

AD-A073 152

MASSACHUSETTS INST OF TECH LEXINGTON LINCOLN LAB
SOLID STATE RESEARCH. 1979:1.(U)
FEB 79 A L MCWHORTER

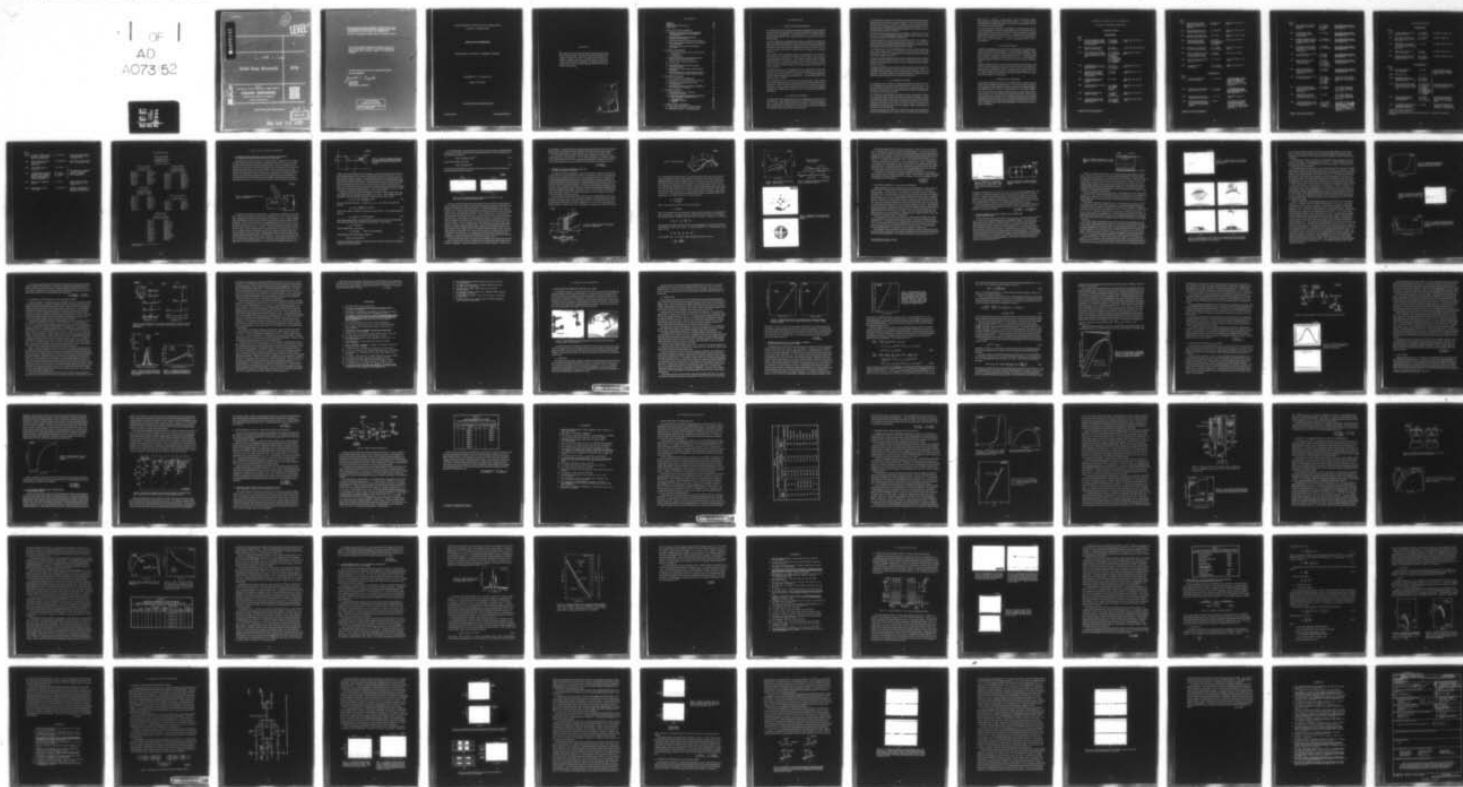
F/G 20/12

UNCLASSIFIED

ESD-TR-79-8

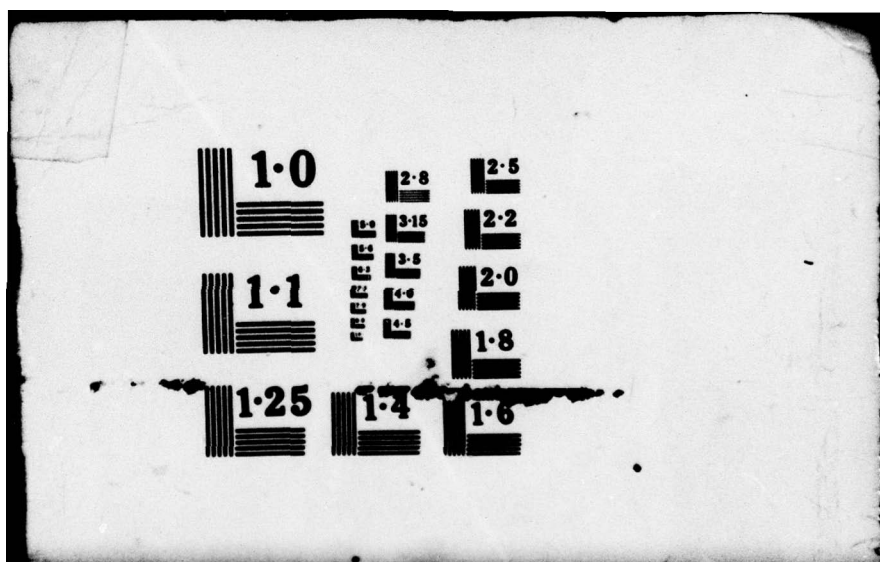
F19628-78-C-0002
NL

1 OF 1
AD
A073 52



END
DATE
FILMED

9-79
DDC



12
B.S.

LEVEL

A073152

207 650

1

See 1473 in back

Solid State Research

1979

DDC FILE COPY

Prepared
under Electronic Systems Division Contract F19628-78-C-0002 by

Lincoln Laboratory

MASSACHUSETTS INSTITUTE OF TECHNOLOGY

LEXINGTON, MASSACHUSETTS



Approved for public release; distribution unlimited.

DDC
RECEIVED
AUG 28 1979

79 08 24 021

The work reported in this document was performed at Lincoln Laboratory, a center for research operated by Massachusetts Institute of Technology, with the support of the Department of the Air Force under Contract F19628-78-C-0002.

This report may be reproduced to satisfy needs of U.S. Government agencies.

The views and conclusions contained in this document are those of the contractor and should not be interpreted as necessarily representing the official policies, either expressed or implied, of the United States Government.

This technical report has been reviewed and is approved for publication.

FOR THE COMMANDER

Joseph C. Syiek

Joseph C. Syiek
Project Officer
Lincoln Laboratory Project Office

Non-Lincoln Recipients

PLEASE DO NOT RETURN

Permission is given to destroy this document
when it is no longer needed.

MASSACHUSETTS INSTITUTE OF TECHNOLOGY
LINCOLN LABORATORY

SOLID STATE RESEARCH

QUARTERLY TECHNICAL SUMMARY REPORT

1 NOVEMBER 1978 - 31 JANUARY 1979

ISSUED 13 JUNE 1979

Approved for public release; distribution unlimited.

LEXINGTON

MASSACHUSETTS

ABSTRACT

This report covers in detail the solid state research work of the Solid State Division at Lincoln Laboratory for the period 1 November 1978 through 31 January 1979. The topics covered are Solid State Device Research, Quantum Electronics, Materials Research, Microelectronics, and Surface-Wave Technology. Funding is primarily provided by the Air Force, with additional support provided by the Army, ARPA, NSF, and DOE.

Accession For	
NTIS GEMRI	<input checked="" type="checkbox"/>
DDC TAB	<input type="checkbox"/>
Unannounced	<input type="checkbox"/>
Justification	
By	
Distribution/	
Availability Codes	
Dist.	Avail and/or special
A	

CONTENTS

Abstract	iii
Introduction	vii
Reports on Solid State Research	xi
Organization	xvi
 I. SOLID STATE DEVICE RESEARCH	 1
A. Anomalous Noise Behavior in Wide-Bandwidth Photodiodes in Heterodyne and Background-Limited Operation	1
B. Integrated Optical Isolator Using GaAs Interband Faraday Rotation	4
C. High-Speed Response of GaInAsP/InP Photodiodes	7
D. Planar-Guarded Avalanche Diodes in InP Fabricated by Ion Implantation	8
E. Zn-Diffused, Stripe-Geometry GaInAsP/InP Diode Lasers	13
 II. QUANTUM ELECTRONICS	 19
A. High-Repetition-Frequency Mini-TEA CO ₂ Lasers	19
1. Tubular Unit	19
2. Cylindrical Unit	20
B. Maximum Efficiency of a Two-Photon Resonant Third-Harmonic-Generation Process	21
C. FM Mode-Locked Nd _{0.5} La _{0.5} P ₅ O ₁₄ Laser	25
D. Ce:YLF Laser	27
E. Alkali-Metal Resonance-Line Lasers Based on Photodissociation	28
F. Photodeposition of Metal Films with Microscopic Dimensions	30
G. Infrared-Submillimeter Double Resonance in CH ₃ F Using Reradiation from Schottky-Barrier Diodes	30
 III. MATERIALS RESEARCH	 35
A. Laser Annealing of Se-Implanted InP	35
B. Ion-Implanted, Laser-Annealed GaAs Solar Cells	37
C. Efficient GaAs Homojunction Solar Cells on Ge Substrates	41
D. Laser-Emission Study of the Pressure Dependence of the Energy Gap in Tellurium	46
 IV. MICROELECTRONICS	 51
A. Charge-Coupled Devices: SAW/CCD Accumulating Correlator	51
B. Comparison of Coplanar Waveguide and Microstrip for GaAs Monolithic Integrated Circuits	54
1. Calculation of Q	54
2. Calculation of Losses	55
3. Results	56
 V. SURFACE-WAVE TECHNOLOGY	 59
A. Hybrid SAW Chirp-Fourier-Transform System	59
B. Integrating Correlator: 4-Wave Interactions	64

INTRODUCTION

I. SOLID STATE DEVICE RESEARCH

The sensitivity of shot-noise-limited semiconductor photodiodes has been calculated for the case where the high-frequency response is limited by the diffusion of photo-excited carriers to the junction. In this situation there is a marked decrease in high-frequency sensitivity, and the noise spectrum is not a true measure of the frequency response.

An optical isolator has been designed which utilizes the interband Faraday effect in GaAs, thus allowing incorporation of the device into integrated GaAs structures. Based upon new measurements of the Faraday coefficient, the design is shown to be feasible; but, even with an optimum configuration, lengths of the order of a centimeter or fields of many tens of kilogauss would be required for satisfactory performance.

Double-heterostructure GaInAsP/InP inverted mesa photodiodes have been fabricated which have an extremely fast response to optical pulses at $1.05\text{ }\mu\text{m}$ from a $\text{Nd}_{0.5}\text{La}_{0.5}\text{P}_{5}\text{O}_{14}$ mode-locked laser. The calculated response risetime of approximately 45 psec is in reasonable agreement with the measured value of $\sim 50\text{ psec}$. Since all the light is absorbed in the depletion region, a high value of quantum efficiency (~ 70 percent) is observed which is limited primarily by reflection loss at the InP-air interface.

InP planar-guarded avalanche photodiodes have been fabricated from structures formed by Si- and Be-ion implantation into n-type epitaxial layers, which were grown by LPE on (100)-oriented n^+ -InP substrates. The avalanche photodiodes exhibited breakdown voltages of approximately 18 V, and the avalanche gains were typically in the 6 to 8 range.

Deep Zn diffusion from a ZnP_2 source has been found to provide a simple technique for fabricating high-quality, stripe-geometry GaInAsP/InP double-heterostructure diode lasers. Linear CW outputs up to 8 mW per facet have been observed for sufficiently narrow stripe widths, and initial life tests have not revealed any significant difference in reliability between diffused-stripe and conventional proton-defined-stripe lasers.

II. QUANTUM ELECTRONICS

Two distinct gas-recirculating systems have been designed and built for use with the mini-TEA laser. Pulse repetition frequencies in excess of 500 Hz, good mode quality, and average power outputs above 10 W were achieved. Frequency doubling at high repetition rates of the output of one of these units in CdGeAs_2 has yielded an average-power-conversion efficiency of over 28 percent.

A general theoretical analysis of a two-photon resonant third-harmonic generation system has been carried out for plane-wave geometry. The third-harmonic conversion efficiency saturates at 17 percent for a single pass under resonance conditions. This plane-wave result is believed to represent an upper bound on efficiency for any focusing condition, including the tight focusing geometry used to obtain the experimentally observed 4-percent conversion.

An FM mode-locked $\text{Nd}_{0.5}\text{La}_{0.5}\text{P}_5\text{O}_{14}$ laser excited by a CW dye laser has been constructed. By using an intensity correlation technique, pulses as short as 14 psec have been measured, with a 480-MHz repetition rate.

Stimulated emission at 325 nm has been observed from the $5d \rightarrow 4f$ transition in Ce:YLF by using a KrF excimer gas laser for optical excitation. The Ce:YLF laser, which is the shortest-wavelength optically pumped solid state laser obtained to date, is potentially a powerful source of tunable near-UV radiation.

A series of new lasers, involving transitions in Na, K, Rb, and Cs have been realized. Pulsed output powers of 1 to 10 kW have been obtained on the alkali-metal resonance lines. Details of the photodissociative excitation process have been studied in order to optimize these lasers.

The laser-initiated photodeposition of metal films is being investigated as a potential technique for microelectronics fabrication. An ArF excimer laser has been used to deposit cadmium films with microscopic features by photodissociating an organo-metallic carrier gas.

The tunable submillimeter spectrometer previously developed has been applied to a *submillimeter-infrared* double-resonance study of excited molecular states. The centrifugal distortion splittings of excited-state rotational transitions in CH_3F were measured. Generation and detection of tunable submillimeter radiation are accomplished using optically pumped lasers and Schottky-diode mixers.

III. MATERIALS RESEARCH

The usefulness of laser heating for removing ion-implantation damage in InP has been demonstrated by annealing Se-doped samples with a CW Nd:YAG laser. For the best samples, the values of carrier concentration and mobility achieved by laser annealing are comparable to those typically observed for similarly implanted samples that have been thermally annealed.

The feasibility of using ion implantation followed by laser annealing in the fabrication of GaAs solar cells has been demonstrated by using this technique to prepare cells utilizing a shallow-homojunction $n^+/p/p^+$ structure without a GaAlAs window. Conversion efficiencies up to 12 percent at AM1 have been obtained for these ion-implanted, laser-annealed (IILA) cells, in which the n^+ -layer was formed by implanting Se^+ ions into the p-layer and then annealing, without encapsulation, by scanning with a CW Nd:YAG laser.

Conversion efficiencies up to 20 percent at AM1 have been obtained for single-crystal GaAs shallow-homojunction solar cells prepared by chemical vapor deposition on

single-crystal Ge substrates. These devices, which are fabricated without $\text{Ga}_{1-x}\text{Al}_x\text{As}$ layers, employ a thin $n^+/p/p^+$ GaAs structure. The spectral response and efficiency show steady improvement as the n^+ -layer is thinned to 200 \AA by means of an anodization-stripping technique.

The very large pressure dependence of the bandgap of Te, which makes this material an attractive candidate for optically pumped tunable lasers in the mid-infrared, has been precisely measured to 8 kbar in a study of the laser emission of an optically pumped sample at liquid-nitrogen temperatures. The bandgap at 63 K is given by the quadratic expression $E_g(P) = E_g(0) + AP + BP^2$, where P is the pressure in kilobars, $E_g(0) = 333.5 \pm 0.5\text{ meV}$, $A = -20.0 \pm 0.5\text{ meV/kbar}$, and $B = 0.52 \pm 0.02\text{ meV/kbar}^2$.

IV. MICROELECTRONICS

A SAW/CCD accumulating correlator has been demonstrated which is capable of correlating two long-duration analog signals. The CCD samples, multiplies, accumulates, and reads out the cross-correlation function of two SAW input signals which counterpropagate on a delay line in close proximity to the CCD. A signal-processing gain of 30 dB at a bandwidth of 20 MHz has been observed by correlating biphase-modulated pseudonoise waveforms of 100-msec duration in the presence of Gaussian noise.

Coplanar waveguide (CPW) has been compared theoretically with microstrip with the intent of determining which is better for incorporation in GaAs monolithic integrated circuits. Conductor and dielectric losses are lower in microstrip than in CPW when the substrate height is equal to the ground-plane spacing in CPW. However, when radiation loss is included and the ground spacing is allowed to increase in the CPW, the guides are comparable.

V. SURFACE-WAVE TECHNOLOGY

A high-speed (10-MHz) analog system for computing Fourier transforms by the chirp-transform technique has been developed. The critical elements are reflective-array-compressor (RAC) dispersive delay lines with large time-bandwidth products. When digital interfaces are added, the system functions as a fast hybrid computer.

Four-wave parametric interactions are being explored in acoustoelectric integrating correlators. Such interactions involve the differential delay, mixing, and integration of signal and reference SAWs propagating in the presence of a stationary pump applied to the silicon-diode array. The scheme significantly reduces spurious signals by permitting the degeneracy between signal and reference RF carriers to be lifted. In addition, a unique signal-processing function—triple-product correlation—may be implemented.

REPORTS ON SOLID STATE RESEARCH

15 November 1978 through 15 February 1979

PUBLISHED REPORTS

Journal Articles

<u>JA No.</u>			
4816	Pressure and Intensity Dependence of Multiphoton Energy Deposition and Reaction Yield in Vinyl Chloride	F. M. Lussier* J. I. Steinfeld* T. F. Deutsch	Chem. Phys. Lett. <u>58</u> , 277 (1978)
4826	Thermal Conductivity and Specific Heat of $\text{NdP}_5\text{O}_{14}$	S. R. Chinn W. K. Zwicker*	J. Appl. Phys. <u>49</u> , 5892 (1978)
4838	Real-Time Spectral Analysis of Far-Infrared Laser Pulses Using a SAW Dispersive Delay Line	H. R. Fetterman P. E. Tannenwald C. D. Parker J. Melngailis R. C. Williamson P. Woskoboinkow* H. C. Praddaude* W. J. Mulligan*	Appl. Phys. Lett. <u>34</u> , 123 (1979)
4841	Λ -Doubling in the $v = 2 \leftarrow 0$ Overtone Band in the Infrared Spectrum of NO	A. S. Pine J. W. C. Johns* A. G. Robiette*	J. Mol. Spectrosc. <u>74</u> , 52 (1979)
4847	Molecular-Beam Tunable-Diode-Laser Sub-Doppler Spectroscopy of Λ -Doubling in Nitric Oxide	A. S. Pine K. W. Nill*	J. Mol. Spectrosc. <u>74</u> , 43 (1979)
4852	Transverse Modes in Gap-Coupled Surface-Wave Devices	S. A. Reible	Appl. Phys. Lett. <u>34</u> , 103 (1979)
4859	An Acoustic SAW/CCD Buffer Memory Device	D. L. Smythe R. W. Ralston B. E. Burke E. Stern	Appl. Phys. Lett. <u>33</u> , 1025 (1978)
4862	Efficient Thallium Photo-dissociation Laser	D. J. Ehrlich J. Maya* R. M. Osgood, Jr.	Appl. Phys. Lett. <u>33</u> , 931 (1978)
4875	Vibrational Kinetics of SF_6 Dissolved in Simple Cryogenic Liquids	S. R. J. Brueck T. F. Deutsch R. M. Osgood, Jr.	Chem. Phys. Lett. <u>60</u> , 242 (1979)

* Author not at Lincoln Laboratory.

JA No.

- | | | | |
|------|--|---|---|
| 4879 | Enhancement of Nonlinear Optical Processes with a Double-Pass Tight-Focusing Geometry | S. R. J. Brueck
H. Kildal | Appl. Phys. Lett. <u>33</u> , 928 (1978) |
| 4880 | Electrode Materials for the Photoelectrolysis of Water | J. G. Mavroides | Mater. Res. Bull. <u>13</u> , 1379 (1978) |
| 4883 | Effect of H ₂ on Residual Impurities in GaAs MBE Layers | A. R. Calawa | Appl. Phys. Lett. <u>33</u> , 1020 (1978) |
| 4884 | On the Possible Magnetic Field Dependence of the Nickel Carbonylation Rate | R. S. Mehta*
M. S. Dresselhaus*
G. Dresselhaus*
H. J. Zeiger | Surf. Sci. <u>78</u> , 681 (1978) |
| 4887 | Beryllium-Ion Implantation in InP and In _{1-x} Ga _x As _y P _{1-y} | J. P. Donnelly
C. A. Armiento | Appl. Phys. Lett. <u>34</u> , 96 (1979) |
| 4893 | Efficient Frequency Tripling of CO ₂ -Laser Radiation in Tandem CdGeAs ₂ Crystals | N. Menyuk
G. W. Iseler | Opt. Lett. <u>4</u> , 55 (1979) |
| 4904 | Optically Pumped LPE-Grown Hg _{1-x} Cd _x Te Lasers | T. C. Harman | J. Electron. Mater. <u>8</u> , 191 (1979) |
| 4905 | Crystal Structure of K ₅ NdLi ₂ F ₁₀ | H. Y-P. Hong
B. C. McCollum* | Mater. Res. Bull. <u>14</u> , 137 (1979) |

Meeting Speeches

MS No.

- | | | | |
|------|---|------------------------------|---|
| 4229 | Solar Energy Application of Natural Zeolites | D. I. Tchernev | In <u>Natural Zeolites: Occurrence, Properties, Use</u> , edited by L. B. Sand and Mumpton (Pergamon Press, Oxford and New York, 1978), pp. 479-485 |
| 4589 | High-Efficiency GaAs Shallow-Homojunction Solar Cells | J. C. C. Fan
C. O. Bozler | In <u>Thirteenth IEEE Photovoltaic Specialists Conference - 1978</u> (IEEE, New York, 1978), pp. 953-955 |
| 4590 | Selective-Black Absorbers Using Sputtered Cermet Films | J. C. C. Fan | Thin Solid Films <u>54</u> , 139 (1978) |
| 4709 | Performance Requirements for Analog Signal Processors in Radar and Communications Systems | E. Stern | Proc. SPIE Vol. 154: <u>Real-Time Signal Processing</u> , T. F. Tao, Ed. (Society of Photo-Optical Instrumentation Engineers, San Diego, 1978), pp. 174-180 |

* Author not at Lincoln Laboratory.

MS No.

- | | | | |
|------|---|---|---|
| 4757 | An Acoustoelectric Schottky-Diode Memory-Correlator Subsystem | D. H. Hurlburt
R. W. Ralston
R. P. Baker
E. Stern | <u>1978 Ultrasonics Symposium Proceedings</u> (IEEE, New York, 1978), pp. 33-37 |
| 4758 | Acoustoelectric Signal-Processing Devices with Charge Storage | J. H. Cafarella | <u>1978 Ultrasonics Symposium Proceedings</u> (IEEE, New York, 1978), pp. 767-774 |
| 4759 | Automated Pulsed Techniques for Measuring the Phase and Amplitude Response of SAW Devices | J. H. Holtham
R. C. Williamson | <u>1978 Ultrasonics Symposium Proceedings</u> (IEEE, New York, 1978), pp. 607-610 |
| 4761 | Interaction of Surface Waves and Bulk Waves in Gratings: Phase Shifts and a New Type of Resonance | J. Melngailis
R. C. Williamson | <u>1978 Ultrasonics Symposium Proceedings</u> (IEEE, New York, 1978), pp. 623-629 |
| 4762 | Transverse Modes in Acoustoelectric Convolvers | S. A. Reible
K. L. Wang*
V. S. Dolat | <u>1978 Ultrasonics Symposium Proceedings</u> (IEEE, New York, 1978), pp. 48-53 |
| 4763 | High-Performance Hybrid SAW Chirp-Fourier-Transform System | V. S. Dolat
M. B. Schulz
L. A. Veilleux
G. R. McCully
R. C. Williamson | <u>1978 Ultrasonics Symposium Proceedings</u> (IEEE, New York, 1978), pp. 527-532 |
| 4766 | Fast Synchronization in a Spread-Spectrum System Based on Acoustoelectric Convolvers | D. Brodtkorb
J. E. Laynor | <u>1978 Ultrasonics Symposium Proceedings</u> (IEEE, New York, 1978), pp. 561-566 |
| 4780 | mm-Wave Integrated Circuits for Strategic Sensors | R. W. Laton
W. E. Courtney
R. A. Murphy
C. O. Bozler
H. J. Stalzer
G. B. Jones | Proc. Govt. Microcircuits Applications Conf., Monterey, California, 14-16 November 1978 |
| 4797 | Surface-Oriented Schottky Barrier Diodes for Millimeter and Submillimeter Wave Applications | R. A. Murphy
B. J. Clifton | Proc. IEEE Intl Electron Devices Mtg., Washington, D. C., 4-6 December 1978, pp. 124-128 |
| 4798 | GaInAsP/InP Lasers and Detectors for Fiber Optics Communications at 1.1-1.3 μm | J. J. Hsieh | Proc. IEEE Intl Electron Devices Mtg., Washington, D. C., 4-6 December 1978, pp. 628-629 |
| 4802 | Vibrational Kinetics in Cryogenic Liquids and Applications to Nonlinear Optics | S. R. J. Brueck
T. F. Deutsch
H. Kildal
R. M. Osgood, Jr. | Proc. SPIE Vol. 158: <u>Laser Spectroscopy - Applications and Techniques</u> , H. Schlossberg, Ed. (Society of Photo-Optical Instrumentation Engineers, San Diego, 1978), pp. 122-131 |

* Author not at Lincoln Laboratory.

UNPUBLISHED REPORTS

Journal Articles

JA No.			
4829	ν_3 Mode Absorption Behavior of Laser Excited SF ₆	T. F. Deutsch S. R. J. Brueck	Accepted by J. Chem. Phys.
4897	Linear Scan Control of Tunable Lasers Using a Scanning Fabry-Perot	M. J. Coulombe A. S. Pine	Accepted by Appl. Opt.
4899	Preparation of Sn-Doped In ₂ O ₃ (ITO) Films at Low Deposition Temperatures by Ion-Beam Sputtering	J. C. C. Fan	Accepted by Appl. Phys. Lett.
4906	Higher Order Nonlinear Processes in CdGeAs ₂	H. Kildal G. W. Iseler	Accepted by Phys. Rev. B
4907	Emission Cross Section and Flashlamp-Excited NdP ₅ O ₁₄ Laser at 1.32 μ m	M. M. Choy* W. K. Zwicker* S. R. Chinn	Accepted by Appl. Phys. Lett.

Meeting Speeches†

MS No.			
4295A	Liquid Phase Epitaxy of III-V Compounds	J. J. Hsieh	American Association for Crystal Growth, Cambridge, Massachusetts, 23 January 1979
4883A	GaAs Solar Cells	J. C. C. Fan	
4753A	Flashlamp-Excited Low-Threshold Miniature NdP ₅ O ₁₄ Laser at 1.32 μ m	M. M. Choy* W. K. Zwicker* S. R. Chinn*	International Conference on Lasers '78, Orlando, Florida, 11-15 December 1978
4791A	Real-Time Spectral Analysis of Far Infrared Laser Pulses Using a SAW Dispersive Delay Line	H. R. Fetterman P. E. Tannenwald C. D. Parker J. Melngailis R. C. Williamson P. Woskoboinikow* H. C. Praddaude* W. J. Mulligan*	
4782	Efficient GaAs Shallow-Homojunction Solar Cells on Ge Substrates	C. O. Bozler J. C. C. Fan R. W. McClelland	Intl Symp. on GaAs and Related Materials, St. Louis, Missouri, 24-27 September 1978
4793	Zn-Diffused, Stripe-Geometry, Double-Heterostructure GaInAsP/InP Diode Lasers	J. J. Hsieh	6th IEEE Intl Semiconductor Laser Conf., San Francisco, 30 October - 1 November 1978

* Author not at Lincoln Laboratory.

† Titles of Meeting Speeches are listed for information only. No copies are available for distribution.

MS No.

- | | | | |
|-------|---|---|---|
| 4802B | Molecular Vibrations in Simple Liquids - Spectroscopy, Kinetics and Applications | S. R. J. Brueck | Harvard-MIT Joint Physical Chemistry Seminar, M.I.T., 16 November 1978 |
| 4844 | Surface Acoustic Wave Devices: Principles and Applications | R. C. Williamson | MIT Industrial Liaison Symp., M.I.T., 7-8 December 1978 |
| 4878 | Liquid Phase Epitaxy of $\text{Hg}_{1-x}\text{Cd}_x\text{Te}$ | T. C. Harman | Gordon Research Conference on Crystal Growth, Santa Barbara, California, 14-19 January 1979 |
| 4914 | Crystallographic Orientation of Silicon on an Amorphous Substrate Using Artificial Surface Relief Grating and Laser Crystallization | M. W. Geis
D. C. Flanders
H. I. Smith | |
| 4883 | Solar Cells: Plugging into the Sun | J. C. C. Fan | Applied Physics Lectures, Harvard University, 5 December 1978 |
| 4905A | Alkali-Metal Resonance-Line Lasers | R. M. Osgood, Jr. | Seminar, National Bureau of Standards, Gaithersburg, Maryland, 29 January 1979 |

ORGANIZATION

SOLID STATE DIVISION

A. L. McWhorter, *Head*
I. Melngailis, *Associate Head*
J. F. Goodwin, *Assistant*

P. E. Tannenwald, *Senior Staff*

QUANTUM ELECTRONICS

A. Mooradian, *Leader*
P. L. Kelley, *Associate Leader*

Barch, W. E.	Fetterman, H. R.
Belanger, L. J.	Fleming, M. W.*
Blumberg, W. A. M.	Hancock, R. C.
Brueck, S. R. J.	Kildal, H.
Burke, J. W.	Menyuk, N.
Chinn, S. R.	Moulton, P. F.
DeFeo, W. E.	Osgood, R. M., Jr.
Deutsch, T. F.	Parker, C. D.
Ehrlich, D. J.	Peck, D. D.
Feldman, B.	Pine, A. S.

APPLIED PHYSICS

A. G. Foyt, *Leader*
C. E. Hurwitz, *Assistant Leader*
T. C. Harman, *Senior Staff*
R. H. Kingston, *Senior Staff*

Armiento, C. A.*	Liau, Z.-L.
Calawa, A. R.	Lind, T. A.
Carter, F. B.	Maby, E. W.*
DeMeo, N. L., Jr.	McBride, W. F.
Diadiuk, V.	Norris, P. E.*
Donnelly, J. P.	Paladino, A. E.
Duffy, P. E.	Plonko, M. C.
Ferrante, G. A.	Spears, D. L.
Glasser, L. A.*	Tsang, D. Z.*
Groves, S. H.	Walpole, J. N.
Leonberger, F. J.	

ELECTRONIC MATERIALS

A. J. Strauss, *Leader*
H. J. Zeiger, *Associate Leader*
J. G. Mavroides, *Senior Staff*

Anderson, C. H., Jr.	Hong, H. Y.-P.
Bayard, M. L.	Hsieh, J. J.
Button, M. J.	Iseler, G. W.
Chapman, R. L.	Kafalas, J. A.
Davis, F. M.	Kolesar, D. E.
Delaney, E. J.	Krohn, L., Jr.
Fahey, R. E.	Mastromattei, E. L.
Fan, J. C. C.	Owens, E. B.
Finn, M. C.	Palm, B. J.
Flutie, R. E.	Pantano, J. V.
Gale, R. P.	Tracy, D. M.
Gay, R. R.*	Vohl, P.

SURFACE WAVE TECHNOLOGY

E. Stern, *Leader*
R. C. Williamson, *Associate Leader*

Baker, R. P.	Kernan, W. C.
Becker, R. A.	Oates, D. E.
Brogan, W. T.	Ralston, R. W.
Cafarella, J. H.	Reible, S. A.
Dolat, V. S.	Slattery, R. L.
Holtham, J. H.	Withers, R. S.
Hurlburt, D. H.	Yao, I.

MICROELECTRONICS

W. T. Lindley, *Leader*
F. J. Bachner, *Associate Leader*
H. I. Smith, *Assistant Leader*

Alley, G. D.	Gray, R. V.
Bozler, C. O.	Hansell, G. L.*
Burke, B. E.	Hawryluk, A. M.*
Chiang, A. M.	Lincoln, G. A., Jr.
Chu, A.	McGonagle, W. H.
Clifton, B. J.	Melngailis, J.
Daniels, P. J.	Mountain, R. W.
DeGraff, P. D.	Murphy, R. A.
Durant, G. I.	Pichler, H. H.
Eastman, L. F.	Shaver, D. C.*
Efremow, N., Jr.	Silversmith, D. J.
Elta, M. E.	Smythe, D. L., Jr.
Felton, B. J.	Sotomayer-Diaz, O.*
Flanders, D. C.	Turner, G. W.
Geis, M. W.	Wilde, R. E.
Gopinath, A.	

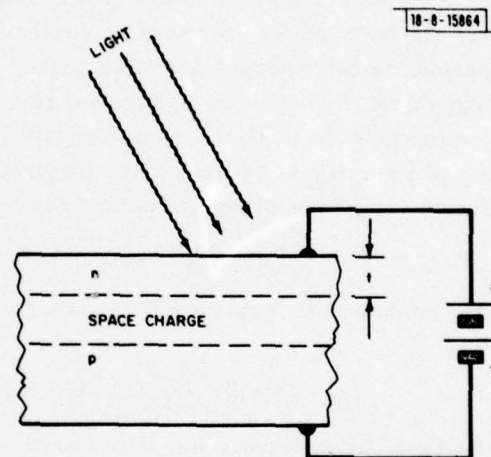
* Research assistant

I. SOLID STATE DEVICE RESEARCH

A. ANOMALOUS NOISE BEHAVIOR IN WIDE-BANDWIDTH PHOTODIODES IN HETERODYNE AND BACKGROUND-LIMITED OPERATION

Anomalous noise behavior can occur at high frequencies in photodiodes when the high-frequency response is limited by diffusion of photoexcited carriers to the junction. Although the signal current thus decreases with increasing frequency because of the dispersion in the diffusion times, the noise current remains fixed since it is a function only of the DC flow reaching the space-charge region. Under these conditions, there is a marked decrease in high-frequency sensitivity, and the noise spectrum is not a true measure of the frequency response. This effect on the sensitivity or noise equivalent power (NEP) has never been previously considered and is particularly important in the case of long-wavelength infrared photodiodes at low temperatures, since it is difficult to confine the photocarrier generation to the junction depletion region because of the low absorption coefficient¹ in narrow-bandgap semiconductors.

Fig. I-1. Schematic diagram of reverse-biased n/p photodiode.



Consider the diode structure, shown in Fig. I-1, consisting of an undepleted n-type surface layer, a space-charge region, and a p-type base. In general, when such a structure is illuminated, photoexcited carriers will be produced in all three regions. In fact, at long wavelengths where the absorption coefficient is low it is difficult to avoid this situation in shallow-junction photodiodes. The generation of photocurrent in a photodiode involves two processes: (1) the production of electron-hole pairs, and (2) the separation of these pairs by the action of the high field of the space-charge layer (e.g., see Ref. 2). For an electron-hole pair produced outside the space-charge region, diffusion produces a statistical spread in the arrival time at the junction. An additional impulse broadening occurs for all carriers due to the finite transit time across the space-charge region, which is typically small compared with the diffusion process and can be ignored for present purposes. If the thickness t of the n-type layer is greater than the diffusion length for holes, a loss in signal current occurs for frequencies greater than $1/2\pi\tau_p$, where τ_p is the hole recombination time. If t is less than a diffusion length, then a loss in signal occurs at frequencies above $D_p/2\pi t^2$, where D_p is the hole-diffusion coefficient. If we

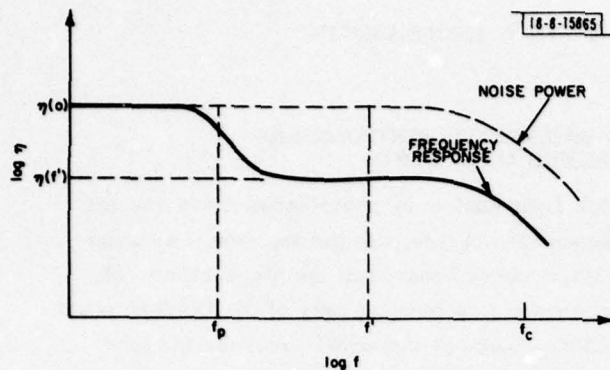


Fig. I-2. Frequency response (solid line) and noise spectrum (dashed line) of photodiode with hole-diffusion component to its response.

consider only the hole-diffusion effect, the frequency response of the photodiode in terms of an effective quantum efficiency $\eta(f)$ is shown schematically by the solid curve in Fig. I-2. $\eta(0)$ is the DC quantum efficiency and $\eta(f)$ is the effective quantum efficiency at frequencies above the point where hole diffusion contributes. Shot noise is produced by the random passage of charge carriers across the space-charge region. The associated noise power spectrum is determined by the space-charge transit time and the external RC cutoff, as shown by the dashed line in Fig. I-2. The noise power spectrum is clearly not a reliable measure of the frequency response of the device, as has been previously assumed.³ This can have a profound effect on the ultimate sensitivity of the photodiode at high frequencies, as will be shown below.

Consider heterodyne operation of the photodiode and assume a local-oscillator power P_{LO} and a signal power P_S at the respective frequencies, ν_{LO} and ν_S . Then, assuming unity mixing efficiency, the time-dependent optical power input to the diode may be written

$$P(t) = P_{LO} + P_S + 2\sqrt{P_{LO}P_S} \cos(2\pi f't) \quad (I-1)$$

where the intermediate frequency f' is given by $\nu_{LO} - \nu_S$. The resultant IF current then becomes

$$i_{IF} = [2e\eta(f') \sqrt{P_{LO}P_S} / h\nu] \cos(2\pi f't) \quad (I-2)$$

where we have chosen a frequency f' as shown on the plot of Fig. I-2. The IF output power then becomes

$$P_{IF} = \langle i_{IF}^2 \rangle R = 2e^2 \eta^2(f') P_{LO} P_S R / h\nu \quad (I-3)$$

after squaring and averaging. The noise power is that produced by the shot noise associated with the local-oscillator current flowing across the junction. This current is

$$i_{LO} = e\eta(0)P_{LO}/h\nu \quad (I-4)$$

and the resultant noise power becomes

$$P_n = 2ei_{LO}BR, \quad \text{where } B \text{ is the bandwidth} \quad (I-5)$$

The final signal-to-noise ratio $(S/N)_P$ is given by

$$(S/N)_P = \eta^2(f')P_S / \eta(0)h\nu B \quad (I-6)$$

Note that the heterodyne sensitivity is reduced by a factor $\eta(f')/\eta(0)$ from the value $\eta(f')P_S/h\nu B$ obtained when diffusion is ignored.

In a similar fashion, a background-limited incoherent detector exposed to background radiation P_B will have a high-frequency envelope response limited by $\eta(f)$, and the resultant NEP for short pulses will be given by

$$NEP = [2h\nu BP_B \eta(0)/\eta^2(f)]^{1/2} \quad (I-7)$$

rather than the familiar expression,

$$NEP = [2h\nu BP_B / \eta(f)]^{1/2} \quad (I-8)$$

The sensitivity degradation factor $\eta(f)/\eta(0)$ is thus common to both heterodyne operation and background-limited incoherent detection.

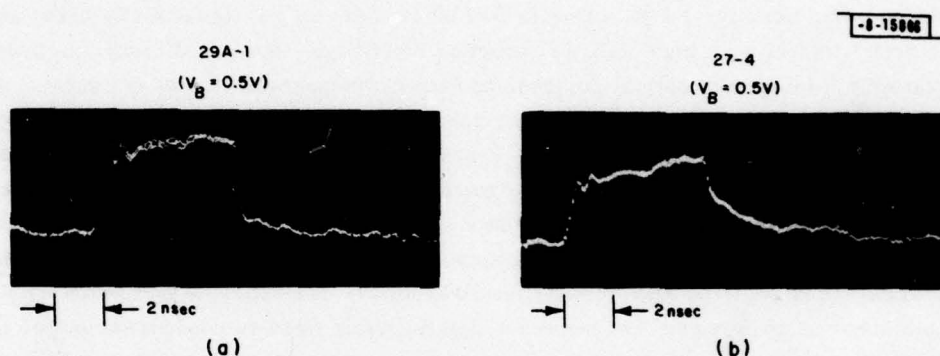


Fig. I-3(a-b). Oscilloscope displays showing pulse response at $10.6 \mu\text{m}$ of two reverse-biased HgCdTe photodiodes.

The very strong effect which slow carrier diffusion can have on heterodyne sensitivity appears to explain the wide variation in high-frequency heterodyne minimum-detectable power observed in low-capacitance, high-quantum efficiency n/p HgCdTe photodiodes.⁴ Slow carrier diffusion can be revealed by the pulse response of the diode;^{4,5} two examples of this are shown in Fig. I-3(a-b). These two HgCdTe photodiodes were illuminated with a 5-nsec CO_2 -laser pulse formed by a fast CdTe electrooptic modulator. The reverse bias of 0.5 V resulted in an RC roll-off frequency much greater than 1 GHz. The device in Fig. I-3(a) shows rise and fall times less than 0.3 nsec, the response of the sampling scope electronics. In contrast, Fig. I-3(b) shows an additional slow transient of about 3-nsec extent which represents about 50 percent of the total response. This slow component, due to hole diffusion in the n-type material, corresponds to a frequency cutoff f_p of about 50 MHz. Direct heterodyne sensitivity measurements have been carried out using blackbody heterodyne radiometry at 760 MHz (see Refs. 4 and 6). Diodes with the simple response of Fig. I-3(a) exhibited sensitivities within a factor-of-2 of the ideal minimum-detectable power $h\nu B$, while those showing the slow transient of Fig. I-3(b) had sensitivities 2 to 4 times poorer, even though the low-frequency quantum efficiencies were comparable. Consistent with the previous arguments was a shot-noise spectrum for both types of diodes with constant noise power out to about 2 GHz (see Refs. 4 and 6).

To avoid the loss of sensitivity associated with hole diffusion, the n-type layer can be made very thin or heavily doped (to create a significant shift of the absorption edge to shorter wavelengths by bandfilling). This latter technique limits the optimum response to a rather narrow

spectral region. An alternate approach which alleviates this problem is to decrease the lifetime of holes in the n-type material so that no photogenerated holes live long enough to produce a slow transient. Having them recombine eliminates their contribution to the noise output.

If any radiation is absorbed in the p-type base region, diffusion of electrons to the space-charge region must also be considered. In 10- μm HgCdTe photodiodes, the mobility of electrons is much higher than the hole mobility; consequently, degradation in sensitivity due to the presence of electron diffusion occurs at substantially higher frequencies, of the order of 1 GHz.

D. L. Spears
R. H. Kingston

B. INTEGRATED OPTICAL ISOLATOR USING GaAs INTERBAND FARADAY ROTATION

Isolation of unidirectional signal flow in optical circuits may be obtained by using the gyro-magnetic properties of such materials as garnet or semiconductors. Until now, the former has been proposed for integrated optical devices, and the nonreciprocal effects are dependent upon coupling of the optical wave into and out of the garnet material.⁷ In contrast, by utilizing the interband Faraday effect in semiconductors, it should be possible to build isolators on the same substrate and utilize the same semiconductor material as that of the laser or LED sources and detectors. Here, we describe the design of such a device and the required dimensions and magnetic field. The results are based on recent measurements of GaAs Faraday rotation obtained at the Francis Bitter National Magnet Laboratory at M.I.T. We conclude that, even with the optimum configuration considered, the required high magnetic field or consequent device length make such an isolator of marginal interest.

Prior designs for isolators utilized the rotation of the plane of polarization to obtain nonreciprocity, which in low-order mode waveguide necessitates mode conversion and the resultant filtering of the unwanted mode by waveguide cutoff techniques. The design proposed here uses the nonreciprocal phase shift in a properly designed guide, as in Fig. I-4(a), and requires two parallel sections, as shown in Fig. I-4(b). Alternatively, one might use a waveguide 3-dB hybrid

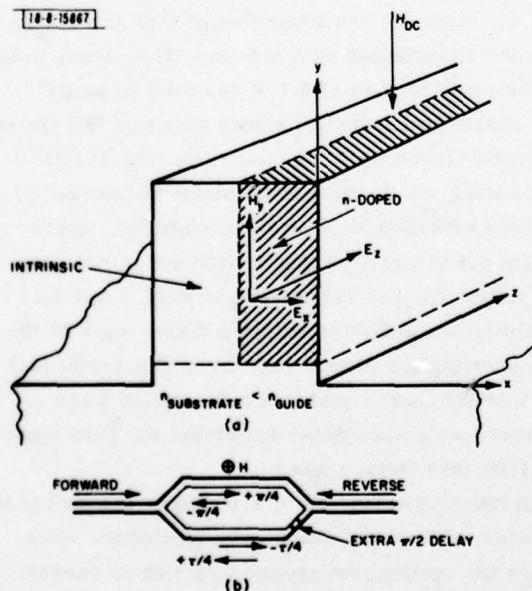
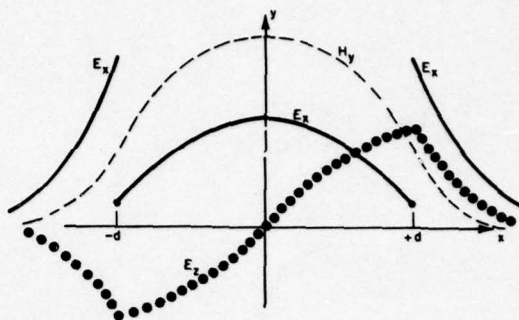


Fig. I-4. (a) Ridge waveguide configuration; (b) isolator configuration.

Fig. I-5. Field distribution.



as in conventional microwave isolators.⁸ The ridge waveguide in Fig. I-4(a), for a width $2d$ of $0.2\lambda_0$ or approximately 2000 \AA , has the property that the transverse electric field E_x and the longitudinal field E_z have equal maximum values and, therefore, the net field in either side of the guide is circularly or near-circularly polarized over a large fraction of the guide width. (It is not possible to obtain this circular behavior in a slab guide bounded by only one air interface, since the ratio of longitudinal to transverse E -field is roughly proportional to $\Delta n/n$, where n is the index of the guide and Δn is the change in index at the non-air interface.) The detailed behavior of the field is shown in Fig. I-5, where the E_x variation is effectively a cosine, and E_z is a sine wave. From waveguide perturbation theory,⁸ the change in propagation constant with application of a DC magnetic field in the z -direction becomes

$$\Delta\beta = \frac{\omega \int \epsilon_2 E_x E_z dA}{\int E_x H_y dA}$$

where ϵ_2 may be written in terms of the Faraday rotation as

$$\epsilon_2 = \epsilon_0 \frac{\lambda_0}{\pi} \left(\frac{\Theta}{l} \right) n$$

Now, if ϵ_2 is constant across the whole guide, then $\Delta\beta$ becomes zero since E_z is antisymmetric and E_x is symmetric. By doping one side of the guide with donor impurities, the off-diagonal term becomes large in the doped material and small in the undoped, resulting in a net $\Delta\beta$ given by

$$\Delta\beta \approx \frac{\epsilon_2}{\epsilon_0} \cdot \frac{1}{\pi} \cdot \frac{\beta}{n} = \frac{\lambda_0 \beta}{2\pi n} \cdot \left(\frac{\Theta}{l} \right)$$

Note here that $\Delta\beta$ changes sign if the direction of wave propagation is reversed, since the field E_z changes sign, while E_x is unchanged. For this waveguide size, βd is approximately $\pi/2$, and with $d = 0.1\lambda_0$,

$$\Delta\beta = \frac{\lambda_0}{\pi} \cdot \frac{1}{2nd} \cdot \left(\frac{\Theta}{l} \right) = \frac{5}{\pi n} \cdot \left(\frac{\Theta}{l} \right)$$

For an isolator, $\Delta\beta L = \pi/4$, and the required length of the structure becomes

$$L = \frac{\pi}{4\Delta\beta} = \frac{\pi^2 n}{20(\Theta/l)}$$

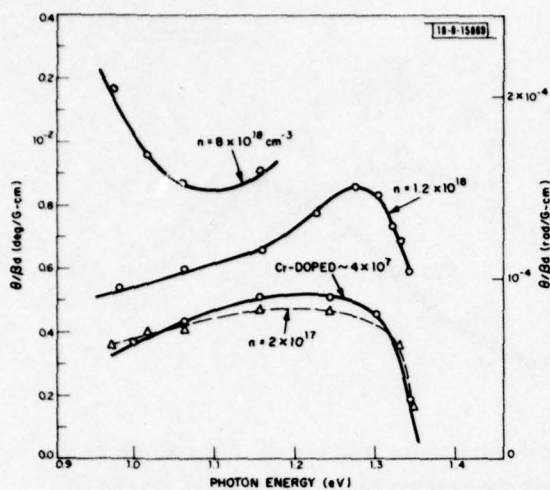


Fig. I-6. Faraday coefficient vs photon energy. GaAs at 300 K.

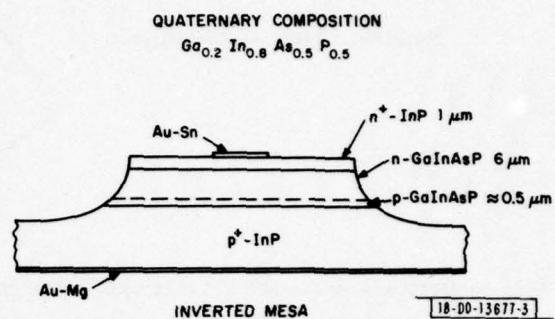


Fig. I-7. Schematic diagram of GaInAsP/InP avalanche photodiode structure.



Fig. I-8. Photograph of four GaInAsP/InP detectors mounted in a high-speed quad package.



The Faraday coefficient for GaAs was first measured by Piller,⁹ and the measurements were recently extended at the M.I.T. National Magnet Laboratory. The results are shown in Fig. I-6, and indicate that higher coefficients (and a reasonable differential phase shift) may be obtained with heavier doping. Unfortunately, the pronounced increase between 10^{17} and 10^{18} cm^{-3} doping density is accompanied by a rapid increase in optical absorption coefficient.¹⁰ At $2 \times 10^{18} \text{ cm}^{-3}$, for example, the coefficient is 5 cm^{-1} . As a result, if a forward transmission of 37 percent is allowable, then the length L would be limited to 2 mm. For a net coefficient of 10^{-4} rad/cm-G , this would require a magnetic field of 80 to 90 kG, available only with a superconducting magnet. It is possible that lower doping might yield a longer structure and reduced field requirement, or undoped material with a variation in bandgap from one side to the other of the guide might yield long structures without the attendant insertion loss.

In conclusion, it would appear that isolators using GaAs are feasible, but would require rather long structures or extremely high magnetic fields. Other materials at longer wavelengths would probably yield higher coefficients (InSb, for example), but the need for isolation at these wavelengths has not been established.

R. H. Kingston
S. Yuen†
R. Aggarwal†

C. HIGH-SPEED RESPONSE OF GaInAsP/InP PHOTODIODES

Double-heterostructure (DH) GaInAsP/InP inverted mesa photodiodes, similar to those described earlier,^{11,12} show an extremely fast response to optical pulses at $1.05 \mu\text{m}$ from a $\text{Nd}_{0.5}\text{La}_{0.5}\text{P}_5\text{O}_{14}$ mode-locked laser. These detectors, the structure of which is shown schematically in Fig. I-7, are fabricated from a wafer in which the quaternary layer was very lightly doped ($N_d - N_a \approx 2 \times 10^{15} \text{ cm}^{-3}$), thus permitting operation at biases well above that required for the depletion layer to "punch through" to the top n^+ -InP layer. When operated as avalanche detectors, the devices show modest gain (≤ 5 times) and substantial dark current ($> 10 \mu\text{A}$). However, when reverse-biased at voltages from 0.5 to 0.8 of the breakdown value, the dark current is reduced substantially (typically $< 200 \text{ nA}$) and the pulse response is very fast. This high speed is the result of the low capacitance associated with the wide depletion region and the fact that the light passes through the transparent InP and generates the electrons and holes directly in the depleted GaInAsP, where the electric field is high. This latter property eliminates the much slower response due to carriers generated by light absorbed in undepleted material, which must then diffuse to the depletion region to be collected.¹²

For measurement, detectors were mounted in a package originally designed for the high-frequency operation of HgCdTe heterodyne detector arrays.⁵ Four diodes mounted thusly are shown in Fig. I-8. The response of one of these detectors, operating into a $50\text{-}\Omega$ load and biased at 85 V, to an approximately 20-psec-wide (FWHM) pulse of $1.05\text{-}\mu\text{m}$ radiation from a mode-locked $\text{Nd}_{0.5}\text{La}_{0.5}\text{P}_5\text{O}_{14}$ laser (described in Sec. II-C) is shown in Fig. I-9. The response is clean and symmetric with 10- to 90-percent rise and fall times of about 60 psec.

The packaged device was examined on a network analyzer at 2 GHz, in order to gain a feeling for the relative contributions to the response characteristics of the device itself, the package, and the measurement apparatus. For the assumed equivalent circuit shown in Fig. I-10, the

† National Magnet Laboratory, M.I.T.

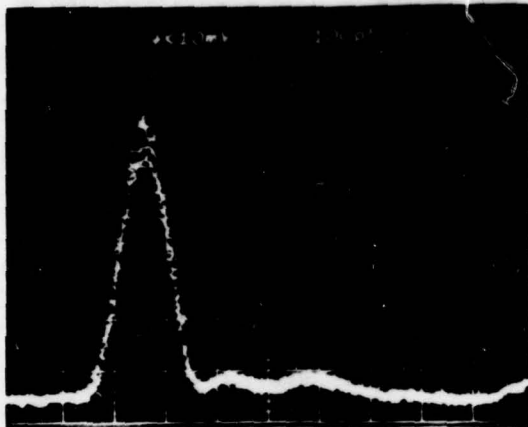


Fig. I-9. Response of a GaInAsP/InP photodiode to a 20-psec-wide pulse from a $\text{Nd}_{0.5}\text{La}_{0.5}\text{P}_5\text{O}_{14}$ laser. Bias voltage was 85 V and load resistor was 50 Ω .

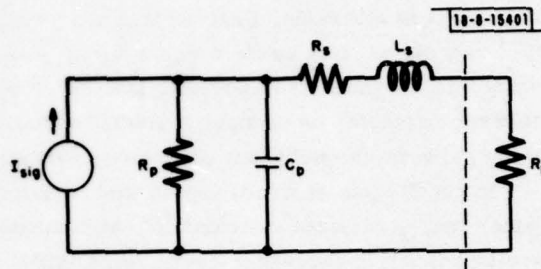


Fig. I-10. Equivalent circuit for packaged photodiode and load. See text for element values.

parameters so obtained were $C_p = 0.3$ pF, $R_s = 15$ Ω , $L_s = 15$ nH, and R_p negligibly large. The calculated 10- to 90-percent response of this circuit to a step input of current for a 50- Ω load is 30 psec. Taking into consideration the 25-psec risetime of the oscilloscope, the approximately 10- to 15-psec risetime of the light pulse, and the estimated 20-psec spread in transit times of holes generated within the depletion region (an absorption length of 1 μm was assumed), the calculated risetime of ≈ 45 psec is in reasonable agreement with that measured.

It is also worth noting that the fact that all the light is absorbed in the depletion region also results in a high value of quantum efficiency (~ 70 percent), which is limited primarily by reflection loss at the InP-air interface.

C. E. Hurwitz F. J. Leonberger
S. R. Chinn D. L. Spears

D. PLANAR-GUARDED AVALANCHE DIODES IN InP FABRICATED BY ION IMPLANTATION

There is currently a great deal of interest in $\text{In}_{1-x}\text{Ga}_x\text{As}_y\text{P}_{1-y}$ avalanche photodiodes^{12,13-16} ($E_g \sim 1.0$ eV) for use in high-bandwidth optical communication systems. To a lesser extent, some interest has been shown in InP IMPATT diodes.¹⁷ All the avalanche diodes reported in these materials have relied on etched mesa and/or punch-through p-n junction structures. Etched mesa diodes depend critically on the etching procedure, i.e., the slope of the mesa at the p-n junction, to prevent edge breakdown. Etching procedures of this type often preclude high-yield fabrication and can present additional surface passivation problems. Punch-through devices depend critically on the thickness and uniformity of the epitaxial layer and on the smoothness of the interface. Here we present some preliminary data on a planar-guarded avalanche structure in InP fabricated using ion implantation. The structure is similar to that used in guarded reach-through Si diodes.^{18,19}

Fig. I-11. Schematic illustration of cross section of a planar-guarded InP p-n junction diode.

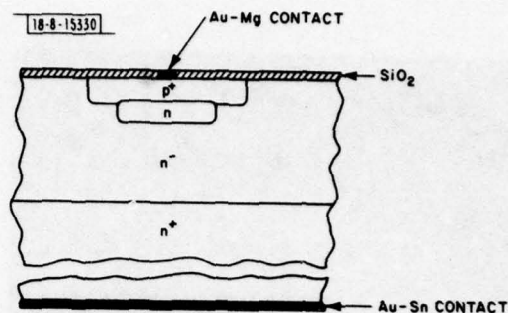


Figure I-11 schematically illustrates a cross section of such a guarded InP p-n junction diode. Viewed from the top, the p^+ - and n -type regions would appear as concentric circles. By appropriately selecting the carrier concentration n and the thickness t of the n -type region (in relation to the concentration in n -region), the maximum electric field at breakdown in the central region can be larger than the electric field at the edge of the p^+ -region. Under this condition, field crowding at the edges will not be sufficient to cause edge breakdown, and avalanche breakdown will occur in the central portion of the diode. The minimum nt product necessary to prevent edge breakdown depends on both the concentration in the n -region and the shape of $p^+ - n^-$ boundary at the periphery.

The InP samples used in this work consist of an n -type epitaxial layer with a concentration of $(1 \text{ to } 2) \times 10^{16} \text{ cm}^{-3}$ grown by liquid-phase epitaxy on a (100)-oriented n^+ -InP substrate. The thickness of the epilayer is not critical but was selected to be greater than $6 \mu\text{m}$ to prevent punch-through, which in this structure would somewhat negate the effects of the central n -type implanted region.

To achieve the central n -type region of Fig. I-11, each sample was coated with a $1000\text{-}\text{\AA}$ layer of SiO_2 and a thick ($\approx 5\text{-}\mu\text{m}$) layer of photoresist. Using photolithographic techniques, 6-mil-diam circles were opened in the photoresist and SiO_2 , and the samples were implanted with 400-keV Si ions at either room temperature or 170°C . The doses used were either 8×10^{12} or $1 \times 10^{13} \text{ cm}^{-2}$. Both doses should result in a peak electron concentration greater than ten times the concentration in the epitaxial layer, and at breakdown a maximum electric field in the central region greater than twice that in the outer rim (neglecting edge effects). As discussed below, best results to date have been obtained with the $8 \times 10^{12} \text{ cm}^{-2}$ dose and a 170°C implant temperature.

After the Si implant, the photoresist mask was removed and a new photoresist layer was applied. Again, using photolithographic techniques, 10-mil-diam circles concentric with the 6-mil-diam Si-implanted regions were opened in the new photoresist and the SiO_2 . The samples were then implanted at room temperature with beryllium to produce the p^+ -layer of Fig. I-11. The dose schedule used for the Be implant was $2 \times 10^{13} \text{ cm}^{-2}$ at 40 keV and $3 \times 10^{13} \text{ cm}^{-2}$ at 30 keV. This Be implant should result in a maximum as-implanted Be concentration of $2.7 \times 10^{18} \text{ cm}^{-3}$, a level at which insignificant indiffusion of implanted Be has been observed.^{20,21}

Following implantation, the photoresist and SiO_2 were removed and the samples were annealed at 750°C for 10 min. using a phosphosilicate glass (PSG) encapsulation procedure described previously.^{20,22} From previous results, about 60 percent of the implanted Be (Ref. 20) and ≥ 80 percent of the implanted Si (Ref. 22) should be electrically active following this anneal.

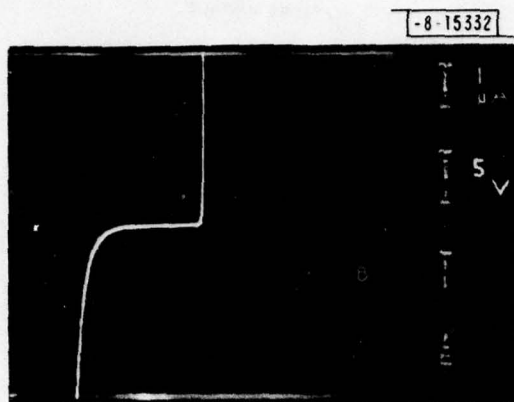
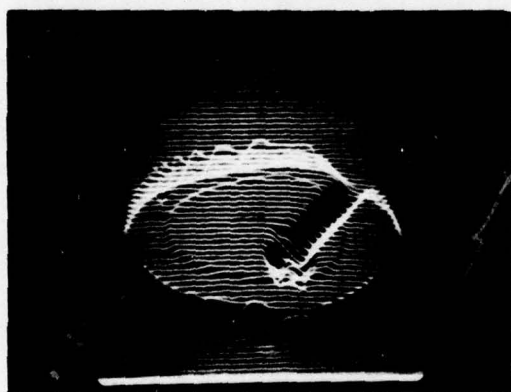
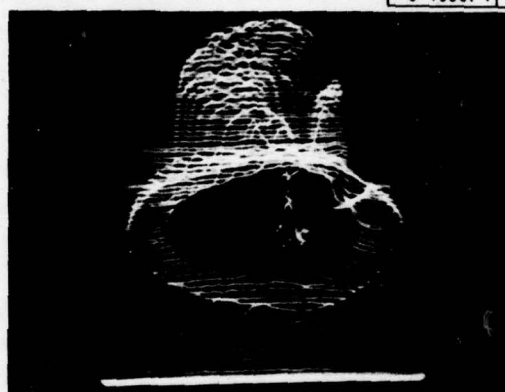


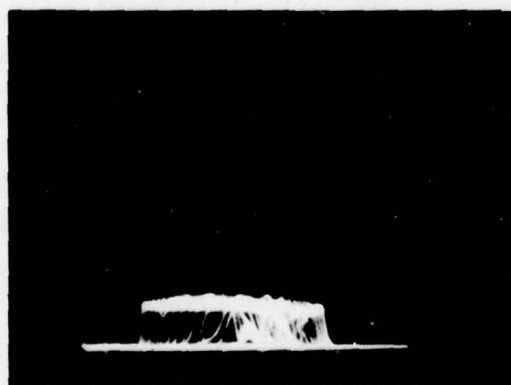
Fig. I-12. Current-voltage characteristics of an ion-implanted planar-guarded InP avalanche diode.



(a)



(c)



(b)



(d)

Fig. I-13. Photoresponse scans at $0.6328 \mu\text{m}$ of a typical planar-guarded InP diode: three-dimensional display at (a) 2 V and (c) 18.2 V reverse bias; two-dimensional display at (b) 2 V and (d) 18.2 V reverse bias.

The p-n junction depth is estimated at about 0.30 μm in the central region and 0.35 μm in the outer rim. This difference in depth is due to the Gaussian falloff in the implanted Be profile and the difference in electron concentration between the Si-implanted region and the initial epitaxial layer.

After annealing, the PSG was removed and a 1500- \AA SiO_2 layer was deposited on the front surface of each sample. Using photolithographic techniques, 1.5-mil-diam holes were opened in the SiO_2 and evaporated Au-Mg contacts were made to the p^+ -regions. Electroplated Au-Sn was used to contact the n^+ substrates.

For initial evaluation of these diodes, their I-V characteristics were measured and scanned photoresponse measurements were performed using the 6328- \AA line of a He-Ne laser. Although diodes on all the samples exhibited photoresponse gain in the central portion, best results were obtained on the sample implanted at 170°C with $8 \times 10^{12} \text{ Si cm}^{-2}$. Since some previous results have shown that less residual damage and higher activation of implanted Si can be achieved by performing the implant at elevated substrate temperatures,²² the implant temperature result is not surprising. The use of the lowest dose possible for this n-type region, while still preventing edge breakdown, should further result in less damage and less possibility of Zener tunneling.

Figure I-12 shows the I-V characteristics of a typical diode. Breakdown, defined as the voltage at which 10- μA reverse current flows, occurs typically at $18 \pm 0.5 \text{ V}$ reverse bias. As can be observed in Fig. I-12, the breakdown is soft. In an attempt to isolate the source of this soft breakdown, planar Be-implanted diodes were fabricated on similar substrates without the Si central implant. These diodes exhibited sharp breakdown and subnanoampere current out to over 60 V reverse bias. Although not conclusive, this result indicates that the soft breakdown is associated with residual defects and/or the high carrier concentration ($> 2 \times 10^{17} \text{ cm}^{-3}$) in the Si-implanted regions.

Figure I-13(a-d) shows the scanned photoresponses of a typical diode at reverse biases of 2 and 18.2 V. Figures I-13(a) and (c) show the photoresponse at 2 and 18.2 V, respectively, superimposed on the lower raster scan pattern. Figures I-13(b) and (d) show the horizontal scans of (a) and (c), respectively, superimposed so that relative magnitudes are more easily discernible. At 2 V reverse bias, the photoresponse is relatively flat. There is a slight amount of enhanced edge response due to the junction coming to the surface. There is also a slight amount of enhanced response in the central portion of the diode. This latter effect is probably due to the slightly shallower junction depth expected in the central region, as discussed above. At 18.2 V reverse bias, the photoresponse in the central region is uniform and greater than 7 times that at 2 V reverse bias, while the photoresponse in the outer rim is essentially the same as observed at 2 V. The depression in the photoresponse in the center is due to the Au-Mg contact and the lead wire. The dark current of this particular diode is less than 10^{-10} A at 2 V and 10 μA at 18.2 reverse bias. Although a few diodes showed photoresponse gains as high as 20, the central photoresponse of a typical diode with a 1-k Ω load generally peaked at a gain of 6 to 8. This is shown in Fig. I-14, which shows the relative photoresponse of the central region vs reverse bias for a typical diode with a 1-k Ω load. Slightly higher gains could be obtained by lowering the load resistance. Furthermore, as the photoresponse in the central portion began to saturate with increasing reverse bias, the photoresponse in the outer rim, which generally showed no photocurrent gain, began to decrease. These results indicate that the photoresponse gain is being limited by the diode impedance, i.e., the differential resistance of the current-voltage characteristics.

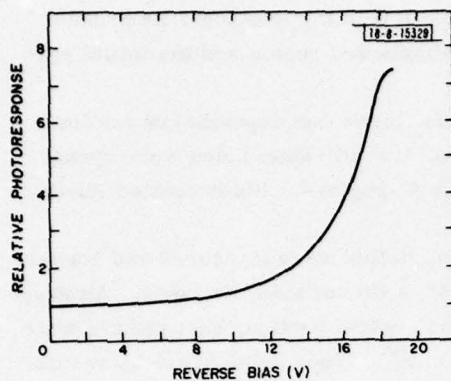


Fig. I-14. Relative photoresponse vs reverse bias of central portion of a typical InP diode with a 1-k Ω load.

Fig. I-15. Cleaved cross section of a diffused stripe (DS) GaInAsP/InP double-heterostructure (DH) diode laser.

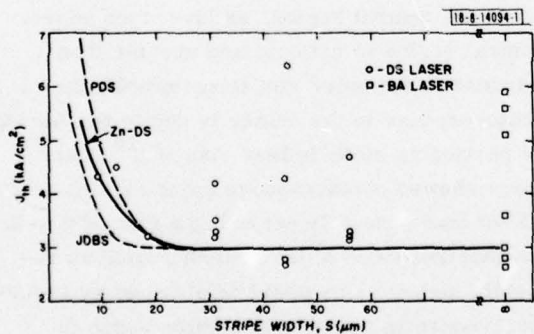
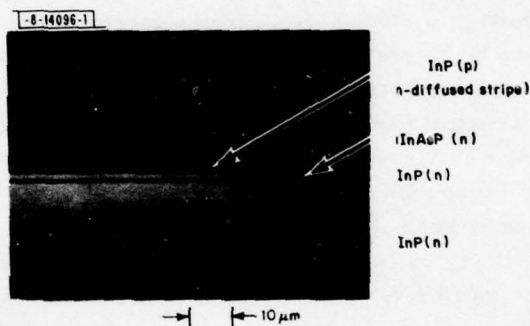


Fig. I-16. Threshold current density (J_{th}) as a function of stripe width (S) for DS and broad-area (BA) lasers fabricated by Zn diffusion.

In conclusion, guarded-planar avalanche diodes in InP have been fabricated which exhibit uniform avalanche photocurrent gain. At present, the magnitude of the photoresponse gain is limited by the dark current of the diodes. It should be stressed that these devices are in an early stage of development, and improvements are anticipated by optimization of both the epitaxial starting material and the ion-implantation fabrication steps.

J. P. Donnelly V. Diadiuk
C. A. Armiento S. H. Groves

E. Zn-DIFFUSED, STRIPE-GEOMETRY GaInAsP/InP DIODE LASERS

Planar Zn diffusion, a simple and accurately controllable process, is a standard technique in the fabrication of devices using III-V compounds and alloys, but it has not been widely employed in fabricating double-heterostructure (DH) GaAs/GaAlAs diode lasers because there are conflicting reports concerning its effect on the reliability of these devices. The degradation mechanisms of GaInAsP/InP and GaAs/GaAlAs lasers appear to be quite different, however. We therefore decided to investigate the utilization of deep Zn diffusion to fabricate stripe-geometry, DH GaInAsP/InP diode lasers with emission wavelengths in the 1.2- to 1.3- μm range. We found that efficient, reliable lasers can be obtained by this technique, although accurate control of the diffusion depth is required for optimum laser performance.

In preparing conventional GaInAsP/InP stripe-geometry lasers, an n-InP buffer layer ($n \sim 2 \times 10^{18} \text{ cm}^{-3}$), n-GaInAsP active region ($n \sim 10^{16}$ to 10^{17} cm^{-3}), and p-InP cap layer ($p \sim 10^{18} \text{ cm}^{-3}$) are grown successively by liquid-phase epitaxy (LPE) on an n-InP substrate, and stripes are defined either by proton bombardment²³ or by deposition of an oxide coating^{24,25} on the upper InP surface. The diffused-stripe (DS) devices described here utilize similar LPE-grown structure, except that the upper InP layer is n-type ($n \sim 10^{16}$ to 10^{17} cm^{-3}) rather than p-type. To define the stripes, a coating of SiO_2 or PSG is deposited on the upper InP surface, windows of the desired width are opened in the coating, and Zn is diffused through the windows to convert the upper InP layer and the GaInAsP layer to p-type ($p \sim 10^{18} \text{ cm}^{-3}$). Diffusion is accomplished by annealing in an evacuated, sealed fused-silica ampoule, using ZnP_2 as the source of Zn. The upper InP layer is 2 to 3 μm thick, and the GaInAsP layer is 450 to 2000 \AA thick. After growth, the substrate side of the wafer is lapped down to $\sim 75 \mu\text{m}$, and contacts of Au/Zn and Au/Sn are applied to the stripe and substrate sides of the device.

Figure I-15 shows the cleaved cross section of a DS laser in which the stripe was formed by diffusing Zn through an opening 13 μm wide. In this case, the diffusion front stopped at the interface between the GaInAsP active layer and the n-InP buffer layer (where the p-n junction is about 16 μm wide), and optical guiding is observed within the stripe cavity under both spontaneous and lasing conditions. Satisfactory lasers are formed only if the diffusion front stops at the interface. If the front fails to reach the interface, no index guiding is observed and the near-field emission in the spontaneous mode behaves like that of an oxide-defined-stripe laser. In addition, the threshold current is high, external quantum efficiency (η_D) is low, and the emission wavelength is shorter. On the other hand, if the diffusion extends beyond the interface by even a few tenths of a micrometer into the InP buffer layer, a twin-laser diode is formed, with laser action occurring within the quaternary layer near the two sides of the stripe. For such diodes, η_D is low and the output linearity is poor.

Figure I-16 shows the threshold current density (J_{th}) as a function of stripe width (S) for pulsed operation of a number of DS and broad-area (BA) lasers from a Zn-diffused wafer in which

18-8-15159-1

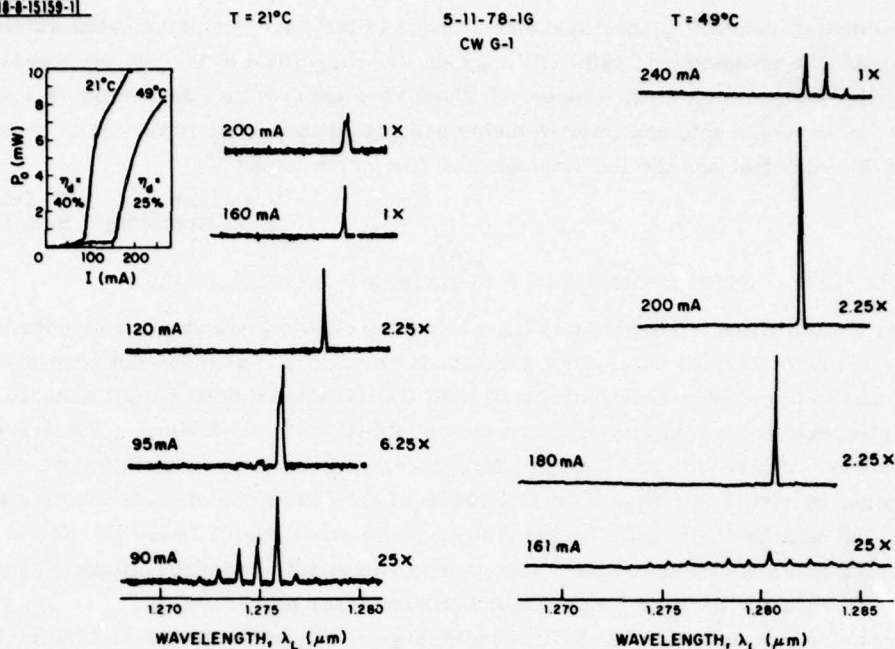


Fig. I-17. Emission spectra for CW operation of a DS laser (S = 9 μm) at heatsink temperatures of 21° and 49°C. Inset: output power (P_O) vs current (I) at the two temperatures.

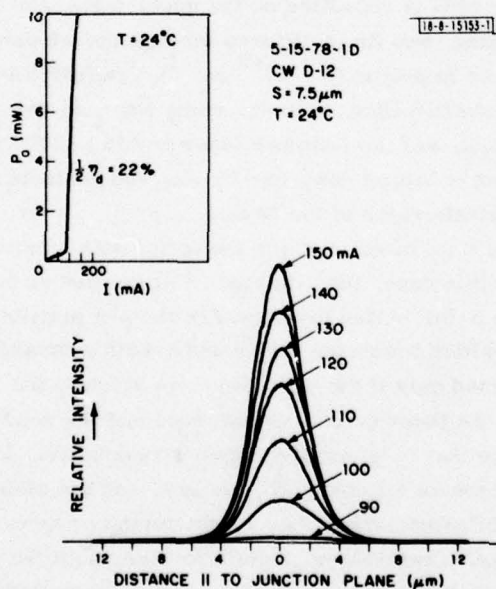


Fig. I-18. Near-field emission measured with a Ge detector for room-temperature CW operation of a DS laser (S = 7.5 μm). Inset: P_O vs I.

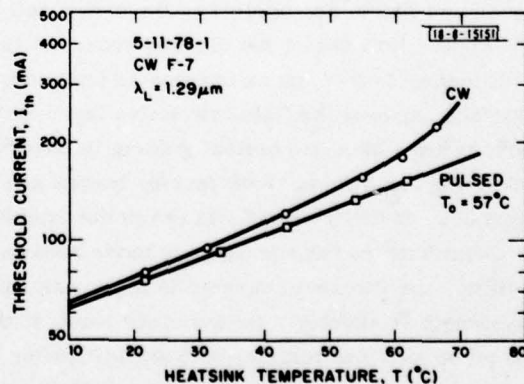


Fig. I-19. Threshold current (I_{th}) as a function of heatsink temperature for pulsed and CW operation of a DS laser.

the diffusion front stopped at the active-layer/buffer-layer interface, as in Fig. I-15. The BA devices ($S = \infty$) were fabricated in the same way as the DS lasers except that no oxide mask was used during diffusion. The J_{th} values for both DS and BA devices exhibit more scatter than obtained for proton-defined-stripe (PDS)²³ or oxide-defined-stripe (ODS)²⁴ lasers. For the DS lasers, with decreasing S the lowest J_{th} value for each stripe width remains about the same ($\sim 3 \text{ kA/cm}^2$) until S reaches $30 \text{ }\mu\text{m}$, below which J_{th} increases rapidly. For $S \leq 10 \text{ }\mu\text{m}$, J_{th} is lower for the best DS lasers than for PDS devices, but junction-defined, buried-stripe (JDBS) lasers have still lower thresholds.²⁴ For pulsed operation, the DS lasers show total optical confinement within the S for drive currents up to 6 times threshold.

Lasers with sufficiently narrow stripes generally exhibit single-mode emission. Emission spectra for CW operation of such a laser with $S = 9 \text{ }\mu\text{m}$ and cavity length (L) of $250 \text{ }\mu\text{m}$ are shown in Fig. I-17 for heatsink temperatures of 21° and 49°C . For operation up to about 40°C , η_d is nearly constant at ~ 40 percent/facet, but it decreases rapidly at higher temperatures. The spectra at both 21° and 49°C show single-mode operation at most current levels. Multimode emission occurs only within narrow current ranges (5 to 10 mA at 21°C) over which the output shifts rapidly to longer-wavelength modes with increasing current. The wavelength shift over these current ranges is about one to two mode spacings (10 to $20 \text{ }\text{\AA}$). For a particular longitudinal mode, at 21°C the shift in wavelength with current is insignificant up to $\sim 200 \text{ mA}$, but at 49°C the shift is of the order of $0.1 \text{ }\text{\AA}/\text{mA}$ for currents up to $\sim 300 \text{ mA}$. With increasing heatsink temperature, the wavelength of a particular mode increases at the rate of $0.85 \text{ }\text{\AA}/\text{K}$. This is much less than the values of 3 to $5 \text{ }\text{\AA}/\text{K}$ reported²⁵ for multimode lasers, which include shifts due to mode instability, but is the same as observed²⁶ for GaInAsP/InP lasers with distributed Bragg reflectors.

The DS lasers also exhibit good lateral-mode stability. Figure I-18 shows the near-field emission measured by scanning a Ge detector parallel to the junction plane of a laser with $S = 7.5 \text{ }\mu\text{m}$, $L = 175 \text{ }\mu\text{m}$, and emission wavelength (λ_L) of $1.30 \text{ }\mu\text{m}$. The laser output is linear up to 6 mW , and η_d is 22 percent/facet. The emission shows a single lateral mode. For drive currents up to 140 mA , the peak of the near-field pattern is almost stationary; at higher currents, the peak begins to shift but the lowest-order mode still dominates.

The lowest threshold current (I_{th}) that has been achieved for room-temperature CW operation of the DS lasers is 70 mA (corresponding to $J_{th} = 2.8 \text{ kA/cm}^2$), for devices with $L = 280 \text{ }\mu\text{m}$. The temperature dependence of I_{th} is generally greater for DS lasers than for PDS devices with the same emission wavelength. For example, the laser of Fig. I-17 has I_{th} values of 86 and 156 mA for CW operation at 20° and 50°C , respectively — an increase of ~ 80 percent compared with ~ 60 percent that we have observed for PDS devices over the same temperature range. Figure I-19 shows I_{th} for pulsed and CW operation of another DS laser ($\lambda = 1.29 \text{ }\mu\text{m}$) as a function of heatsink temperature. Between 20° and 60°C , I_{th} (pulsed) can be approximated as $I_0 (\exp T/T_0)$, with $T_0 = 57^\circ\text{C}$, compared with T_0 values of 80° to 90°C for PDS lasers. As shown in Fig. I-19, CW operation of this laser has been achieved at heatsink temperatures as high as 66°C . The thermal impedance, as determined from the difference between pulsed and CW values of I_{th} , is about 20°C/W near room temperature and increases to 30°C/W near 60°C . This increase in thermal impedance is not currently understood. In view of the observed dependence of emission wavelength on drive current, the change in impedance does not seem to result from the Seebeck effect, as is reported²⁷ to be the case for ODS GaAs/GaAlAs diode lasers.

Life tests are in progress on two DS lasers that are in CW operation at room temperature with power inputs of a few milliwatts. Both devices have already logged over 6300 hr. On the basis of these very limited results, it appears that DS devices are comparable in reliability to conventional GaInAsP/InP PDS lasers.

J. J. Hsieh

REFERENCES

1. M. D. Blue, Phys. Rev. 134, A226 (1964).
2. R. H. Kingston, Detection of Optical and Infrared Radiation (Springer, New York, 1978), pp. 64-76.
3. B. J. Peyton, A. J. DiNardo, G. M. Kanischak, F. R. Arams, R. A. Lange, and E. W. Sard, IEEE J. Quantum Electron. QE-8, 252 (1972).
4. D. L. Spears, I. Melngailis, and T. C. Harman, Digest of Technical Papers, 1975 IEEE/OSA Conf. on Laser Engineering and Applications, May 28-30, 1975, Washington, D. C. (IEEE, New York, 1975) p. 79; and Solid State Research Report, Lincoln Laboratory, M.I.T. (1976:3), pp. 5-11, DDC AD-A034647/8.
5. D. L. Spears, Infrared Phys. 17, 5 (1977), DDC AD-A046982/5.
6. R. T. Ku and D. L. Spears, Opt. Lett. 1, 84 (1977), DDC AD-A050857/2.
7. See F. Auracher and H. H. Witte, Opt. Commun. 13, 435 (1975), and cited references.
8. B. Lax and K. J. Button, Microwave Ferrites and Ferrimagnetics (McGraw-Hill, New York, 1962).
9. H. Piller, Proc. Int. Conf. Phys. of Semiconductors, Paris, 1964, p. 299.
10. W. G. Spitzer and J. M. Whelan, Phys. Rev. 114, 59 (1959).
11. Solid State Research Report, Lincoln Laboratory, M.I.T. (1977:4), p. 1, DDC AD-A052463/7.
12. C. E. Hurwitz and J. J. Hsieh, Appl. Phys. Lett. 32, 487 (1978), DDC AD-A060752.
13. M. Ito, T. Kaneda, K. Nakajimo, Y. Toyoma, T. Yamaoka, and T. Kotani, Electron. Lett. 14, 418 (1978).
14. Y. Takanashi and Y. Horikoshi, Jpn. J. Appl. Phys. 17, 2065 (1978).
15. H. Law, L. R. Tomasetta, and K. Nakano, Appl. Phys. Lett. 33, 920 (1978).
16. C. A. Armiento, J. P. Donnelly, and S. H. Groves, Appl. Phys. Lett. 34, 229 (1979).
17. J. J. Berenz, F. B. Frank, and T. L. Hierl, Electron. Lett. 14, 683 (1978).
18. H. W. Rugg, IEEE Trans. Electron Devices ED-14, 239 (1967).
19. P. Webb and A. R. Jones, IEEE Trans. Nucl. Sci. NS-21, 151 (1974).
20. J. P. Donnelly and C. A. Armiento, Appl. Phys. Lett. 34, 96 (1979).
21. W. T. Devlin, K. T. Ip, D. P. Leta, L. F. Eastman, G. H. Morrison, and J. Comas, presented at 7th International Symposium on GaAs and Related Compounds, St. Louis, Missouri, 24-27 September 1978.

22. J. P. Donnelly and C. E. Hurwitz, Appl. Phys. Lett. 31, 418 (1977), DDC AD-A050856/4.
23. J. J. Hsieh, J. A. Rossi, and J. P. Donnelly, Appl. Phys. Lett. 28, 709 (1976), DDC AD-A028550/2.
24. J. J. Hsieh and C. C. Shen, Appl. Phys. Lett. 30, 429 (1977), DDC AD-A063419.
25. T. Yamamoto, K. Sakai, S. Akiba, and Y. Suematsu, IEEE J. Quantum Electron. QE-14, 95 (1978).
26. H. Kawanishi, Y. Suematsu, Y. Itaya, and S. Arai, Jpn. J. Appl. Phys. 17, 1439 (1978)
27. L. Yang, R. T. Lynch, Jr., and R. Y. Hung, 1978 IEEE International Laser Conference, San Francisco.

II. QUANTUM ELECTRONICS

A. HIGH-REPETITION-FREQUENCY MINI-TEA CO₂ LASERS

In our efforts to construct a miniaturized TEA CO₂ (mini-TEA) laser system with high pulse repetition frequency (PRF) and good mode quality, we previously reported achieving a PRF in excess of 200 Hz using an arrangement in which the gas flowed transversely through the active laser volume and directly into the atmosphere.¹ At 200 Hz and 1.5 clearing ratio, the gas consumption rate is over 40 l/min. For higher PRF and the larger clearing ratios needed to obtain the highest power levels available, the gas dissipation rate becomes excessive. For this reason, we decided to build a semi-open circulating gas-flow laser system in which a small fraction of the gas flowing through the laser region is continuously replaced.

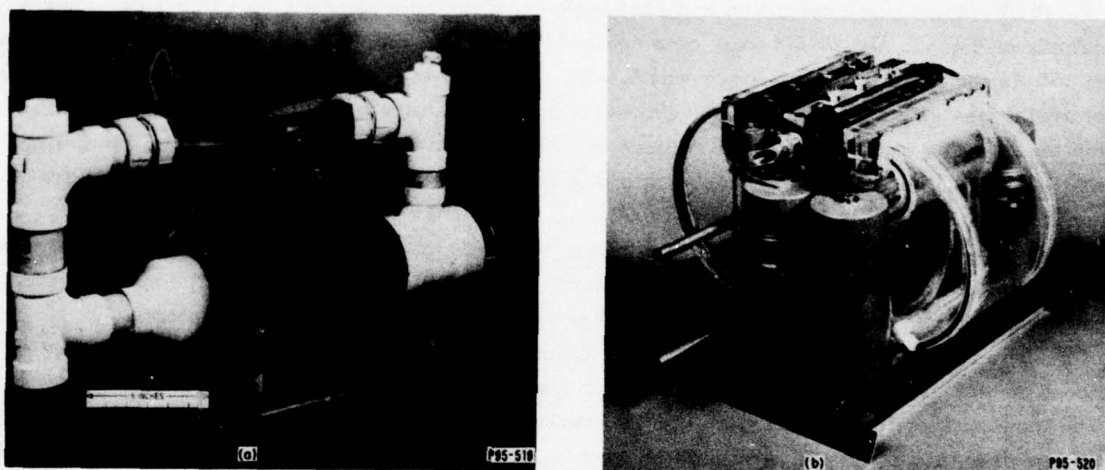


Fig. II-1. High-repetition-rate circulating gas-flow mini-TEA CO₂-laser systems: (a) tubular unit; (b) cylindrical unit.

Two distinct systems were designed and constructed; they are shown in Figs. II-1(a) and (b). Both were designed for use with the original laser body and UV preionizer,² and employ a single, resonantly charged, thyatron-activated firing circuit for both the preionization and main discharges. A description of these systems, along with a discussion of their operation at high PRF, is given below.

1. Tubular Unit

The tubular unit [Fig. II-1(a)] consists of a simple recirculating system built of 10- and 5-cm plastic tubing and two Plexiglas pieces shaped to permit a transition between the tubing and the laser body while maintaining a constant cross section for the gas flow. The 10-cm tubing section contains a heat exchanger and a 7.5-cm-diam recirculating fan. The unit was normally operated at a gas-bleeding rate of 5 l/min., but it has operated arc-free for several minutes at 400 Hz with a bleedthrough rate slightly below 1 l/min.

The laser has been run at capacitor charging voltages between 11 and 18 kV. Per-pulse energy outputs of 45, 40, and 21 mJ have been obtained at PRFs of 100, 200, and 500 Hz, respectively. Thus, at 500 Hz the mini-TEA laser achieved an average output power level of 10.5 W. This laser system was used in the second-harmonic-generation (SHG) experiments discussed below.

2. Cylindrical Unit

This unit [Fig. II-1(b)] consists of two semi-cylinders of equal length placed nonconcentrically on each side of the laser so that their spacing at the top is equal to the laser interelectrode distance (4 mm), while the spacing at the bottom is sufficiently large to hold a fan and a heat exchanger. Short constant-area spacers are placed between the laser body and the semi-cylinders to reduce turbulence in the active region. Due in large measure to these shorter constant-area flow sections, this system is considerably more compact than the tubular unit.

Preliminary laser operation tests have been performed with this unit. Per-pulse energy outputs of 55, 43, and 27 mJ were obtained at PRFs of 50, 200, and 350 Hz, respectively. Thus, at 350 Hz the average output power was 9.5 W. The highest frequency obtained before the onset of arcing was slightly over 400 Hz. However, the present system is operating with a smaller fan than the one in the tubular unit. Since the PRF is limited by the gas-flow rate, we believe that the introduction of the larger fan into this unit will increase the ultimate achievable frequency to above 500 Hz for this system as well; this will be tested shortly.

The higher pulse energy levels obtained at low PRF in the cylindrical unit are probably due mainly to differences in stray circuit inductance since the laser geometry in the active region, the electronics, and the optical components are nominally identical in both systems.

The outputs of both units are in low-order transverse modes, because the small active cross-sectional area (4×4 mm) of the laser is comparable to the area of the TEM_{00} cavity mode. The mode quality is maintained at high repetition rates because of the rapid removal of the discharge gases from the active volume between pulses. The TEM_{10} appeared to be the dominant mode at the highest output power levels, and approximately half the laser power was available in the TEM_{00} mode by placing apertures in the cavity.

Each of the units meets the original design criteria, which were for a simple, compact unit with sufficient gas-flow stability and velocity to provide a high PRF (~ 500 Hz) with pulses of good mode quality at energy levels approaching 20 mJ.

These mini-TEA lasers are to be used as the fundamental frequency pump for SHG in conjunction with $CdGeAs_2$ as the nonlinear frequency-doubling crystal.³ Good mode quality of the laser output is particularly important for SHG, where a fundamental Gaussian beam is desirable for high conversion efficiency. To establish the efficacy of the mini-TEA laser for this application, SHG experiments were carried out with the tubular laser system providing the fundamental pump frequency at PRFs of 350 and 405 Hz. The results are shown in Figs. II-2(a) and (b), respectively. To obtain these results, the CO_2 -laser beam was weakly focused through a BaF_2 lens to a calculated spot size of $700 \mu m$ at the $CdGeAs_2$ sample face. The sample was antireflection-coated and cooled to liquid-nitrogen temperature. The input to the nonlinear crystal was varied by placing filters of varying transmittance between the laser output and the focusing lens.

The results show that the mini-TEA laser output takes the SHG process well into a saturation regime; observation of the square-law dependence of $P(2\omega)/P(\omega)$ is limited to input levels

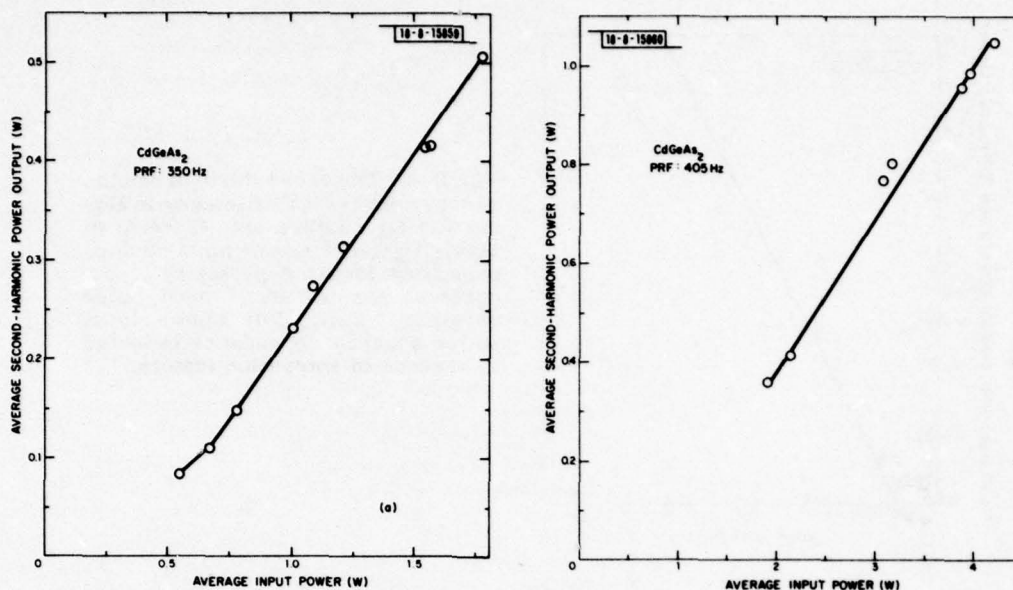


Fig. II-2. Average second-harmonic power generated by CdGeAs₂ crystal as a function of average power from a mini-TEA CO₂ laser. (a) PRF = 350 Hz; (b) PRF = 405 Hz.

well below 1 W, that is, to the three lowest points in Fig. II-2(a). The top point in Fig. II-2(a) corresponds to an average power second-harmonic conversion efficiency of over 28.5 percent, which is the highest value reported to date for CO₂-laser frequency doubling. The SHG at 405 Hz was carried out at somewhat higher laser pump energy and, as shown in Fig. II-2(b), yielded a power level over 1 W, corresponding to a 2.5-mJ pulse energy and a peak power well above 25 kW at the doubled frequency.

N. Menyuk
P. F. Moulton

B. MAXIMUM EFFICIENCY OF A TWO-PHOTON RESONANT THIRD-HARMONIC-GENERATION PROCESS

The highest energy conversion efficiency observed for a two-photon resonant third-harmonic generation (THG) process is 4 percent. This was obtained⁴ for tripling CO₂-laser radiation in a liquid CO-O₂ mixture using a tight-focusing geometry (1-cm confocal parameter in a 10-cm cell) in a double-pass configuration. A mirror was used to refocus both the fundamental and the third-harmonic beams back into the cell. The conversion efficiency saturated at an input power level approximately a factor-of-4 below the laser-induced-breakdown threshold for the 8-nsec duration CO₂-laser pump pulses at 9.35 μ m used in the experiments. Figure II-3 shows the dependence of the observed conversion efficiency on the CO₂ input power for a CO-O₂ mixture with a 0.083 relative CO peak absorbance. The latter is approximately proportional to the relative CO concentration.⁵ We have varied the relative CO concentration from 5 to 25 percent and, in each case, have added SF₆ to optimize the phasematching condition.⁶ The efficiency always saturated at about the same level. The above variation in CO concentration corresponds to a 0.15-cm⁻¹ tuning of the vibrational two-photon resonance in CO, which has a typical linewidth of about 0.2 cm⁻¹ at these CO concentrations.⁷ Although the THG efficiency saturates, we have

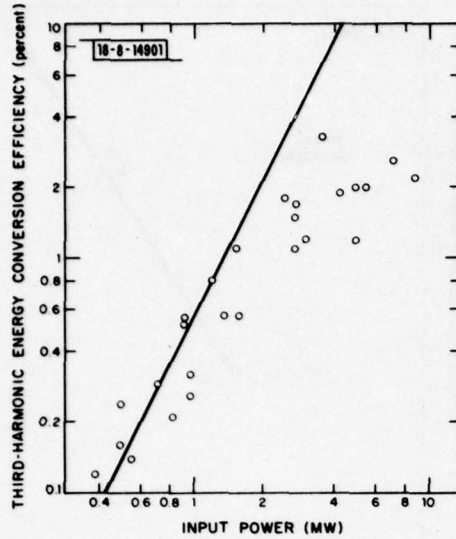


Fig. II-3. Observed third-harmonic energy conversion efficiency in liquid CO-O₂ mixture as a function of input CO₂-laser power for a double-pass tight-focusing geometry (1-cm confocal parameter, 8-nsec pulse duration). Solid line shows input power squared dependence expected in absence of saturation effects.

not observed any nonlinear attenuation of the CO₂ beam as it passes through the cell. From these experiments, it is clear that the saturation behavior cannot be explained by either breaking of the phasematching condition due to field-induced refractive index changes or pump depletion due to two-photon absorption. Neither can the results be explained by any of the other limiting mechanisms discussed in Ref. 7.

In order to explain the above results, we have examined theoretically a general two-photon resonant THG process. Our calculations show that the ultimate THG efficiency is limited by an interference phenomenon between THG, two-photon-absorption, and Raman-scattering processes. Furthermore, incorrect conclusions are reached if these processes are considered independently. The coupled-wave equations, in MKS units, that describe the THG process for a plane-wave geometry with beam propagation in the z -direction are given by

$$\begin{aligned} \frac{\partial E_3}{\partial z} = & -i \frac{3\eta_3\omega_1}{8} \{ \chi_{\text{res}}^{(3)} [E_1^3 e^{i\Delta kz} + 2E_3 |E_1|^2] \\ & + \chi^{(3)}(\omega_1, \omega_1, \omega_1) E_1^3 e^{i\Delta kz} + 6\chi^{(3)}(\omega_3, \omega_1, -\omega_1) E_3 |E_1|^2 \\ & + 3\chi^{(3)}(\omega_3, \omega_3, -\omega_3) E_3 |E_3|^2 \} \end{aligned} \quad (\text{II-1a})$$

$$\begin{aligned} \frac{\partial E_1}{\partial z} = & -i \frac{\eta_1\omega_1}{8} \{ [2\chi_{\text{res}}^{(3)} + \chi_{\text{res}}^{(3)*}] E_3 E_1^{*2} e^{-i\Delta kz} + 2\chi_{\text{res}}^{(3)*} E_1 |E_3|^2 \\ & + \chi_{\text{res}}^{(3)} E_1 |E_1|^2 + 3\chi^{(3)}(\omega_3, -\omega_1, -\omega_1) E_3 E_1^{*2} e^{-i\Delta kz} \\ & + 6\chi^{(3)}(\omega_1, \omega_3, -\omega_3) E_1 |E_3| + 3\chi^{(3)}(\omega_1, \omega_1, -\omega_1) E_1 |E_1|^2 \} \end{aligned} \quad (\text{II-1b})$$

where E_1 and E_3 are the electric-field amplitudes at the fundamental and the third-harmonic frequencies, respectively; $\{E(t, z) = \text{Re} [E e^{i(\omega t - kz)}]\}$; η_1 and η_3 are the wave impedances (376.8 Ω /refractive index); and $\Delta k = k_3 - 3k_1$ is the wave-vector mismatch. The quantities $\chi^{(3)}(\omega_1, \omega_1, \omega_1) \approx \chi^{(3)}(\omega_3, -\omega_1, -\omega_1)$, $\chi^{(3)}(\omega_3, \omega_1, -\omega_1) \approx \chi^{(3)}(\omega_1, \omega_3, -\omega_3)$, and $\chi^{(3)}(\omega_3, \omega_3, -\omega_3) \approx \chi^{(3)}(\omega_1, \omega_1, -\omega_1)$,

which constitute the nonresonant contributions to the third-order susceptibility tensor, are assumed real. The two-photon resonant contribution is given by⁵

$$\chi_{\text{res}}^{(3)} = K \frac{\Delta\omega/2}{\omega_0 - 2\omega_1 + i\Delta\omega/2} \quad (\text{II-2})$$

where K is a real positive quantity, ω_0 is the vibrational resonance frequency, and $\Delta\omega$ is the linewidth of the two-photon resonance.

There is an exchange of energy between the two electromagnetic fields and the material system corresponding to the parametric interaction, two-photon absorption, and Raman scattering. The Raman process produces gain at ω_1 and loss at ω_3 . Using Eqs. (II-1a) and (II-1b), we calculate the attenuation of the total electromagnetic intensity as:

$$\begin{aligned} \frac{\partial}{\partial z} \left(\frac{|E_3|^2}{2\eta_3} + \frac{|E_1|^2}{2\eta_1} \right) &= \frac{\omega_1}{2} \text{Im} \chi_{\text{res}}^{(3)} \{ (|E_3|^2 + |E_1|^2/4) |E_1|^2 \\ &+ \text{Re} [E_3^* E_1^3 e^{i\Delta kz}] \} \end{aligned} \quad (\text{II-3})$$

where the first and second terms on the right-hand side of Eq. (II-3) represent losses due to the Raman scattering and two-photon absorption, respectively. The third term can either be negative (energy flow from material system to fields) or positive, depending on the relative phases.

When the phasematching condition $\Delta k = 0$ is satisfied and far from resonance where $\text{Im} \chi_{\text{res}}^{(3)} \ll [\text{Re} \chi_{\text{res}}^{(3)} + \chi^{(3)}(\omega_1, \omega_1, \omega_1)]$, it follows from Eq. (II-1a) that the generated third-harmonic signal is 90° out of phase with the fundamental beam. On resonance, however, where $\text{Im} \chi_{\text{res}}^{(3)} \gg [\text{Re} \chi_{\text{res}}^{(3)} + \chi^{(3)}(\omega_1, \omega_1, \omega_1)]$, there is a 180° phase difference. This difference in relative phases affects the parametric term in Eq. (II-1b), which gives rise to gain or loss depending on the resonance condition. On resonance there is gain, which reduces the effects of the two-photon-absorption term, i.e., the total attenuation at the fundamental frequency is smaller than that calculated from the two-photon-absorption cross section neglecting the THG process.

If the nonresonant terms in Eqs. (II-1a) and (II-1b) are ignored, it can be shown that $\partial E_3 / \partial z = \partial E_1 / \partial z = 0$ when

$$E_1^2 e^{i\Delta kz} + 2E_3 E_1^* = 0 \quad (\text{II-4})$$

is satisfied. The THG and the absorptive processes then saturate, even though the generated third-harmonic intensity is only one-quarter of the transmitted intensity at the fundamental frequency.

For exact resonance, neglecting the nonresonant contributions to $\chi^{(3)}$, the THG efficiency and the nonlinear absorption can be calculated analytically; solving Eqs. (II-1a) and (II-1b) with $\Delta k = 0$ and assuming the boundary conditions $E_3 = 0$ and $E_1 = E_1(0)$ give the transcendental expression

$$3E_1^2 - E_1 E_3 + E_3^2 = 3E_1(0)^2 \exp \left[-\frac{2}{\sqrt{11}} \arctan \frac{\sqrt{11}}{1 - 6E_1/E_3} \right]. \quad (\text{II-5})$$

The intensity at the third-harmonic frequency grows monotonically until it saturates at $E_1 = -2E_3$, which substituted into Eq. (II-5) gives a maximum THG efficiency of 17 percent. At this conversion level, the nonlinear absorption is 14 percent; thus, 69 percent of the fundamental beam power is transmitted through the nonlinear medium. The fundamental and third-harmonic beams

propagate in the nonlinear medium without further exchange of energy, regardless of the intensity level or medium length.

We have numerically calculated the THG power conversion efficiency including the nonresonant susceptibility terms for the liquid CO-O₂ system for arbitrary detuning using Eqs. (II-1a) and (II-1b) and assuming a collimated beam geometry with a TEM₀₀ mode incident laser beam. Electrostriction, molecular reorientation, and the nonlinear electronic polarizability all contribute to the nonresonant third-order susceptibility tensor. The electrostrictive effect, however, has a slow response time given approximately by the ratio of the laser spot size to the acoustic velocity (~100 nsec for a 100-μm spot size). This effect can therefore be ignored for pump pulses of a few-nanoseconds duration. The molecular reorientation effect, with a typical relaxation time of 10⁻¹² sec, contributes only to the AC Kerr effect; the corresponding third-order susceptibility tensor satisfies the relation $\chi^{(3)}(\omega_1, \omega_1, -\omega_1) = 2\chi^{(3)}(\omega_3, \omega_1, -\omega_1)$. When this is used in Eqs. (II-1a) and (II-1b), it can be shown that the Kerr terms due to molecular reorientation cancel when the equations are combined to calculate the THG efficiency. It is therefore only necessary to include the nonlinear electronic polarizability in the nonresonant terms. The third-order nonresonant electronic susceptibility, $\chi_{el}^{(3)}$, is smaller than the nonlinearity due to molecular reorientation in liquids such as CO-O₂ mixtures. Our measured value relative to the peak value of $\chi_{res}^{(3)}$ in CO-O₂ is $\chi_{el}^{(3)} = 0.015$ K at a CO peak absorption of 8 percent. The tensor has the properties $\chi_{el}^{(3)} = \chi^{(3)}(\omega_1, \omega_1, \omega_1) = \chi^{(3)}(\omega_1, \omega_1, -\omega_1) = \chi^{(3)}(\omega_3, \omega_1, -\omega_1)$.

Figure II-4 shows the results of a numerical calculation of the third-harmonic power conversion efficiency for $\Delta k = 0$ in liquid CO-O₂ (8-percent CO peak absorbance). The figure gives

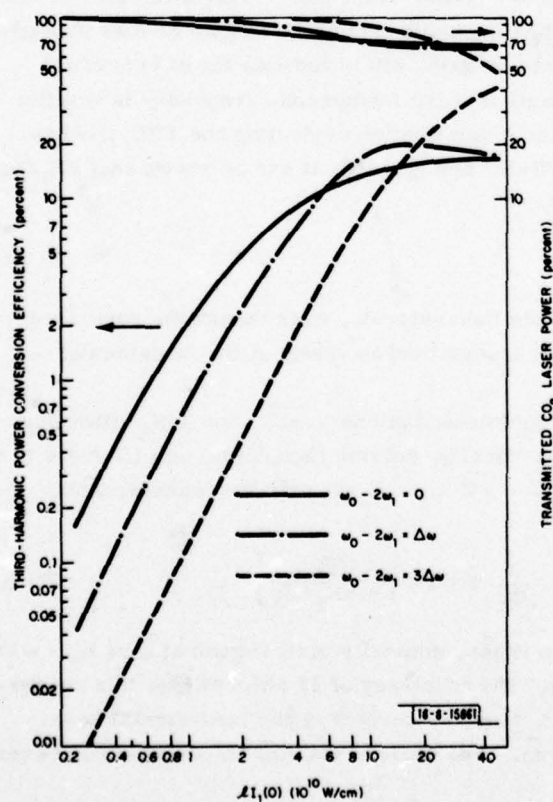


Fig. II-4. Calculated power conversion efficiency for a two-photon resonant THG process in a liquid CO-O₂ mixture assuming a collimated beam geometry.

the dependence of the conversion efficiency on the product of the cell length l times the CO_2 input intensity $I_1(0)$ for exact two-photon resonance and for a detuning corresponding to one and three linewidths. The figure also shows the transmitted CO_2 pump power. The total power attenuation due to two-photon absorption and Raman scattering at $lI_1(0) = 5 \times 10^{11} \text{ W/cm}$ is 13.7 percent on resonance, and 14.2 and 8.7 percent for a detuning of $\Delta\omega$ and $3\Delta\omega$, respectively.

It is assumed in Fig. II-4 that the pump laser is detuned to the low-frequency side of the two-photon resonance. Detuning in the opposite direction results in slightly lower conversion efficiencies; thus, higher input intensities are required to reach maximum conversion. This is due to interference effects between the resonant and nonresonant third-order susceptibility tensors.

The calculations show that higher conversion efficiencies are attainable when the pump laser is tuned slightly off the two-photon resonance, provided that no other limiting mechanisms such as laser-induced breakdown become important. For reference, the laser-induced breakdown threshold in liquid CO-O_2 mixtures for a 120- μm spot size is about $3 \times 10^{10} \text{ W/cm}^2$ for 8-nsec pulses, and the threshold is inversely proportional to the spot size and the square root of the pulse duration.

The CO-O_2 system using the R(6) pump line cannot be detuned by more than a linewidth by changing the liquid mixing ratio. It is still possible, however, to increase the conversion efficiency beyond the 17-percent level (at exact resonance) by adopting a multipass technique in which only the fundamental beam is resonated, since there is only 14-percent power loss after a single transit through the nonlinear medium.

Our measured maximum energy conversion efficiency of 4 percent for a tight-focusing geometry may be consistent with the calculated maximum efficiency of 17 percent for collimated beams. For tight focusing, it is reasonable to expect a lower maximum efficiency since the phasematching condition is sensitive to phase distortions of the Gaussian beam profiles due to pump-depletion and Raman-scattering processes. Quantitative calculations, however, are more complex and have not been carried out.

H. Kildal
S. R. J. Brueck

C. FM MODE-LOCKED $\text{Nd}_{0.5}\text{La}_{0.5}\text{P}_5\text{O}_{14}$ LASER

Using the high-Nd-concentration material $\text{Nd}_{0.5}\text{La}_{0.5}\text{P}_5\text{O}_{14}[(\text{Nd}, \text{La})\text{PP}]$, we have constructed a FM mode-locked laser with output pulses ~ 14 psec wide at a repetition rate of 480 MHz. The primary advantages of this material are its wide fluorescence bandwidth ($\sim 25 \text{ cm}^{-1}$) and its large emission cross section, which simultaneously allow short laser pulses and low threshold CW operation.

The laser design, illustrated in Fig. II-5, uses an astigmatically compensated three-mirror cavity of the type commonly used for dye lasers.⁸ The small mode waist at the laser crystal provides a low threshold, while the long cavity arm where the phase modulator is inserted has a wide, nearly collimated beam. The laser crystal is 3.5 mm long with faces polished at Brewster's angle and a laser polarization along the highest gain "b" direction. $(\text{Nd}, \text{La})\text{PP}$ has been used rather than NdPP in order to lower the fluorescence concentration quenching and decrease the $^4I_{11/2}$ resonant absorption loss. Crystals were grown by the technique described in Ref. 9. Nearly all the pump radiation at 585 nm is absorbed in the crystal, except for a small amount used for alignment.

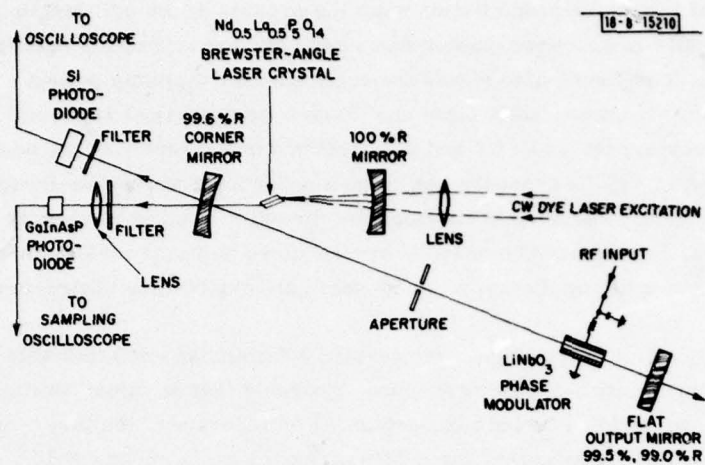


Fig. II-5. Schematic diagram of FM mode-locked Nd_{0.5}La_{0.5}P₅O₁₄ laser.

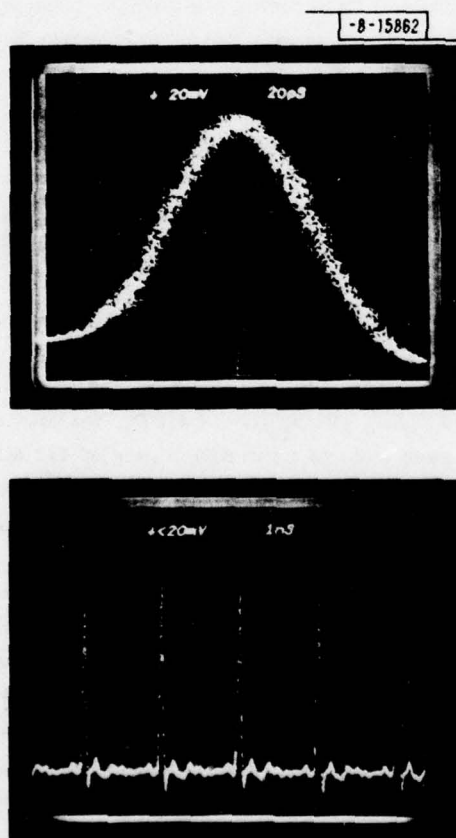


Fig. II-6. Mode-locked pulses from Nd_{0.5}La_{0.5}P₅O₁₄ laser detected by GaInAsP/InP photodiode.

The phase modulator is a crystal of LiNbO_3 , $4 \text{ mm}^2 \times 20 \text{ mm}$ long, mounted in a tuned package with $Q \approx 150$ to lower the RF drive power. The modulation depth at 633 nm has been measured with a HeNe laser and, using reported data on the electrooptic coefficients at 633 and 1060 nm (Ref. 10), the phase retardation in radians at the laser wavelength of 1050 nm was found to be $\delta \approx 0.5 \sqrt{P}$, where P is the power in watts. The optical length of the laser cavity, which was adjusted to match the 480-MHz center frequency of the modulator circuit, was about 31 cm.

The laser output was measured by several methods. At the partially transmitting corner mirror, one beam was detected with a relatively slow Si photodiode in order to monitor the average output power, and the other beam was focused onto a small-area GaInAsP photodiode whose output was put into a sampling oscilloscope (see also Sec. I-C). This output, with a detector-limited, minimum measured width of 80 psec as shown in Fig. II-6, was used for coarse alignment of the cavity and to monitor continuously the output pulse train. The beam from the flat output mirror was measured by three different methods: direct SHG enhancement with a $\text{Ba}_2\text{NaNb}_5\text{O}_{15}$ crystal, pulse intensity correlation with a scanning Michelson interferometer followed by the SHG crystal, and spectral measurement with a scanning Fabry-Perot interferometer.

Using two output mirrors with 0.5- and 1.0-percent transmission, thresholds of 23 and 28 mW were measured, with corresponding single-ended slope efficiencies of 5.6 and 9.7 percent, respectively. The round-trip nonresonant internal loss was calculated to be 1.4 percent. Typical single-ended average output powers were from 4 to 8 mW. The maximum measured SHG enhancement factor of 53 implies a pulse duration of ~ 13 psec, assuming a Gaussian pulse shape. The direct intensity correlation scans seemed to be more sensitive to the cavity alignment; the minimum measured correlation function width was 20 psec, implying a Gaussian pulse width of 14 psec. This is less than half the shortest value reported for CW Nd:YAG lasers.¹¹ With modulation power of 300 mW ($\delta \approx 0.27$) and cavity loss of 0.03, the pulse width calculated from the theory of Ref. 10 is 13.6 psec, in excellent agreement with the measurement. The product of the measured spectral width and pulse duration was ~ 0.66 , compared with the theoretical value of 0.624 (Ref. 10), showing that no significant extraneous frequency chirp was present.

The high gain density of (Nd, La)PP allows the use of very small laser crystals, with resulting advantages of lower dispersion and use of shorter laser cavities. With lower cavity loss, greater modulation, and higher modulation frequency, pulses less than 10 psec wide should be attainable. Development of suitable semiconductor lasers or LEDs to pump the 800-nm Nd^{3+} absorption band should enable development of a small and efficient (Nd, La)PP mode-locked laser.

S. R. Chinn
W. K. Zwickert†

D. Ce:YLF LASER

Stimulated emission from a $5d \rightarrow 4f$ transition in a triply ionized rare-earth doped crystal has been observed for the first time. Ce^{+3} ions in YLF (LiYF_4) were optically pumped at 249 nm and lased at 325 nm. This wavelength is the shortest ever obtained from an optically pumped solid-state laser. The characteristics of the Ce:YLF laser, because of the electric-dipole-allowed nature of the transition and the strong coupling between the $5d$ state and host lattice, differ strongly from more conventional rare-earth doped solid-state lasers. The laser

† Philips Laboratories, Briarcliff Manor, New York.

transitions in those devices occur between 4f levels and are characterized by long ($>10 \mu\text{sec}$) spontaneous emission lifetimes and narrow ($\sim 10 \text{ cm}^{-1}$) linewidths. In contrast, a lifetime of roughly 40 nsec and an emission linewidth of $\sim 1500 \text{ cm}^{-1}$ have been measured for the lowest-lying 5d level. Because of the short lifetime, large linewidth, and short wavelengths required for optical excitation, stimulated emission from Ce:YLF is most readily achieved by using an excimer gas laser for pumping. A KrF laser was used to longitudinally pump a 700- μm -thick plate of Ce:YLF (1-percent doping), placed in the center of a 5-cm-long optical cavity. The pump-laser pulse width was 25 nsec, FWHM. The threshold behavior of the Ce:YLF laser is shown in Fig. II-7; the nonlinear output response above threshold is probably due to heating effects in the crystal. The maximum output energy observed was $\sim 1 \mu\text{J}$, but the 1-percent-transmission output mirror undoubtedly resulted in severe undercoupling. The laser wavelength, 325 nm, was at the peak of the spontaneous emission spectrum.

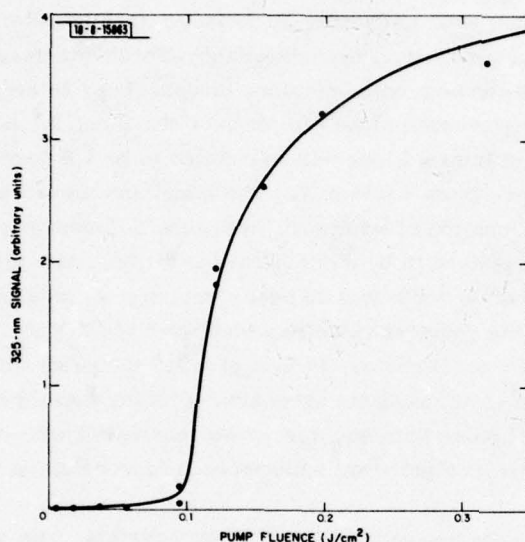


Fig. II-7. Threshold plot for Ce:YLF (325-nm) laser with KrF (249-nm) pumping.

Further experiments will have to be done, especially toward demonstrating wideband tunability, but the Ce:YLF laser, pumped by an excimer gas laser, has the potential for becoming a powerful source of tunable near-UV radiation.

D. J. Ehrlich
P. F. Moulton
R. M. Osgood, Jr.

E. ALKALI-METAL RESONANCE-LINE LASERS BASED ON PHOTODISSOCIATION

A series of new alkali-metal lasers has been obtained based on excitation by photodissociation of alkali-halide salts with the output of a small excimer laser. The lasers have important potential practical utility since all emit on the resonance lines of their respective alkali metals. High-intensity, pulsed resonance-line sources can be readily used as probes in remote sensing of alkali metals in chemical and atmospheric applications. The facts that these atomic lasers possess extremely low excimer-pump thresholds ($\sim 10 \mu\text{J}$) and that the salt-sample cells can be operated indefinitely on a single sample fill mean that small, simple resonance-line lasers are

feasible. The realization of such sources has been greatly simplified by the development of intense UV-laser pumps, principally excimer lasers and frequency-multiplied Nd:YAG lasers.¹² In this connection, there have been a number of recent reports of atomic photodissociation lasers including In (Ref. 13), Se (Ref. 14), Na (Ref. 15), and Tl (Ref. 16). However, we have found that photodissociation of alkali-halide salts is a technique with general applicability for producing resonance-line lasers. Further, important physical details regarding the photodissociation process are revealed by the properties of these lasers.

The experimental arrangement was similar to that previously described for the Tl laser.¹⁶ Pulses of ~1 to 10 mJ and 25-nsec duration from an ArF (193-nm) or a KrF (249-nm) laser were weakly focused into sealed, unbuffered sample cells containing the salt to be photodissociated. The cells were heated in ovens of various designs to temperatures as high as 1000°C. A copper cooling rod was inserted near the center of the cells to create a small cold spot away from the windows. The sample cells were constructed from standard 10-cm-path-length spectrometer cells of ultraviolet-grade fused silica. Each cell was subjected to vacuum bakeout for several hours, then filled with a few milligrams of alkali-halide salt (Ultrapure grade, Ventron Company). The vacuum bakeout was resumed for several additional hours at a temperature of 200°C in order to remove any free metal, free halogen, or other volatile impurities, and finally the cell was sealed off. Both iodide and bromide salts were examined in the study.

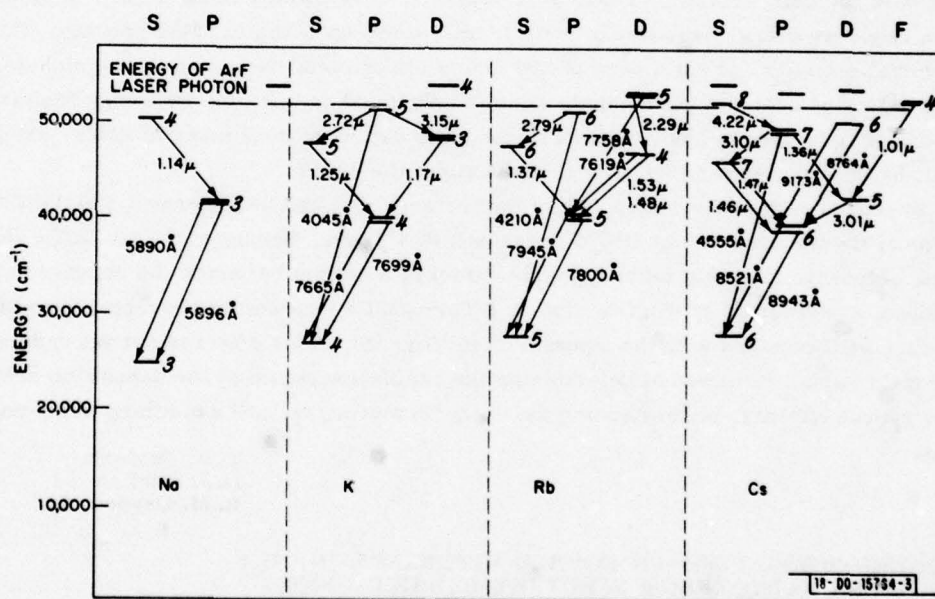


Fig. II-8. Atomic laser transitions observed with ArF dissociation of alkali-iodide salts. Script numbers to right of levels are principal quantum numbers.

Figure II-8 illustrates the laser transitions which were observed when a series of iodide salts was dissociated with 193-nm light from an ArF laser. In the figure, each alkali ground state is displaced by the dissociation energy of the molecular ground state.¹⁷ The heavy dashed line at the ArF photon energy therefore intercepts each energy-level diagram at the maximum electronic energy which may be produced by single-photon dissociation of the vibrationless

molecular ground state. Because of the large dipole moments for most of the transitions studied here, the threshold for superfluorescent stimulated emission in the cells was extremely low, and it was not necessary to use mirrors for the experiments reported here. Operating temperatures were generally between 500° and 700°C, corresponding to vapor pressures from 10^{-4} to 5×10^{-1} Torr.

D. J. Ehrlich
R. M. Osgood, Jr.

F. PHOTODEPOSITION OF METAL FILMS WITH MICROSCOPIC DIMENSIONS

The use of UV and visible lasers to initiate photodeposition and photoetching processes that may be useful in microelectronic technology is being explored. The deposition of metallic cadmium films with microscopic features has been demonstrated using a pulsed ArF excimer laser to dissociate dimethyl cadmium.

Dimethyl cadmium, $\text{Cd}(\text{CH}_3)_2$, or DMCd for brevity, exhibits a broad UV absorption band centered at 215 nm. Earlier photodissociation experiments using incoherent sources showed that absorption by this band leads to the production of cadmium atoms, with CdCH_3 also being formed. The ArF pulsed excimer laser, operating at 193 nm, provides a convenient, energetic source for the photolysis of DMCd. In a typical experiment a 10-cm stainless-steel cell was filled with 1.0 Torr DMCd, and a pinhole illuminated by the ArF laser beam was imaged on the rear window of the cell. Metallic deposits of cadmium were usually obtained in 1 to 10 pulses. Deposition requires energy densities of $\sim 0.2 \text{ J/cm}^2$, corresponding to pulse energies of less than 1 mJ. Typical deposits had diameters of 200 μm , a dimension determined by the pinhole diameter. Dektak stylus scans of the deposits showed heights of up to 1 μm , with edge features sharper than 10 μm . The deposition height was not linear with the number of shots; damage to the deposit by the beam caused cratering, and limited the height.

With improved optics, the sharpness of the features that can be generated may be limited by diffusion of the metal atoms at DMCd pressures of 1 Torr. Hence, inert gas buffers may be required to obtain the sharpest features. The effect of a helium buffer on the deposition process was examined. Addition of 27 Torr helium to 1 Torr DMCd essentially prevented deposition; deposits were still obtained with the addition of 10 Torr He. This effect is not yet understood. Current experiments are aimed at determining the resolution limits of the deposition process, improving reproducibility, understanding the deposition process, and examining other donor molecules.

T. F. Deutsch
D. J. Ehrlich
R. M. Osgood, Jr.

G. INFRARED-SUBMILLIMETER DOUBLE RESONANCE IN CH_3F USING RERADIATION FROM SCHOTTKY-BARRIER DIODES

The tunable sideband spectrometer described in previous Solid State Research Reports (see p. 15 in Ref. 1, and p. 24 in Ref. 18) has been applied to an infrared-submillimeter double-resonance investigation of the rotational spectra of vibrationally excited states of the molecule CH_3F . There have been extensive infrared-infrared double-resonance studies of molecules using tunable near-infrared lasers.¹⁹ Now, for the first time, a broadly tunable coherent submillimeter source and a fixed-frequency infrared source have been used to probe directly excited vibrational levels which were heretofore inaccessible. With this technique, not only can significant improvements in the accuracy of particular molecular constants be obtained, but also the kinetics of energy transfer can be investigated.

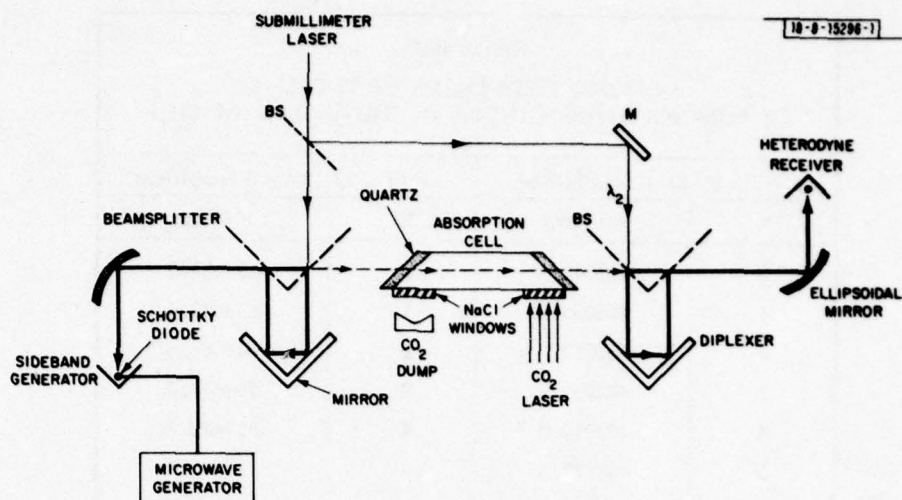


Fig. II-9. Double-resonance spectrometer.

The experimental configuration is shown schematically in Fig. II-9. Any of the numerous fixed-frequency submillimeter laser lines can be mixed with microwave or UHF signals in a corner-reflector-mounted GaAs Schottky-barrier diode²⁰ to generate tunable sidebands. The sidebands are directed through a sample cell and are detected coherently with high efficiency in a heterodyne receiver using a second corner-reflector-mounted Schottky diode. Optical diplexers in both the mixer and detector arms couple the laser radiation into the diodes with minimum loss. A CO₂ laser was used as the infrared source to excite the vibrational states.

The sample cell has quartz windows which are highly transparent to the submillimeter radiation. They are used as reflectors at 9.6 μm to enable the CO₂ beam to propagate collinearly with the submillimeter beam. An electret microphone mounted inside the cell monitors precisely the vibrational absorption of the CO₂ radiation. The double-resonance signal is observed by chopping the CO₂ beam and synchronously detecting the absorption (or emission) of submillimeter radiation.

As a demonstration of the technique, the centrifugal distortion splittings have been studied in two sets of rotational transitions in the ν_3 , $v = 1$ state of CH₃F. The 458.5- and 742.6- μm submillimeter laser lines of HCOOH were mixed with IF signals of 600 to 1100 MHz to generate approximately 10^{-7} W beams of tunable sidebands which were detected with S/N ratios of up to 40 dB. The 9.55- μm P(20) line of the 20-W CO₂ pump laser was tuned to populate the ν_3 , $v = 1$; $J = 12$; and $K = 1$ and 2 states of CH₃F, where J is the total rotational angular momentum and K is the projection of J on the C-F axis. The cell was operated at pressures of 30 to 200 mTorr, just high enough to collisionally populate the other rotational levels of the ν_3 , $v = 1$ state. The centrifugal distortion splittings ($-2K^2JD_{JK1}$) of the $J = 7 \rightarrow 8$, $\Delta K = 0$, $K = 0$ to 7 and the $J = 12 \rightarrow 13$, $\Delta K = 0$, $K = 0$ to 4 sets of rotational transitions were observed. Table II-1 lists the measured frequencies of these transitions. A value of $D_{JK1} = 0.517 \pm 0.004$ MHz was obtained, which represents a significant improvement over previous data.²¹ One check on the consistency of the data is that one can predict to within 1 MHz the frequency of the well-known $J = 12 \rightarrow 11$, $\Delta K = 0$, $K = 2$ CH₃F laser transition at $\nu = 604,297$ MHz.

TABLE II-1
MEASURED FREQUENCIES OF TWO SETS
OF ROTATIONAL TRANSITIONS IN THE ν_3 STATE OF CH_3F

J = 7 \rightarrow 8, $\Delta K = 0$ Transitions		J = 12 \rightarrow 13, $\Delta K = 0$ Transitions	
K	ν (MHz)	K	ν (MHz)
0	403043.5	0	654635.3
1	403035.3	1	654622.1
2	403010.7	2	654581.6
3	402969.2	3	654514.7
4	402910.8	4	654420.7
5	402835.6	—	—
6	402743.4	—	—
7	402632.9	—	—

This is the first demonstration of a submillimeter-infrared double-resonance technique which has general applicability to molecules which can be optically pumped. Virtually all the lower-lying rotational levels of the excited state can be probed, not just the levels which are pumped. Finally, the time response of the heterodyne receiver is fast. This enables one to directly investigate the kinetics of collision-induced population transfer among the rotational levels of the excited state. Important physical effects which may contribute include collisional selection rules arising from the C_{3v} symmetry of CH_3F and vibrational energy exchange between ground and excited-state molecules. Such kinetic studies should facilitate understanding the detailed operation of submillimeter lasers.

W. A. M. Blumberg D. D. Peck
H. R. Fetterman P. F. Goldsmith[†]

[†] University of Massachusetts, Amherst.

REFERENCES

1. Solid State Research Report, Lincoln Laboratory, M.I.T. (1978:2), p. 11, DDC AD-A061241/6.
2. Ibid. (1977:4), p. 18, DDC AD-A052463/7.
3. G. W. Iseler, H. Kildal, and N. Menyuk, *J. Electron. Mater.* 7, 737 (1978).
4. S. R. J. Brueck and H. Kildal, *Appl. Phys. Lett.* 33, 928 (1978).
5. H. Kildal and S. R. J. Brueck, *Phys. Rev. Lett.* 38, 347 (1977), DDC AD-A042238/6.
6. S. R. J. Brueck and H. Kildal, *Opt. Lett.* 2, 33 (1978), DDC AD-A054569.
7. S. R. J. Brueck, *Chem. Phys. Lett.* 53, 273 (1978), DDC AD-A057517/5.
8. H. W. Kogelnik et al., *IEEE J. Quantum Electron.* QE-8, 373 (1972).
9. W. K. Zwickler, T. Kovats, and S. R. Chinn, Fourth American Conference on Crystal Growth, Gaithersburg, Maryland, Paper IIIB, 16-20 July 1978.
10. D. J. Kuizenga and A. E. Siegman, *IEEE J. Quantum Electron.* QE-6, 694 (1970).
11. L. M. Osterink and J. D. Foster, *J. Appl. Phys.* 39, 4163 (1968).
12. The alkali-halides were first suggested as laser media in the pioneering paper of D. R. Herschbach and R. N. Zare, *Appl. Opt. Suppl. No. 2*, 194 (1965).
13. R. Burnham, *Appl. Phys. Lett.* 30, 132 (1977).
14. H. T. Powell and J. J. Ewing, *Appl. Phys. Lett.* 33, 165 (1978).
15. J. C. White, *Appl. Phys. Lett.* 33, 325 (1978).
16. D. J. Ehrlich, J. Maya, and R. M. Osgood, Jr., *Appl. Phys. Lett.* 33, 931 (1978).
17. H. G. Hanson, *J. Chem. Phys.* 27, 491 (1957).
18. Solid State Research Report, Lincoln Laboratory, M.I.T. (1978:4), DDC AD-A068563.
19. P. F. Moulton, D. M. Larsen, J. N. Walpole, and A. Mooradian, *Opt. Lett.* 1, 51 (1977), DDC AD-A046984/1.
20. H. R. Fetterman, P. E. Tannenwald, B. J. Clifton, C. D. Parker, W. D. Fitzgerald, and N. R. Erickson, *Appl. Phys. Lett.* 33, 151 (1978), DDC AD-A061203.
21. S. M. Freund, G. Duxbury, M. Römheld, J. T. Tiedje, and T. Oka, *J. Mol. Spectrosc.* 52, 38 (1974).

III. MATERIALS RESEARCH

A. LASER ANNEALING OF Se-IMPLANTED InP

In a previous report¹ we presented the results obtained in a study of the effects of laser annealing on the electrical properties of Se-implanted GaAs layers. Good electrical activation was achieved, but we observed the formation of (111) defect planes that degrade the electrical characteristics. We have now extended this study by conducting a series of laser-annealing experiments on InP, for which no such experiments have been reported in the literature. The electrical properties obtained by laser annealing of Se-implanted InP layers are comparable to those obtained by thermal annealing, and defect plane formation is much less pronounced than in the case of laser-annealed GaAs.

The InP samples were rectangular bars about 0.5×1 cm in lateral dimensions and about 800 μm thick that were cleaved from polished (111)B slices cut from semi-insulating Fe-doped single crystals. Test samples were implanted with $1 \times 10^{14} \text{ cm}^{-2}$ 400-keV Se^+ ions, while control samples were implanted with the same dose of 400-keV Kr^+ ions. Implant temperatures of 20° and 175°C were used, and during implantation the samples were tilted with respect to the ion beam in order to minimize channeling. After implantation, about half the samples were encapsulated with 3000 Å of phosphosilicate glass (PSG), which was then overcoated with 400 to 500 Å of SiO_2 .

The laser-annealing system was the same one used in the GaAs study.¹ A cylindrical lens focuses the beam from a CW Nd:YAG laser operating at 1.06 μm to form a slit-like image on the sample, which is mounted on a resistively heated platform that permits the sample to be scanned under the laser beam. The platform temperature generally used for InP was 400°C, which is high enough for sufficient bandgap narrowing to allow efficient absorption of Nd:YAG radiation, but still low enough so that there is no noticeable thermal dissociation in the absence of laser heating. During annealing, a forming gas (Ar/H_2) ambient was maintained around the sample. A single laser scan at the rate of 9.5 mm/sec was made on each sample.

Table III-1 summarizes the laser-annealing results for the Se-implanted InP test samples. Thermal etching was observed for all the unencapsulated samples, but not for any of the encapsulated ones. After annealing, the effective sheet carrier concentration N_s exceeded $2 \times 10^{13} \text{ cm}^{-2}$ for all but one of the samples listed, while the Kr-implanted control samples remained high in resistivity, with $N_s < 10^{12} \text{ cm}^{-2}$. For the three best samples, all of which were implanted at 175°C and encapsulated during annealing, N_s was between 6.8 and $8.3 \times 10^{13} \text{ cm}^{-2}$ and the effective mobility μ_s was 1300 to 1400 $\text{cm}^2/\text{V}\cdot\text{sec}$. These values are comparable to the N_s and μ_s values of $8.0 \times 10^{13} \text{ cm}^{-2}$ and 1800 $\text{cm}^2/\text{V}\cdot\text{sec}$, respectively, that are typically obtained for similarly Se-implanted InP samples that are thermally annealed at 750°C for 15 min. using PSG encapsulation.

Surface lines due to (111) defect planes were observed on only one of the laser-annealed InP samples. The great reduction in defect plane formation compared with GaAs may be due to the use of (111) InP substrates, rather than the (100) substrates used for GaAs, or to lower thermal stress in InP. Lower thermal stress is expected because InP has a lower thermal expansion coefficient and higher thermal conductivity than GaAs, and lower annealing temperatures are required for good activation. On the (111) InP surface, the lines due to the defect planes

TABLE III-1 LASER ANNEALING OF InP SAMPLES IMPLANTED WITH $1 \times 10^{14} \text{ cm}^{-2} \text{ Se}^+$ Ions					
Implant Temperature (°C)	Encapsulation	Power Density (W/cm ²)	Effective Sheet Electron Concentration N_s (cm ⁻²)	Effective Mobility μ_s (cm ² /V-sec)	Surface Features
175	No	9.5×10^3	2.0×10^{13}	400	Slight thermal etch
175	No	9.9×10^3	3.5×10^{13}	630	Thermal etch
175	No	1.03×10^4	3.3×10^{13}	550	Thermal etch
175	PSG + SiO ₂	9.9×10^3	6.8×10^{13}	1300	Smooth
175	PSG + SiO ₂	1.01×10^4	8.0×10^{13}	1400	Slight marks
175	PSG + SiO ₂	1.03×10^4	8.3×10^{13}	1300	Smooth
20	PSG + SiO ₂	1.03×10^4	1.2×10^{13}	450	Smooth
20	PSG + SiO ₂	1.08×10^4	1.1×10^{13}	540	Smooth
20	No	1.01×10^4	4.7×10^{11}	260	Thermal etch
20	No	1.08×10^4	2.0×10^{13}	260	Thermal etch

intersect with each other at an angle of 60° . The one InP sample for which defect lines were observed was the sample with the highest μ_s . Thus, the defects apparently have less effect on the electrical properties of InP than they do in the case of GaAs. The reduction in degradation due to defects may result because defects in InP are generally n-type and therefore do not tend to compensate n-type material.

J. C. C. Fan C. O. Bozler
J. P. Donnelly R. L. Chapman

B. ION-IMPLANTED, LASER-ANNEALED GaAs SOLAR CELLS

Although laser treatment of semiconductor materials is the subject of strong current interest, little has been reported to date on device fabrication utilizing the laser annealing of ion-implanted layers, except for the preparation of single-crystal Si solar cells with an efficiency of about 11 percent at AM1 (see Ref. 2). We have now fabricated ion-implanted, laser-annealed (IILA) GaAs solar cells with conversion efficiencies up to 12 percent at AM1.

We previously developed GaAs shallow-homojunction solar cells, with conversion efficiencies as high as 20 percent at AM1, that incorporate GaAs layers grown by chemical vapor deposition (CVD) on either GaAs (Ref. 3) or Ge (Ref. 4) single-crystal substrates. These devices employ an $n^+/p/p^+$ structure, without a GaAlAs window, in which surface recombination losses are reduced because the n^+ -layer is so thin that most of the photogenerated carriers are created in the p-layer below the junction. The new IILA cells use a similar shallow-homojunction $n^+/p/p^+$ structure, but the n^+ -layer is formed by implantation of Se ions into a p/p^+ -wafer.

A number of advantages can be expected for IILA solar cells. Ion implantation is well suited to the preparation of efficient shallow-homojunction cells, since the range of the ions is of the same order as the required junction depth. In addition, the as-implanted depth profile of the dopant can be accurately controlled and reproduced from run-to-run by fixing the ion energy and dose. Furthermore, the lateral uniformity of the dopant profile is not very sensitive to surface morphology, a feature that may be important for polycrystalline solar cells, where surface roughness is often encountered.

The damage incurred during ion implantation generally renders the dopant electrically inactive, and annealing is necessary for electrical activation. For GaAs, conventional thermal annealing is accomplished by heating the implanted sample to about 900°C for 5 to 15 min., but this requires the GaAs surface to be encapsulated in order to prevent As loss. With laser heating, annealing may be achieved in a much shorter time, and without the necessity of encapsulation. Laser annealing also has the advantage of minimizing the diffusion of the dopant.

In a recent study¹ we achieved good electrical activation of Se-implanted GaAs by annealing with scanned radiation from a CW Nd:YAG laser. On the basis of this study, we selected a set of ion-implantation and laser-annealing parameters for fabricating IILA solar cells with an $n^+/p/p^+$ shallow-homojunction structure. An AsCl_3 -Ga- H_2 CVD system described previously⁴ was used to grow a p-epilayer about $3\text{ }\mu\text{m}$ thick on a single-crystal p^+ substrate oriented 2° off (100), toward (110). The epilayer and substrate were doped with Zn to concentrations of about 1×10^{17} and $1 \times 10^{18}\text{ cm}^{-3}$, respectively. The n^+ -layer was formed by implanting $2 \times 10^{14}\text{ cm}^{-2}$ 400-keV Se ions in the p/p^+ -wafer at an implant temperature of 300°C . During implantation, the wafer was tilted with respect to the ion beam in order to minimize channeling.

The system used for laser annealing the implanted samples has been described previously.¹ The circular beam from a CW Nd:YAG laser operating at $1.06\text{ }\mu\text{m}$ is focused by a cylindrical lens

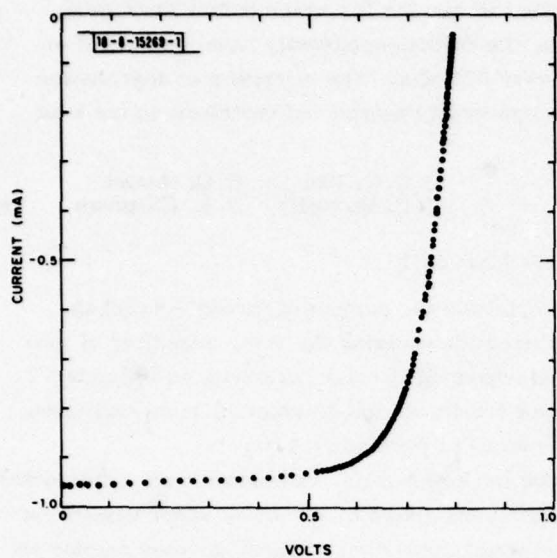


Fig. III-1. Photocurrent as a function of voltage for an ion-implanted, laser-annealed (IILA) GaAs cell with 12-percent conversion efficiency at AM1.

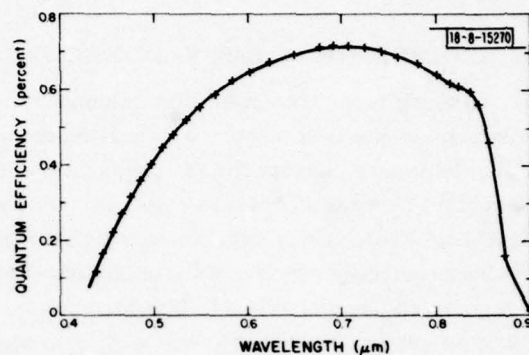


Fig. III-2. Quantum efficiency as a function of wavelength for cell of Fig. III-1.

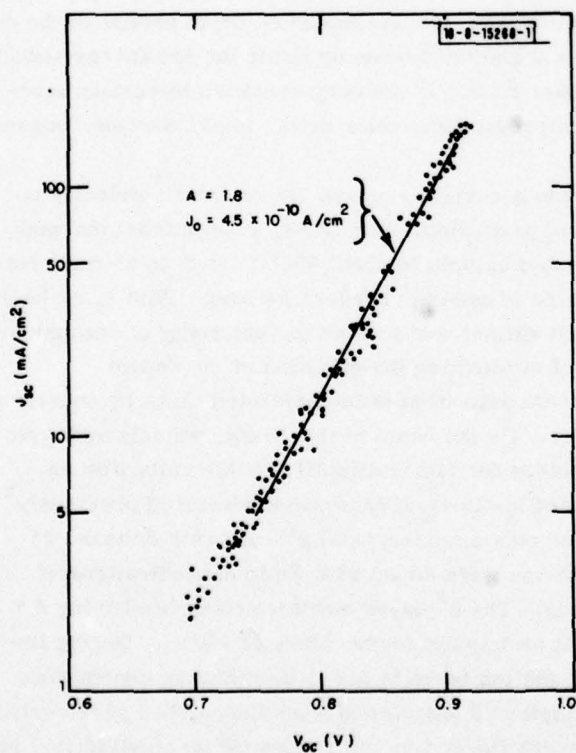


Fig. III-3. Short-current density J_{sc} as a function of open-circuit voltage V_{oc} at different illumination levels for cell of Fig. III-1.

into a slit-like image onto the GaAs sample. By mapping the image with a moving Si photodiode whose active area was covered by a mask with a 3- μm -diam hole, the power density was found to be uniform to about ± 3 percent over a central area of 50 μm by 1.5 mm. The uncertainty in absolute-power-density measurements is estimated to be about ± 10 percent. During laser annealing, the sample is held in a forming gas (Ar/H_2) ambient on a resistively heated platform. The platform is mounted on a translational stage that permits the sample to be scanned under the laser beam in the focal plane and normal to the long axis of the slit image.

Laser-annealing runs were made on two unencapsulated samples from the same ion-implanted GaAs wafer. In each run the sample platform was heated to 580°C, the incident power density within the central area of the image was about 3 kW cm^{-2} , and the sample scan rate was about 0.5 mm sec^{-1} . This rate was selected in order to reduce the formation of (111) slip planes. Our earlier study showed an increase in the density of slip planes with increasing scan rate, and a resultant degradation in the electrical properties of IILA layers. No such planes were observed on either of the two annealed samples, although some regions of the surface were somewhat roughened or gave evidence of slight thermal etching. Since the earlier study showed that electrical activation was increased by repeated laser scans, during each annealing run the sample was scanned back and forth under the laser image a total of ten times—five times in each direction. In the first run, the sample was not moved laterally between scans, and three cells were made from the section of the sample that had been exposed to ten scans by the central area of the image. In the second run, the sample was translated laterally by 0.23 mm after each scan, and a cell about 2.2 mm square was made from the annealed region.

The fabrication techniques used for the IILA cells were similar to those used for our all-CVD cells, as described previously.^{3,4} No vacuum processing procedures were employed. The back contact to the p^+ substrate was electroplated Au, and the front contact bar and fingers (defined by photolithography) were electroplated Sn-Ag. By a series of alternating anodic oxidation and etching steps, the thickness of the n^+ -layer was reduced by about 2100 Å from its initial value of about 3000 Å. The last of these steps was an anodization that formed an oxide layer about 850 Å thick as an antireflection coating. The cell area was defined by conventional mesa techniques. The areas of the four cells ranged from 0.28 to 4.7 mm^2 .

In making conversion-efficiency measurements, a high-pressure Xe lamp with a water filter was used as a simulated AM1 source. Using a NASA-measured GaAs solar cell as a reference, the source was adjusted to provide an incident radiation of 100 mW/cm^2 . The measurements were made at an ambient temperature of 25°C. Figure III-1 shows the current-voltage curve for the most efficient cell, which also had the largest area. The open-circuit voltage (V_{oc}) was 0.79 V, the short-circuit current density (J_{sc}) was 20.4 mA/cm^2 (not corrected for the contact finger area, which was less than 5 percent of the total), and the fill factor was 0.73, giving a measured efficiency of about 12 percent. The other cells had efficiencies of 9, 10, and 11 percent.

The quantum efficiency of the best cell is plotted as a function of wavelength in Fig. III-2. The values of quantum efficiency are about 20-percent lower than those of our best all-CVD cells. This decrease corresponds well with the lower J_{sc} measured in our IILA cells. Figure III-3 shows the dependence of J_{sc} (in this case, corrected for contact finger area) on V_{oc} as obtained by a series of measurements on the best cell at different illumination levels up to about 10 suns. The whole series was taken in about 10 sec to minimize heating at the high illuminations, with the cell mounted on a copper block thermoelectrically controlled at 25°C. From the relationship⁵

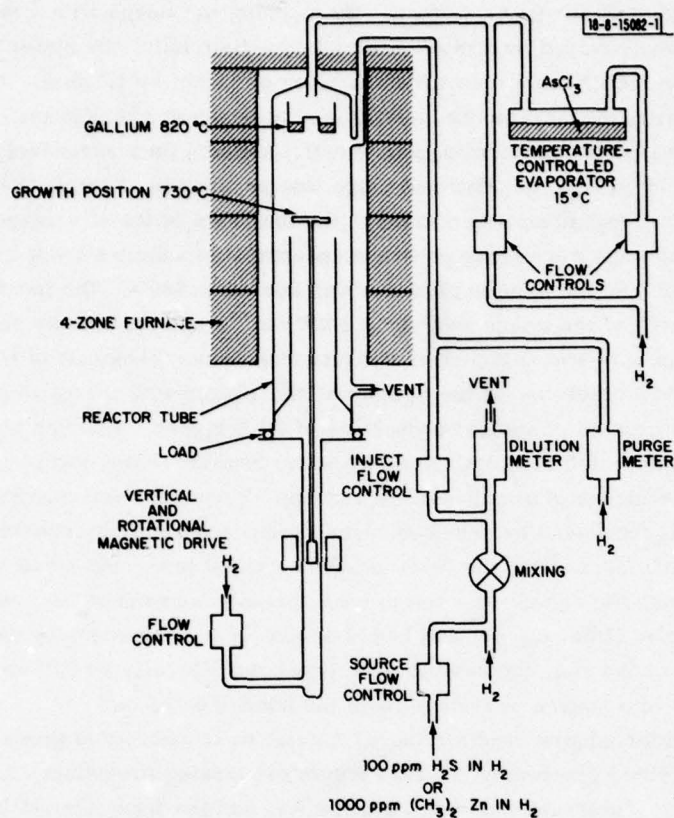


Fig. III-4. Schematic of GaAs vapor-deposition system showing H_2 , $AsCl_3$, and doping-gas-flow control, and also a cross-sectional view of reactor tube.

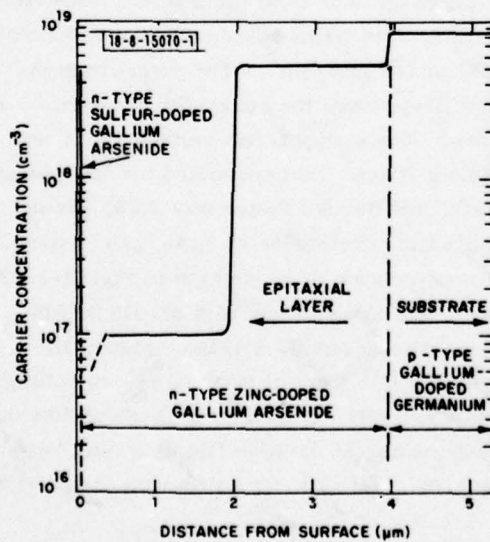


Fig. III-5. Impurity profile of GaAs epitaxial layers grown on a single-crystal Ge substrate for $n^+/p/p^+$ shallow-homojunction solar cells.

$V_{oc} = A(kT/q) \ln [(J_{sc}/J_0) + 1]$, where k is Boltzmann's constant, T is the absolute temperature, and q is the electronic charge, the diode factor A is about 1.8 and the saturation current density J_0 is about 4.5×10^{-10} A/cm². Both values are higher than those for our best all-CVD cells, resulting in the lower V_{oc} and fill factor of the IILA cells.

Since the IILA GaAs solar cells are at an early stage of development, optimizing the implantation and annealing parameters should lead to a significant improvement in their performance. At this time we see no obstacles that would prevent their ultimate efficiency from approximating the values that we have achieved for all-CVD homojunction GaAs cells.

J. C. C. Fan G. W. Turner
R. L. Chapman C. O. Bozler
J. P. Donnelly

C. EFFICIENT GaAs HOMOJUNCTION SOLAR CELLS ON Ge SUBSTRATES

We previously reported^{6,7} the development of GaAs solar cells, fabricated without the use of Ga_{1-x}Al_xAs layers, with conversion efficiencies as high as 20 percent at AM1. These cells employ an n⁺/p/p⁺ structure, prepared by chemical vapor deposition (CVD) on single-crystal GaAs substrates, in which surface recombination losses are reduced because the n⁺-layer is so thin that most of the carriers are generated in the p-layer below the junction. We have now obtained 20-percent efficiency at AM1 with similar GaAs cells on single-crystal Ge substrates. The spectral response and efficiency of these cells show steady improvement as the n⁺-layer is thinned to 200 Å by means of a controlled anodization-stripping technique.

The GaAs layers are grown on the Ge substrates in the AsCl₃-Ga-H₂ system shown schematically in Fig. III-4. The reactor tube has an inner diameter of 55 mm, and the H₂-flow through the AsCl₃ evaporator and over the Ga boat is in the range 300 to 500 cm³/min. The p and n dopants are introduced in the vapor phase by using (CH₃)₂Zn and H₂S, respectively. The reactor tube is vertical, allowing rotation of the substrate, which results in greater doping uniformity in the layers. The substrate can be preheated in pure H₂ just before being introduced into the reactant gas flow at the growth position.

The Ge substrates are oriented 2° off (100), toward (110). The substrates are prepared by coating the back side with SiO₂ to reduce Ge autodoping of the GaAs layers during growth, and the electron concentration in nominally undoped layers deposited on these coated substrates was 5×10^{15} cm⁻³. The lattice constants and expansion coefficients of Ge and GaAs are well matched, and thus a favorable condition exists for obtaining good-quality epitaxial layers.

The doping profile used for the solar cells is shown in Fig. III-5. The p⁺ Ge substrate is highly doped with Ga (8×10^{18} cm⁻³) in order to overdope any As that may diffuse into the Ge during the deposition of the GaAs, and to assure tunneling through any thin barriers which may arise at the heterojunction interface. The p⁺ GaAs buffer layer is highly doped with Zn, again to assure tunneling and also to overdope Ge diffusing into the GaAs during growth. The change in hole concentration from 5×10^{18} cm⁻³ in the buffer layer to 1×10^{17} cm⁻³ in the active layer provides a back-surface field to increase the collection efficiency. In order to maximize the open-circuit voltage (V_{oc}) of the cells, the carrier concentration in the active layer should be high, but increasing the concentration reduces the electron diffusion length.⁸ The preliminary results of our computer simulations of the n⁺/p/p⁺ structure show that the optimum concentration in the active region is in the low 10^{17} cm⁻³ range. Because the diffusion lengths in GaAs are larger for electrons than for holes, this structure should have better collection efficiency than

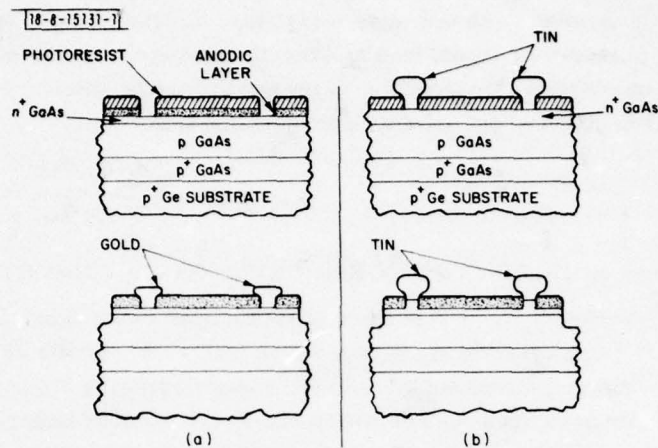


Fig. III-6. Schematic of fabrication process for solar cells using (a) gold or (b) tin contact metallization.

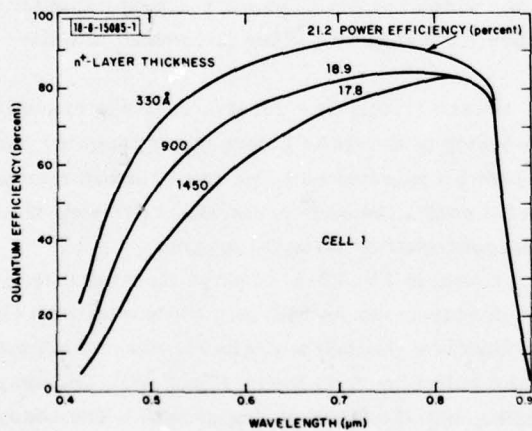


Fig. III-7. Spectral response of a solar cell with an n^+ -layer which was thinned using an anodize-strip cycle.

the complementary $p^+/n/n^+$ structure. The doping concentration shown in Fig. III-5 for the n^+ -layer, $5 \times 10^{18} \text{ cm}^{-3}$, is the highest obtainable with our CVD system. The n^+ -layers were characterized by Hall and resistivity measurements on test specimens taken from each wafer. For the cells reported here, the sheet resistivity is in the range 45 to 100 Ω/\square , and the electron mobility is $\sim 1000 \text{ cm}^2/\text{V-sec}$.

An AR coating is produced on the n^+ -layer by anodic oxidation, which consumes a thickness of GaAs equal to 0.66 times the thickness of oxide produced. The anodizing solution is prepared by adding 3-g tartaric acid to 100-ml H_2O , adjusting the pH to 6.2 with NH_4OH , and adding 250-ml propylene glycol (see Ref. 9). The thickness of the oxide layer is proportional to the limiting voltage used for anodization. The thickness required for an optimum AR coating is 860 Å, which is obtained for a limiting voltage of 43 V (see Ref. 7).

Contact to the very thin n^+ -layer is made easily because of its high doping level. Electroplated Au forms ohmic contacts with a specific resistance of $8 \times 10^{-5} \Omega\text{-cm}^2$. Electroplated Sn also appears to form ohmic contacts, although their resistance has not been measured. Sn has the advantage that in the solution used for GaAs anodization, Sn is also anodized forming an oxide resistive enough to allow the GaAs to be anodized in the presence of Sn contacts.

Two different fabrication procedures are used for cells with Au and Sn contact fingers, as shown schematically in Fig. III-6(a-b). For devices with Au contacts the n^+ -layer is anodized, finger openings are then etched through the oxide using a photoresist mask, and, finally, Au is plated using the same mask. For cells with Sn contacts the Sn fingers are plated using a photoresist mask, the photoresist is then removed, and, finally, the n^+ -layer is anodized. With this procedure the n^+ -layer is thicker under the Sn contacts than under the anodic oxide, so that there is a larger separation of the metal from the p-n junction than with Au contacts. Because the n^+ -layer is so thin, the increased separation may be better for device yield and reliability.

The use of Sn contacts is advantageous for optimizing the n^+ -layer thickness, since the anodic oxide formed on GaAs can be stripped with dilute HCl and the cell reanodized without removing the contacts. Because the thickness of the oxide layer is very uniform and easily controlled by adjusting the anodizing voltage, a series of alternating anodization and stripping steps can therefore be used for controlled reduction of n^+ -layer thickness. The thickness of GaAs removed during each anodization can be accurately determined by using ellipsometry to measure the anodic oxide thickness and multiplying this value by the thickness ratio 0.66.

A mesa etch of the GaAs is used to define the active area of the cell, and the back contact to the Ge substrate is made by Au plating. No alloying or vacuum processing is used in cell fabrication.

Measurements of spectral response as a function of n^+ -layer thickness were made on small cells, 0.05 cm^2 in area, having two Sn contact fingers 0.5 mm apart connected to a Sn bar at one end. The n^+ -layer, which was initially 2000 Å thick with a sheet resistance of 45 Ω/\square , was thinned by alternate anodization and stripping. The external quantum efficiency, which is the ratio of the number of carriers collected (I_{sc}/q) to the number of incident photons, was measured after each of three anodizations at 43 V so that the cells were antireflection-coated during each measurement. The values of I_{sc} and incident photon flux were measured as a function of wavelength in a spectrometer which was arranged so that all the light fell between the two contact fingers. The results for cell 1 are given in Fig. III-7, which shows that thinning the n^+ -layer results in a marked improvement in quantum efficiency, especially at shorter wavelengths. This is expected because of the high absorption coefficient for GaAs (10^4 to 10^5 cm^{-1})

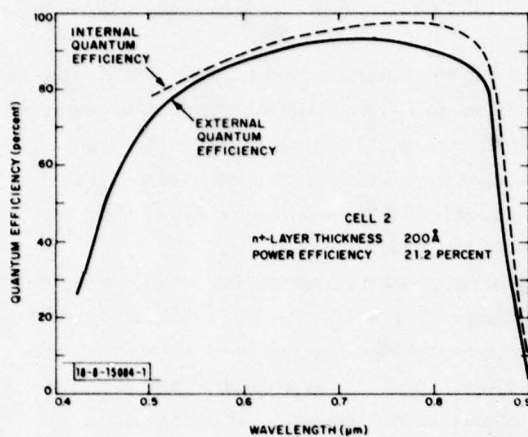


Fig. III-8. Spectral response of a solar cell comparing internal and external quantum efficiency.

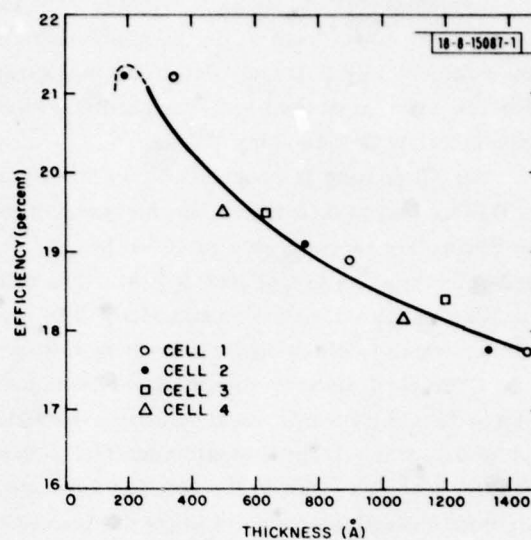


Fig. III-9. Power conversion efficiency as a function of n^+ -layer thickness of four cells fabricated side-by-side on same wafer where n^+ -layer was thinned using an anodize-strip cycle.

TABLE III-2								
EXPERIMENTAL MEASUREMENTS OF GALLIUM ARSENIDE SHALLOW HOMOJUNCTION SOLAR CELLS HAVING AN AREA OF 0.49 cm^2								
Cell No.	CVD Wafer No.	Contact Metal	Initial Sheet Resistance (Ω/\square)	Total Anodization Voltage	AM1 V_{oc} (V)	AM1 I_{sc} (mA)	AM1 Fill Factor	AM1 Efficiency (percent)
1	13	Au	102	63	0.99	12.0	0.82	20
2	11	Au	65	96	0.99	11.4	0.83	19
3	9	Sn	62	86	0.97	10.9	0.79	17
4	11	Sn	65	106	0.99	11.8	0.75	18
5	11	Sn	65	116	0.99	11.9	0.79	18

which increases with decreasing wavelength,¹⁰ and the high surface recombination velocity, which is believed to be around 10^6 cm/sec. The power conversion efficiency for each n^+ -layer thickness is also given in Fig. III-7. These values were measured with the cell fully illuminated by a simulated AM1 source, with no correction made for the finger area.

Figure III-8 shows the final spectral response of cell 2, which was fabricated next to cell 1. The n^+ -layer was slightly thinner than that of cell 1, and the response was therefore slightly improved at the short wavelengths. The curve for internal quantum efficiency, which is the ratio of I_{sc}/q to the rate at which photons enter the semiconductor, was obtained from the measured external efficiency by correcting for the spectral reflectivity of the AR-coated cell. This curve indicates that the cell design is very near the optimum.

The AM1 power efficiencies of cells 1 and 2 and two other small cells fabricated side-by-side on the same wafer are plotted in Fig. III-9 as a function of n^+ -layer thickness. In order to obtain additional thickness values, cells 2, 3, and 4 were first anodized to 10, 20, and 30 V, respectively, after which the oxide was stripped. All four cells were then anodized together to 43 V to provide an AR coating, stripped, anodized to 43 V, stripped again, and once more anodized to 43 V. Efficiency measurements were made after each 43-V anodization. After the third such anodization, the efficiency of cell 3 had dropped to 10 percent, while cell 4 had no sensitivity to light.

Assuming that the cell output drops to zero when removal of the n^+ -layer is completed, the complete removal would occur at a total anodization voltage between 149 and 159 V for cells 1 to 4 – the final values for cells 3 and 4, respectively. For the purposes of plotting the data, it was assumed that complete removal would occur at 154 V. Using the removal rate of $13.3 \text{ \AA}/V$, the initial n^+ -layer thickness was found to be 2050 \AA . To obtain the thickness of the n^+ -layer remaining after each successive anodization, the total thickness removed was calculated from the sum of the voltages used to that point and subtracted from the initial thickness. The thickness values given in Figs. III-7 and III-8, as well as those of Fig. III-9, were obtained in this manner. For all the points in Fig. III-9, the fill factor was 0.82 and V_{oc} was 0.97 V. As the thickness of the n^+ -layer is reduced, the power conversion efficiency rises with increasing slope until the n^+ -layer is less than 200 \AA thick, where the efficiency drops precipitously from the maximum value of 21.2 percent.

Seven larger cells, $1 \times 0.49 \text{ cm}$, were made from three different wafers. Either Au or Sn was used for the contact finger pattern, which consisted of 20 fingers 0.5 mm apart with a connecting bar at one end. The fingers covered 4 percent of the total area. One cell with Au contacts was partially shorted, and one with Sn contacts was thinned too much. Power efficiency measurements, using a high-pressure Xe lamp with a water filter as a simulated AM1 source, were made on the other five cells. The incident intensity was adjusted to 100 mW/cm^2 using a NASA-calibrated GaAs solar cell as a reference. Table III-2 lists the measured values of V_{oc} , I_{sc} , fill factor, and efficiency, as well as the initial sheet resistance and the total anodization voltage. Independent measurements at NASA Lewis Research Center have confirmed these results. The sheet-resistance value gives some indication of the initial thickness of the n^+ -layer; a value of $100 \text{ } \Omega/\square$ corresponds to approximately 1200 \AA . The total anodization voltage is the sum of the limiting voltages used in a series of anodization-strip steps where the thinning ratio is $20 \text{ \AA}/V$. For each cell, the final anodization was carried out at 43 V to provide the AR coating. The cells with Sn contacts have slightly lower fill factors, indicating some extra series resistance associated with the Sn. The efficiency values, which were not corrected for contact areas, are all in the 17- to 20-percent range.

In conclusion, epitaxial layers of GaAs have been grown by CVD on single-crystal Ge substrates, and high-efficiency shallow-homojunction solar cells have been fabricated from these layers. A new Sn plating and anodization-stripping technique has been used to determine the effect of n^+ -layer thickness on the performance of solar cells with the $n^+/p/p^+$ structure. The use of Ge substrates should reduce the cost of single-crystal GaAs solar cells.

C. O. Bozler
J. C. C. Fan
R. W. McClelland

D. LASER-EMISSION STUDY OF THE PRESSURE DEPENDENCE OF THE ENERGY GAP IN TELLURIUM

As part of a program to develop broadly tunable infrared-laser sources, we measured the pressure dependence of the laser emission of optically pumped Te at liquid-nitrogen temperatures for hydrostatic pressures up to 8 kbar. The laser emission, which is associated with the direct H-point energy gap in Te, tunes from 3.7 to 6.0 μm over this pressure range. This very large pressure dependence makes Te an attractive candidate material for tunable lasers in the mid-infrared. To our knowledge this is the first report of optically pumped laser action in Te, though electron-beam excitation has previously been described.¹¹ Since Te has not been made n-type, diode lasers have not been fabricated.

In contrast to the extremely linear pressure tuning of a number of zinc-blende semiconductor lasers previously studied,¹² Te exhibits a marked nonlinear pressure dependence. This nonlinearity has been noted before in analyses of the optical absorption and photoconductivity¹³ and electrical transport measurements¹⁴⁻¹⁶ of the energy gap in Te. The present high-resolution laser-emission measurement, which is a more precise and direct probe of the energy gap than these other techniques, gives a linear pressure coefficient of -20.0 ± 0.5 meV/kbar (compared with values from -13 to -23.4 meV/kbar reported previously¹³⁻¹⁹) and yields a significantly higher nonlinearity.

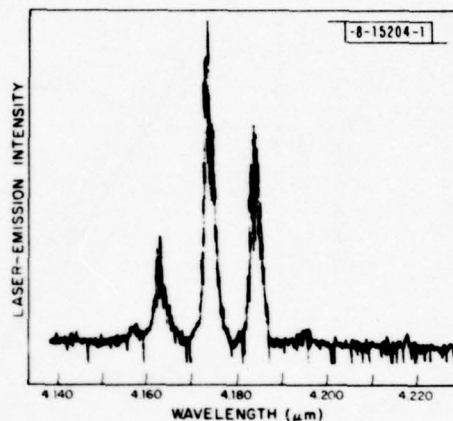
The nonlinear pressure dependence of the energy gap in Te has been attributed by Anzin *et al.*¹³ to the nonlinear compressibility of the crystal assuming a constant deformation potential. This assertion was based on early x-ray measurements of the nonlinear pressure dependence of the lattice constants of Te (see Refs. 20 and 21). However, more recent x-ray data to higher pressures²² indicate too small a nonlinearity to account for the energy-gap variation. This implies that the deformation potential is not constant over the measured pressure range. The present results will be compared with previous measurements of the linear and nonlinear pressure dependence of the bandgap.

The apparatus used to measure the pressure dependence of the laser emission of Te was essentially the same as that used for pressure-tuning of optically pumped GaSb, InAs, and InSb semiconductor lasers.¹² A Q-switched Nd:YAG laser was chosen as a convenient universal excitation source for pumping these bulk semiconductor materials well above their bandgaps.

The Te sample was obtained from Kennecott Copper Corporation. Hall measurements at 77 K showed the hole concentration to be $p = 3.4 \times 10^{14} \text{ cm}^{-3}$. Platelets oriented normal to the crystal c-axis were cut with a string saw and then polished in a $\text{Br}:\text{CH}_3\text{OH}$ etch to a thickness of $\sim 50 \mu\text{m}$. Laser cavities were formed by cleaving edges normal to the crystal y-axis about 200 μm apart. The cleaving was done at liquid-nitrogen temperature, since at room temperature the soft material tended to bend, crush, and tear. A transverse pumping geometry¹² was used

in which the 1.06- μm Nd:YAG laser radiation was focused by a 10-cm cylindrical lens onto the polished c-face of the platelet along a line bridging the parallel cleaved edges. The four-port high-pressure vessel¹² contained a 6-mm-thick by 6-mm-diam sapphire window to admit the pump light and a 6- \times 6-mm Irtran 5 (sintered polycrystalline MgO) window to transmit the Te laser radiation out to 6.0 μm . The MgO windows exhibited slight extrusion and clouding after several cycles to 8 kbar at 77 K. No permanent damage nor hysteresis effects was noted for the Te sample, which was in a hydrostatic environment provided by a helium-gas pressure medium. The helium gas is also transparent to the infrared radiation. Pressure was measured with a temperature-compensated manganin strain gauge, dead-weight calibrated by the manufacturer (Harwood Engineering) to within 1 percent.

Fig. III-10. Mode structure of laser emission of optically pumped Te at $P = 2$ kbar and $T = 77$ K.



A spectrum of the optically pumped Te laser emission at a pressure of 2 kbar is shown in Fig. III-10. The separation between the peaks corresponds roughly to the longitudinal mode spacing, $0.5 n^* L$, expected for a cavity ~ 200 μm long with an effective refractive index $n^* = [n - \lambda(\partial n / \partial \lambda)] \sim 5$ (Ref. 23) for the $E \perp c$ polarized output. The width of each of the peaks is resolution limited for the 1-cm^{-1} slit setting on the Spex grating monochromator. However, with narrower slits a residual mode width of $\sim 0.6\text{ cm}^{-1}$ was observed, indicating some chirping of the laser frequency due to heating during the 200-nsec-long pump pulse. For the spectrum of Fig. III-10, the incident peak power from the pump laser was 250 W, which was $\sim 3\times$ threshold, and the pump photon energy was about $4\times$ the bandgap energy, so considerable excess energy was deposited in the lattice. The threshold pump power was between 60 and 80 W over the full 8-kbar pressure range for temperatures from 63 to 77 K.

The tuning of the laser-emission energy vs hydrostatic pressure P in kilobars at 63 and 77 K is shown in Fig. III-11. Here the centroid of the laser mode pattern is plotted; the individual modes tune at approximately $0.3\times$ the rate of the envelope, due primarily to the pressure variation of the refractive index.¹² There seems to be little systematic temperature dependence of the bandgap in the 63- to 77-K range according to the data in Fig. III-11. The 63-K data, which had less scatter, were fit with a quadratic expression:

$$E_g(P) = E_g(0) + AP + BP^2 \quad (\text{III-1})$$

where $E_g(0) = 333.5 \pm 0.5$ meV, $A = -20.0 \pm 0.5$ meV/kbar, and $B = 0.52 \pm 0.02$ meV/kbar². This parabola is superimposed on the data in Fig. III-11 and a straight line is drawn between the

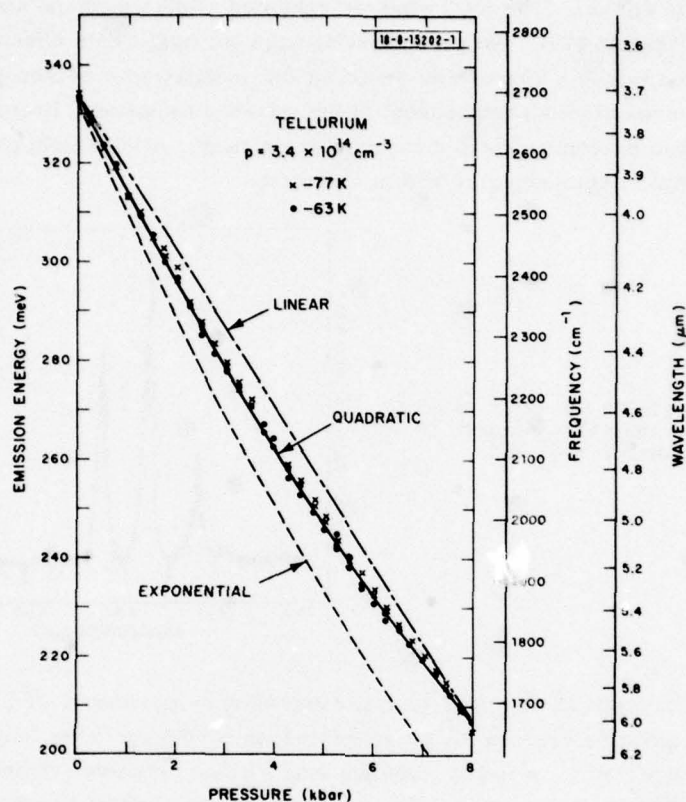


Fig. III-11. Pressure tuning of laser emission of optically pumped Te. Linear curve is $E_g(P) = 333.5 - 15.8 P$; quadratic curve is $E_g(P) = 333.5 - 20.0 P + 0.52 P^2$; exponential curve (Ref. 13) is $E_g(P) = 331.6 \times \exp[-0.0706 P]$, where $E_g(P)$ is in meV and P is in kbar.

first and last points in order to indicate the deviation of the tuning from linearity. Also included is the exponential curve given by Anzin *et al.*¹³ as a fit to their photoconductivity data at 77 K; here, $E_g(P) = E_g(0) \exp[-\alpha P]$ with $E_g(0) = 331.6 \pm 0.6$ meV, and $\alpha = 0.0706 \pm 0.0005$ kbar⁻¹. The higher energies found by laser emission are more indicative of the bandgap than photoconductivity or absorption-edge data, which are less sharp and are subject to extrapolation errors due to bandtailing effects. Also, the slightly larger pressure dependence of the bandgap obtained by Anzin *et al.*¹³ may result from a possible nonhydrostatic environment caused by using benzene as a pressure fluid at low temperatures and the very anisotropic compressibility of Te (see Refs. 20 through 22).

The initial slope of the pressure dependence of the energy gap obtained by conductivity and Hall-effect measurements has been given as $(\partial E_g / \partial P)_{P=0} = -17$ meV/kbar by Blum and Deaton,¹⁵ -14.7 meV/kbar by Koma *et al.*,¹⁶ and -13 meV/kbar by Becker *et al.*¹⁷ These electrical measurements were all made in the intrinsic carrier regime of Te at room temperature and above, and they depend to some extent on the number of extrinsic carriers and on assumptions about the pressure dependences of the valence- and conduction-band densities of states. The slopes from these transport studies are consistently lower than for the optical measurements made here and elsewhere.^{13,18,19}

A. S. Pine
N. Menyuk

REFERENCES

1. Solid State Research Report, Lincoln Laboratory, M.I.T. (1978:4), DDC AD-A068563.
2. J. Narayan, R. T. Young, R. F. Wood, and W. H. Christie, Appl. Phys. Lett. 33, 338 (1978).
3. J. C. C. Fan, C. O. Bozler, and R. L. Chapman, Appl. Phys. Lett. 32, 390 (1978), DDC AD-A058281/7.
4. C. O. Bozler, J. C. C. Fan, and R. W. McClelland, in Proceedings of the 7th International Symposium on GaAs and Related Compounds, St. Louis, 1978 (The Institute of Physics, London, 1979), p. 429.
5. M. P. Godleski, C. R. Baraona, and H. W. Brandhorst, Jr., Conf. Record 10th IEEE Photovoltaic Specialists Conf., Palo Alto, California, 13-15 November 1973, p. 40.
6. C. O. Bozler and J. C. C. Fan, Appl. Phys. Lett. 31, 629 (1977), DDC AD-A053926/2.
7. J. C. C. Fan, C. O. Bozler, and R. L. Chapman, Appl. Phys. Lett. 32, 390 (1978), DDC AD-A058281/7.
8. L. W. Ackerman, M. F. Miller, and M. J. McColl, Appl. Phys. Lett. 38, 685 (1967).
9. H. Hasegawa and H. L. J. Hartnagel, Electrochem. Soc. 124, 1784 (1977).
10. B. O. Seraphin and H. E. Bennett, Optical Properties of III-V Compounds, Vol. 3 of Semiconductors and Semimetals (Academic Press, New York, 1967).
11. C. Benoit a la Guillaume and J. M. Debever, Physics of Quantum Electronics, edited by P. L. Kelley, B. Lax, and P. E. Tannenwald (McGraw-Hill, New York, 1966), p. 397.
12. N. Menyuk, A. S. Pine, J. A. Kafalas, and A. J. Strauss, J. Appl. Phys. 45, 3477 (1974), DDC AD-A002777/1.
13. V. B. Anzin, M. I. Eremets, Yu. V. Kosichkin, A. I. Nadezhdinskii, and A. M. Shirokov, Phys. Stat. Sol. (a) 42, 385 (1977).
14. J. Bardeen, Phys. Rev. 75, 1777 (1949).
15. F. A. Blum and B. C. Deaton, Phys. Rev. 137, A1410 (1965).
16. A. Koma, T. Tani, and S. Tanaka, Phys. Stat. Sol. (b) 66, 669 (1974).
17. W. Becker, W. Fuhs, and J. Stuke, Phys. Stat. Sol. (b) 44, 147 (1971).
18. V. B. Anzin, Yu. V. Kosichkin, A. I. Nadezhdinskii, and A. M. Shirokov, Phys. Stat. Sol. (a) 20, 253 (1973).
19. L. J. Neuringer, Phys. Rev. 113, 1495 (1959).
20. P. W. Bridgman, Proc. Amer. Acad. Arts and Sci. 60, 305 (1925).
21. F. Birch, J. F. Schaiver, and H. C. Spiecer, Geol. Soc. Amer. Spec. Papers No. 36 (1942).
22. J. C. Jamieson and D. B. McWhan, J. Chem. Phys. 43, 1149 (1965).
23. American Institute of Physics Handbook, 2nd Edition (McGraw-Hill, New York, 1963), p. 6-40.

IV. MICROELECTRONICS

A. CHARGE-COUPLED DEVICES: SAW/CCD ACCUMULATING CORRELATOR

Experiments with the SAW/CCD buffer memory¹ have led to the development of an accumulating correlator which is capable of correlating two long-duration analog signals of up to 20-MHz bandwidth. This new device is a practical realization of the SAW tapped correlator described by Menager and Desormiere.² Construction techniques for SAW/CCD devices appear in an earlier report.³ A schematic diagram of the accumulating correlator (Fig. IV-1) shows a LiNbO₃ delay line in close proximity (typically 300 nm) to an array of 300 sampling fingers connected to a 300-stage CCD on a p-type silicon substrate. The RF piezoelectric fields associated with the SAWs are sensed by the sampling fingers and used to modulate charge in the CCD structure.

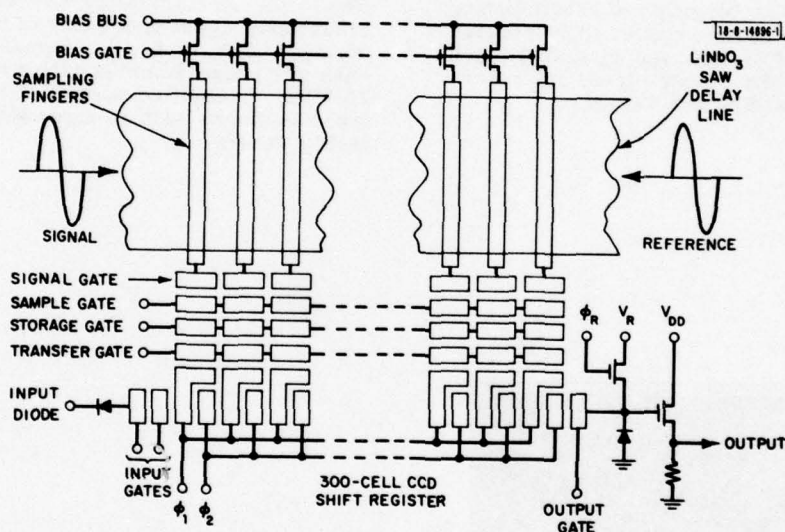


Fig. IV-4. Schematic diagram of a SAW/CCD accumulating correlator.

In the accumulating correlator, two counterpropagating surface waves - a signal and a reference - are launched from opposite ends of the LiNbO_3 SAW delay line. These two waveforms are sensed by the sampling fingers and mixed, or multiplied together, by nonlinearities in the silicon which are either in the space-charge layer underlying the fingers, in the CCD transfer gate, or both. The mixing products from this nonlinear interaction are accumulated in wells under the signal, sample, storage, transfer, and ϕ_1 gates (shown in Fig. IV-1) by stopping the CCD clocks with ϕ_1 high during the accumulation interval. Prior to launching the acoustic waves, the wells under these gates were half-filled with charge.⁴ Thus, the multiplication and accumulation produce a spatial variation of the initially uniform charge distribution in the CCD, with the charge in each CCD ϕ_1 well now representing a discrete sample of the correlation of the signal waveform with the reference waveform. When the charge is clocked out of the CCD at a convenient data rate, this spatial variation becomes a time-sampled data representation of the desired correlation function.

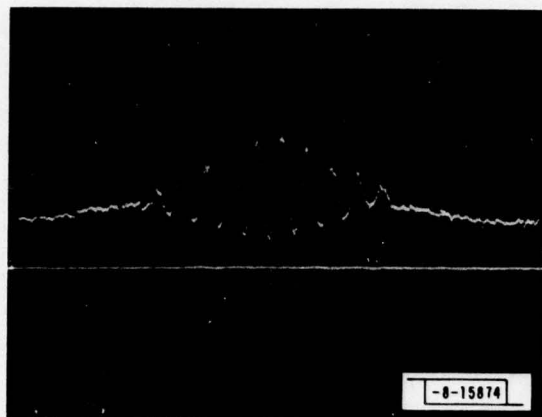


Fig. IV-2. Oscillograph of accumulating correlator operation at an input carrier frequency of 89 MHz and an output clock rate of 100 kHz. Input signal and reference pulse widths are 1.6 μ sec.

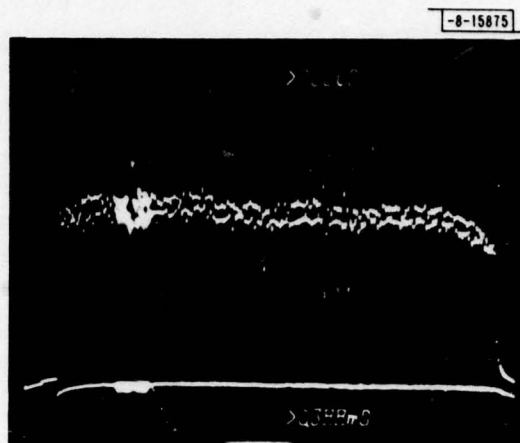


Fig. IV-3. Accumulating correlator output at an input signal frequency of 97 MHz with an input S/N of 0 dB. Signal and reference are phase-encoded with a bandwidth of 20 MHz. Intensified portion of oscilloscope trace is shown with an expanded time scale in Fig. IV-4(a).

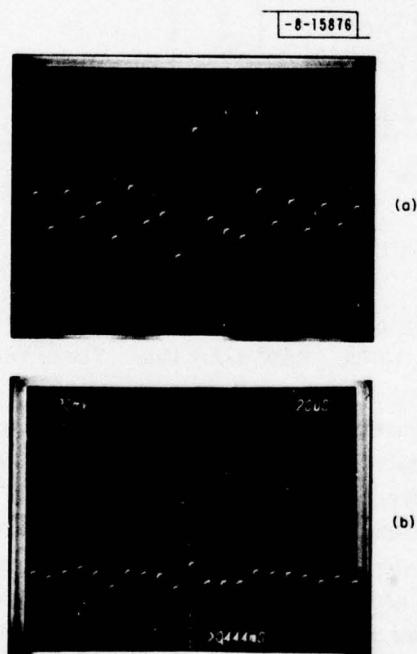


Fig. IV-4. Correlator output with input signal masked by noise, demonstrating a signal-processing gain of 20 dB. (a) Input S/N of 0 dB; (b) input S/N of -20 dB.

A simple example of this correlation mode is shown in Fig. IV-2, where both the signal and the reference are 1.6- μ sec-long rectangular pulses (a single code bit) at a carrier frequency of 89 MHz. The output waveform is the expected triangular cross-correlation function of the input waveforms. The effective output carrier frequency ($10.5 \text{ cycles}/1.6 \mu\text{sec} = 6.6 \text{ MHz}$) results from sampling the 178-MHz product frequency at the second harmonic of the effective 85.7-MHz sampling frequency of the fingers.⁵

The utility of this device is its ability to perform, under programmable control, correlation of waveforms much longer than the 3.5- μ sec SAW propagation delay time of the structure. As a demonstration, we have tested this accumulating correlator device with constant-amplitude, biphasic-encoded, pseudorandom waveforms with a rate (bandwidth) of 20 MHz, a duration of 100 μ sec, and with one of the inputs corrupted by Gaussian noise of the same 20-MHz bandwidth. The full 300-tap correlation output spanning a 7- μ sec time window at an input signal-to-noise ratio (S/N) of 0 dB is shown in Fig. IV-3, where the correlation peak is in the intensified region of the oscilloscope trace. The peak occurs at that tap for which reference and signal were in synchronism. Offsetting the signal-to-reference-code timing produces a predictable time displacement in the correlation peak. The sidelobes of the correlation function are exhibited in this photograph as a vertical spread in the output sampled-data points. Some leakage-current spikes, bad storage sites, and fixed pattern noise⁴ can also be seen in this photograph. These artifacts are caused by defects and inhomogeneities in the silicon and are independent of the input signal amplitude, and could therefore be subtracted out by a post-processor.

The intensified part of the correlation output of Fig. IV-3 is shown with an expanded time scale in Fig. IV-4(a). If the input signal is reduced by 20 dB while keeping the reference and noise unchanged, the output shown in Fig. IV-4(b) is obtained. By comparing Fig. IV-4(a) with (b), it can be seen that the correlation peak and the sidelobes drop, as expected. The correlation peak is still in evidence, even though the input signal is now buried in noise. A processing gain of 30 dB has been observed by gating on and off a signal at a level 30 dB below the noise. Under these conditions, the correlation peak was observed to move up and down. However, the sidelobes are now masked by the fixed-pattern noise, which limits the useful processing gain of the prototype to approximately 20 dB rather than the theoretical gain of $33 \text{ dB} = 10 \log (20 \text{ MHz} \times 100 \mu\text{sec})$.

The performance of this SAW/CCD accumulating correlator is given in Table IV-1. In summary, we have demonstrated a SAW/CCD accumulating correlator. The important feature of this device is that it can correlate wideband analog signals of long duration against controlled reference waveforms. The signal processing is performed by multiplication and time integration of discrete samples of the input analog signal with discrete samples of an analog reference, and the device provides an output of 300 discrete samples of the correlation in a 7- μ sec time window after each accumulation interval. The unique hybrid structure combines a number of significant advantages not previously achieved by any one of the competing devices. These advantages include analog-analog correlation, programmability, wide input bandwidth, selectable output data rate, and compactness.

We are in the process of performing experiments to help us more fully understand the physical mechanisms underlying the correlation and accumulation so that we can optimize the design and build an accumulating correlator device with improved performance.

D. L. Smythe
R. W. Ralston

TABLE IV-1
SAW/CCD ACCUMULATING CORRELATOR PERFORMANCE SUMMARY

Input Center Frequency	97 MHz
Input Bandwidth	20 MHz
Maximum Accumulation Time	100 μ sec
Time Window	7 μ sec
Output Clock Rate	100 kHz
Maximum Input Power (1-dB compression)	27 dBm
Maximum Output Level	35 mV rms
Dynamic Range	20 dB
Time-Bandwidth Product	2000

B. COMPARISON OF COPLANAR WAVEGUIDE AND MICROSTRIP FOR GaAs MONOLITHIC INTEGRATED CIRCUITS

Coplanar waveguides (CPW) are often suggested as an alternative to microstrip lines in GaAs monolithic microwave integrated circuits, especially when the active elements include planar diodes and GaAs FETs. Here, we compare losses in coplanar waveguides with those in microstrip lines to provide a basis for the choice of the guide. We have calculated conductor and dielectric losses in each case, and have also obtained the radiation losses for respective half-wavelength resonators. The results are presented in terms of the quality factor Q of these resonators. When the ground-plane spacing (see Fig. IV-5) of the coplanar waveguide is identical

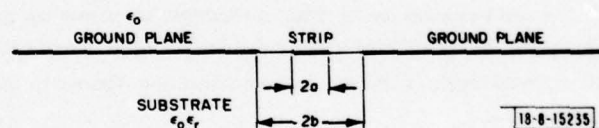


Fig. IV-5. Geometry of coplanar waveguide.

to the substrate height of the optimum microstrip line, the CPW Q 's are lower. But when the ground-plane spacing is allowed to increase, the Q factors approach that of the microstrip line. Increasing the ground-plane spacing in coplanar waveguides is possible since the radiation losses are much less due to the antiphase excitation of the adjacent radiating slots. Thus, in the cases considered, the choice of guide may be resolved by considerations other than loss.

1. Calculation of Q

The conductor and dielectric loss constants α_c and α_d , respectively, are estimated as described below, and from these the circuit quality factor Q_0 is obtained. Note that the stored energy U in a $\lambda_g/2$ resonator, with the voltage distribution of $V \sin \beta_g z$, is given by

$$U = \frac{V^2}{8Z_0 f} \quad (\text{IV-1})$$

and the power loss W_l by

$$W_l = \frac{1}{4} \frac{V^2}{Z_0} \lambda_g (\alpha_d + \alpha_c) \quad (IV-2)$$

where λ_g is the guide wavelength, β_g is the propagation constant of the guide, z is the distance along the resonator, Z_0 is the characteristic impedance, and f is the frequency. Thus, the circuit Q is given by

$$Q_o = \frac{2\pi f U}{W_l} = \frac{\pi}{\lambda_g (\alpha_c + \alpha_d)} \quad (IV-3)$$

The radiation Q is estimated by calculating the total power radiated W_r , and then evaluating the ratio

$$Q_r = \frac{2\pi f U}{W_r} \quad (IV-4)$$

The total Q is given by

$$\frac{1}{Q_t} = \frac{1}{Q_o} + \frac{1}{Q_r}$$

2. Calculation of Losses

a. Coplanar Waveguide

The coplanar-waveguide impedance, velocity, and effective dielectric constant for different a/b (strip width to ground-plane spacing) ratios are calculated assuming quasi-static TEM propagation. The Green's-function approach is used, and for computational convenience a secondary ground plane is assumed to exist some large distance from the guide. Calculations of the even- and odd-mode charge distributions and subsequent subtraction of these ensure that the presence of this ground plane does not have any effect. Results obtained by computer calculations agree with those of Wen.⁶ The impedances, however, are higher by a few percent due to the finite thickness of the substrate.⁷

The conductor loss factor in neper/m is estimated using the equation:

$$\alpha_c = \frac{R_s}{2Z_0 I^2} \left(\int_{-a}^{+a} J_s^2 dx + 2 \int_b^\infty J_{gp}^2 dx \right) \quad (IV-5)$$

and the dielectric loss factor by

$$\alpha_d = \frac{q \epsilon_r}{\epsilon_{eff}} \frac{\tan \delta}{\lambda_g} \quad (IV-6)$$

where

J_s is the strip longitudinal current distribution,

J_{gp} is the ground-plane current distribution of the CPW,

I is the total strip or ground-plane current,

ϵ_r is the substrate relative dielectric constant,

ϵ_{eff} is the effective dielectric constant, and

$\tan \delta$ is the substrate loss factor.

The current distributions, impedance, and the effective dielectric constant estimated from the computer calculations are used to obtain α_c , α_d and, subsequently, Q_0 for different a/b ratios.

Radiation from a half-wavelength resonator is calculated by assuming that the electric fields in the gap between strip and ground plane (see Fig. IV-5) give rise to magnetic currents which radiate. The standard formula⁸ for radiation from a resonant slot is used, with corrections for the resonant length, which is reduced due to the substrate; the presence of the pair of slots excited in antiphase is also taken into account. The power radiated into the air and dielectric regions are estimated separately and summed, and the radiation Q is estimated from Eq. (IV-4). Results have been obtained for both open- and short-circuit resonators.

b. Microstrip

The microstrip loss calculations follow well-documented methods^{9,10} for conductor and dielectric loss factors. The radiation loss is estimated following the approach of Easter and Roberts.¹¹ The Q factors follow similar trends to those observed by others.¹²

3. Results

Since the purpose here is to try to resolve the choice of guiding structure for GaAs monolithic circuits, all results have been obtained for $\epsilon_r = 13$ and $\tan \delta = 10^{-3}$. No surface roughness factor has been included. Calculations have been performed at 8 GHz, assuming gold metallization $\sigma = 4.1 \times 10^7$ mhos/m, thickness 3 μm .

Figure IV-6 summarizes the results for half-wavelength open-circuit coplanar waveguide resonators with ground-plane spacings of 0.5, 1.0, and 2.0 mm for different impedances. (Note that the impedance variation with a/b is available in the literature.^{6,7}) The highest Q_t is obtained for a ground-plane spacing of 1.0 mm, and reaches a value of 160. Figure IV-7 compares the

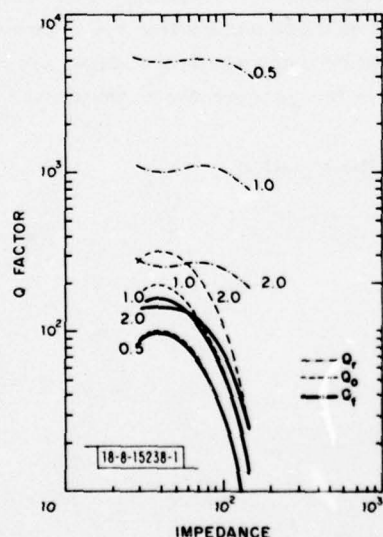


Fig. IV-6. Quality factor vs impedance for CPW $\lambda_g/2$ open-circuit resonators for $2b = 0.5, 1.0$, and 2.0 mm. $\epsilon_r = 13$, $\tan \delta = 10^{-3}$, $f = 8$ GHz.

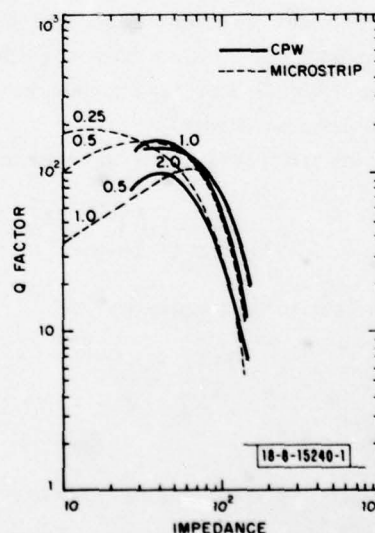


Fig. IV-7. Comparison of Q_t factors of microstrip and CPW $\lambda_g/2$ open-circuit resonators for $h = 0.25, 0.5$, and 1.0 mm and $2b = 0.5, 1.0$, and 2.0 mm, respectively.

microstrip Q of $\lambda_g/2$ resonators for $h = 0.25, 0.5$, and 1.0 mm with those of the CPW resonators. The Q of the 0.5 -mm substrate microstrip resonators are similar to those of the CPW resonators with ground-plane spacing of 1.0 mm, but the CPW resonators with 0.5 -mm ground-plane spacing show much lower Q .

Thus it appears that choice between the guides is not clear on the basis of loss. Other considerations may determine the choice, and some of these are as follows. The CPW, as a planar structure, allows shunt and series elements to be incorporated with ease, though some care needs to be exercised with shunt elements to retain symmetry in order to prevent the excitation of spurious slot modes. Microstrip shunt elements require the drilling of holes in the substrate and subsequent processing or, alternatively, the use of wraparound ground planes. The packaging of the CPW circuits in principle requires that the enclosures provide space both above the metallization and also below the substrate, and omission of the latter for reasons of convenience and cost may result in the excitation of spurious circuit responses. Microstrip enclosures require air space only above the substrate. To retain comparable loss performance, the CPW ground-plane spacing has to be over twice the equivalent microstrip substrate height, and circuits, in general, may require larger substrate areas when compared with equivalent circuits in microstrip. Realization of complex circuits in CPW may result in isolated ground-plane regions, with associated problems. Thus, the choice of guiding structure is determined by the designer.

A. Gopinath

REFERENCES

1. Solid State Research Report, Lincoln Laboratory, M.I.T. (1978:3), pp. 31-32, DDC AD-A065116.
2. O. Menager and B. Desormiere, *Appl. Phys. Lett.* **27**, 1 (1975).
3. Solid State Research Report, Lincoln Laboratory, M.I.T. (1978:1), pp. 34-36, DDC AD-A056715/6.
4. D. L. Smythe, R. W. Ralston, and B. E. Burke, 1978 International Conference on the Applications of CCDs Processes (Naval Ocean Systems Center, San Diego, 1978), p. 4.65.
5. Solid State Research Report, Lincoln Laboratory, M.I.T. (1977:4), pp. 37-39, DDC AD-A052463/7.
6. C. P. Wen, *IEEE Trans. Microwave Theory Tech.* **MTT-17**, 1087 (1969).
7. M. E. Davis, E. W. Williams, and A. C. Celestini, *IEEE Trans. Microwave Theory Tech.* **MTT-21**, 594 (1973).
8. S. Ramo and J. R. Whinnery, Fields and Waves in Modern Radio (Wiley, New York, 1953), p. 535.
9. R. A. Pucel, D. J. Masse, and C. P. Hartwig, *IEEE Trans. Microwave Theory Tech.* **MTT-16**, 342 and 1064 (1968).
10. A. Gopinath, R. Horton, and B. Easter, *Electron. Lett.* **6**, 40 (1970).
11. B. Easter and R. J. Roberts, *Electron. Lett.* **6**, 573 (1970).
12. E. Belohoubek and E. Denlinger, *IEEE Trans. Microwave Theory Tech.* **MTT-23**, 522 (1975).

V. SURFACE-WAVE TECHNOLOGY

A. HYBRID SAW CHIRP-FOURIER-TRANSFORM SYSTEM

The availability of large RAC (reflective array compressor) dispersive delay lines with large time-bandwidth products and with relatively precise phase and amplitude response¹⁻³ has stimulated a great deal of interest in the use of these devices in chirp-transform systems to perform high-speed analog Fourier transforms.⁴⁻¹³ For situations in which the input signal is analog and its bandwidth and duration fall within the bounds achievable with SAW dispersive delay lines, SAW chirp-transform systems usually represent the most efficient technique (in terms of size, cost, power, and speed) available for performing spectral analysis.^{11,14} When compared with digital FFT computers, SAW chirp-Fourier-transform systems appear especially attractive when measured in terms of equivalent rates of mathematical operations per unit of cost, size, or power.^{11,14,15} The goal of the work described here is the development of a hybrid Fourier-transform-computing module which accepts digital input data, efficiently converts it to analog, and exploits the capabilities of an analog chirp-transform system to compute the transform at high speed with minimum power.

In order to implement this digital-in/digital-out signal processing, a hybrid chirp-Fourier-transform system which contains a series of conversion stages was configured. The system accepts input words consisting of 8-bit real and 8-bit imaginary parts. These words are converted to an analog signal and processed in real time through one of two duplicate transform circuits which operate in a ping-pong fashion. The analog output of the circuits is converted to complex digital words. As a digital computing element, the system computes the transforms of contiguous 256-word data blocks at a throughput rate of 10 Mwords/sec.

Present RAC technology is capable of providing devices with phase error of approximately 1° rms and amplitude errors of the order of ± 0.3 dB. With these characteristics, Fourier transforms accurate to about 1 percent are possible. A major task in this program is to demonstrate an analog system with this level of accuracy. The equivalent digital precision is 8 bits (including a bit for sign).

A block diagram of the hybrid transform processor is shown in Fig. V-1. In order to test the system by means of a standard low-speed computer, high-speed input and output buffer memories are employed. Data blocks consisting of 256 complex words are read out of the input buffer at a rate of 10 Mwords/sec and converted to in-phase (real) and quadrature (imaginary) baseband signals. These signals are modulated onto a 165-MHz carrier, processed by the chirp-transform system, translated back to a 165-MHz carrier, demodulated to baseband, and A/D converted to yield the real and imaginary parts of the Fourier transform.

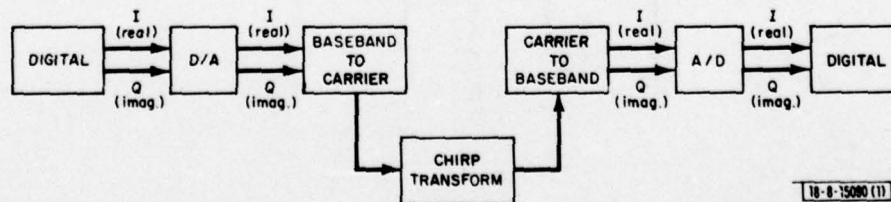


Fig. V-1. Block diagram of hybrid chirp-Fourier-transform system.

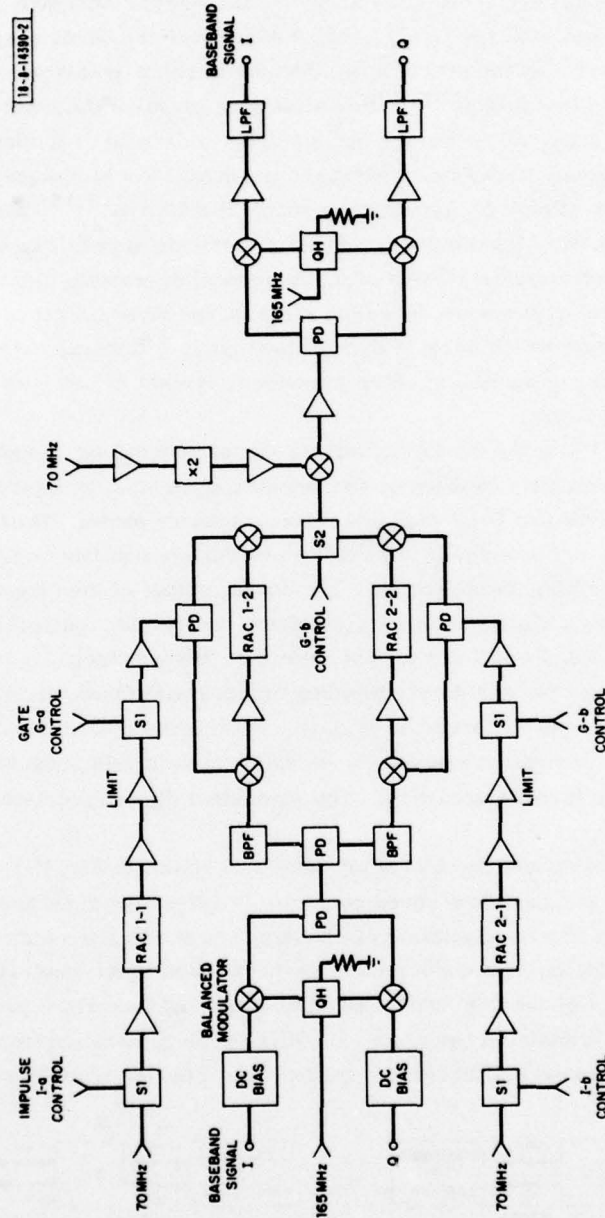


Fig. V-2. Schematic diagram of analog portion of chirp-Fourier-transform subsystem.

A schematic diagram of the analog portion of the system is shown in Fig. V-2. It consists of duplicate chirp-Fourier-transform circuits in the conventional multiply-convolve-multiply configuration. The mathematical description of the operation of this circuit has been extensively described.^{16,17} Contiguous 25.6- μ sec complex data blocks from a continuous data stream are processed by the two matched transform circuits which are connected in a side-by-side arrangement. Each operates sequentially over a 50-percent duty cycle in a ping-pong fashion.

The flexibility afforded by computer generation of test waveforms allowed a large amount of data on many aspects of overall system performance to be accumulated over a short time. Selected examples are presented. Much of the data is in the form of photographs of oscilloscope traces showing the baseband input waveforms generated by the D/A converters, and the output Fourier-transform waveforms present at the input to the A/D converters (see Fig. V-1). The in-phase and quadrature waveforms correspond to the real and imaginary components, respectively. When a single input waveform is shown, it represents the output of the D/A converter connected to the in-phase channel. Such an input corresponds to a purely real function.

The relatively simple D/A conversion process currently employed causes a modification of the computed Fourier transform. In this mode, each digital word generates a constant voltage in a sample-and-hold circuit for the duration of each clock cycle. This causes a $(\sin x)/x$ roll-off in the computed transform. This is evident in the transform of the 100-nsec-wide pulse generated by a single nonzero real digital word at the center of the data block, as shown in Fig. V-3. Only the in-phase (real) component of the output is nonzero. The detailed spectral shape is approximately $(\sin x)/x$, and the 3.5-dB roll-off of the band edges agrees to within 0.1 dB with the spectral response measured with a standard spectrum analyzer. This roll-off is not fundamental and can be eliminated by improved D/A conversion techniques.

Figure V-4 demonstrates the system's 100-percent duty cycle. The upper trace shows a 2- μ sec pulse within each data block. The pulse occurs in the I (real) channel. The real and

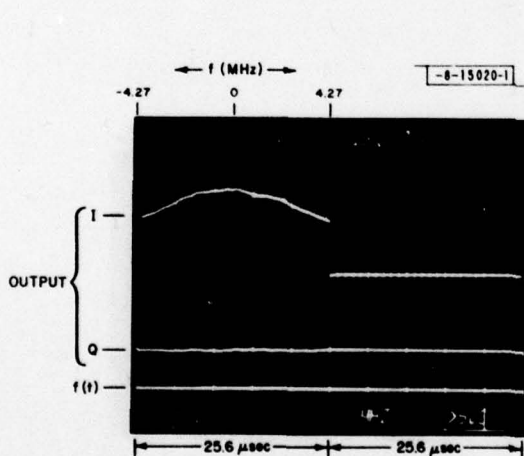


Fig. V-3. Transform of digital impulse. In-phase and quadrature output components shown in top two traces. Input waveform is shown in bottom trace.

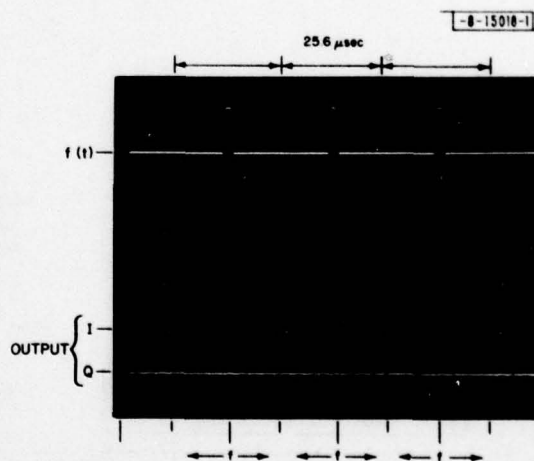


Fig. V-4. Operation at 100-percent duty cycle. Contiguous data blocks each containing a single video pulse are shown in top trace. In-phase and quadrature components of Fourier transform are shown in bottom two traces.

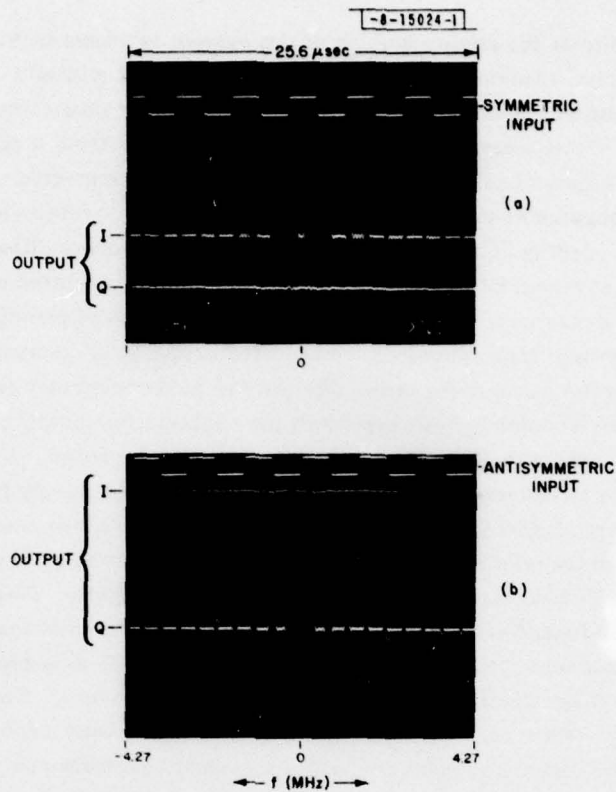


Fig. V-5. (a) Symmetric square wave and its real and even Fourier transform; (b) antisymmetric square wave and its imaginary and odd Fourier transform.

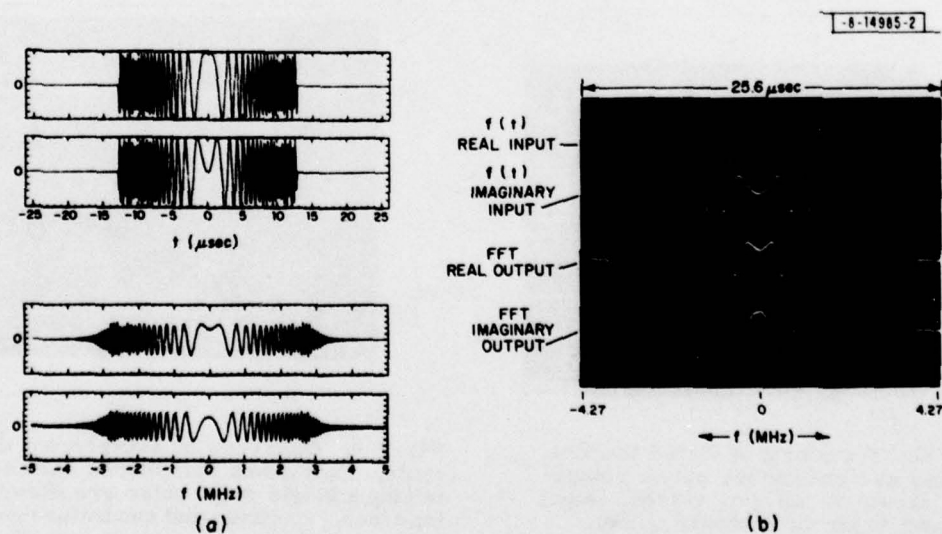


Fig. V-6. Complex baseband chirp and its Fourier transform: (a) theoretical, and (b) measured.

imaginary components of the complex Fourier transform are represented by in-phase and quadrature baseband signals shown in the lower two traces. The transform is provided in real time delayed by 51.2 μsec . The outputs from the two halves of the analog circuit are essentially indistinguishable. This indicates that a precise match in both phase and amplitude has been achieved between the two ping-pong circuits.

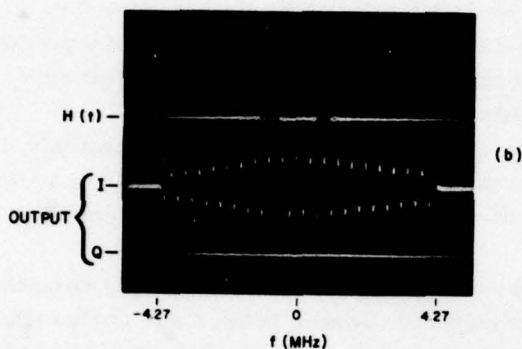
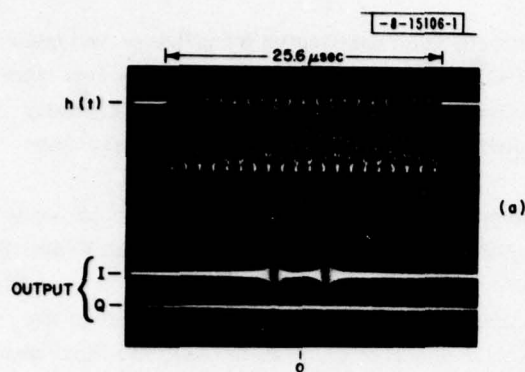
The issues of timing and phasing, balance between I and Q channels, and the overall accuracy of the analog system were explored, in part, by the test waveforms shown in Figs. V-5(a-b) and V-6(a-b).

Transforms of square waves which are symmetric and antisymmetric with respect to the center of data block are shown in Figs. V-5(a) and (b), respectively. In each case, the input was to the in-phase channel, and thus corresponded to a real input function. Output waveforms show that the odd harmonics present in the spectrum of a square wave fall off at the predicted rate of $1/n$. The measured values, with accuracy limited by the linearity of the display, agreed to within 3 percent of the theoretical values. The effect of processing a finite segment of a periodic function is to convolve the spectrum with a $(\sin x)/x$ response. The detailed sidelobe patterns shown in Fig. V-5(a-b) are predicted by the computed transform.

The ability to go from a clean zero output in the Q channel when the input waveform is symmetric [Fig. V-5(a)] to a clean zero in the I channel when the input is antisymmetric [Fig. V-5(b)] demonstrates that the two output signals are in quadrature. A deviation from quadrature by as little as 1° becomes noticeable.

The test waveforms shown in Fig. V-6(a-b) yielded nonzero signals in the I and Q channels at both the input and output. This provided a test of amplitude balance in the I and Q channels. For this test, we exploited the ability of the digital system to generate a variety of baseband waveforms in functional form not otherwise easily obtainable. Figure V-6(a-b) shows the results obtained with an input chirp waveform, $f(t) = \exp[-j\pi t^2/2]$. The real and imaginary components of the input function and the D/A-converted waveforms are shown in the upper traces of Figs. V-6(a) and (b), respectively. The measured in-phase and quadrature components shown in the lower traces of Fig. V-6(b) compare in detail with the calculated transform shown in Fig. V-6(a). For example, the small ripple in the frequency response near DC is likewise present in the measured transform.

One test of the A/D conversion process is illustrated by the results shown in Fig. V-7(a-b). Here the input waveform is a cosine function $h(t)$ in the real input channel. The cosine is symmetric within the 25.6- μsec data block. Alternate data blocks are left empty to conveniently define the zero level. The I and Q components of the resulting transform $H(f)$, shown in the lower two traces [Fig. V-7(a)], are A/D converted and read into computer memory for storage. Subsequently, this file was recalled and redefined as the new input file $H(t)$. The sampled waveform is shown in the top trace of Fig. V-7(b). Its real transform, $h'(-f)$, is shown in the lower two traces [Fig. V-7(b)]. The symmetry theorem states that if $h(t)$ and $H(f)$ are a Fourier-transform pair, then $H(t)$ and $h(-f)$ are also a pair. Thus, if the transform of a real even function, such as used here, is recycled through the system, the output in the frequency domain should be the same as the original input time function. Figure V-7(a-b) illustrates this result. The final transform yields a waveform nearly identical to the input except for a roll-off toward the ends of the transform. The roll-off is the predicted result caused by the frequency roll-off of the D/A converted samples, as illustrated in Fig. V-3. The details of the final output, as shown in Fig. V-7(b), are sensitive to the initial transform being centered in the 25.6- μsec output data



SYMMETRY PROPERTY:
IF $h(t) \leftrightarrow H(f)$,
THEN $H(f) \leftrightarrow h(-t)$

Fig.V-7. Fourier transform symmetry property illustrated (a) input $h(t)$ and its Fourier transform $H(f)$, and (b) input $H(t)$ and its Fourier transform $h'(-f)$.

block. Therefore, the cascaded transforms are also a critical check on system timing and phasing.

The dynamic range of the analog portion of the system was tested, in part, with a CW signal which fully filled each data block. Dynamic range was defined as the ratio of the level of the maximum input for linear operation to the level of input which yielded unity signal-to-noise at the output. When measured before the post-multiply mixers, the dynamic range is well in excess of 70 dB. However, the several mixers in the output circuit limited the dynamic range to approximately 70 dB. This is equivalent to 13 bits in the output of a digital FFT. To obtain this, many more than 13 bits would have to be carried during intermediate digital calculations. The large analog dynamic range is a direct result of the use of RAC devices with low insertion loss.

V. S. Dolat L. A. Veilleux
G. R. McCully R. C. Williamson

B. INTEGRATING CORRELATOR: 4-WAVE INTERACTIONS

The integrating correlator is a relatively new acoustoelectric device, with a structure consisting of a LiNbO_3 surface-acoustic-wave (SAW) delay line on which counterpropagating reference and signal waves are launched and a Si strip whose surface is spaced (~ 350 nm) from the surface of the LiNbO_3 . The silicon nonlinearities provide local mixing of the evanescent

RF fields which accompany the SAWs. The Si surface adjacent to the LiNbO_3 is covered with a high-density ($3.8\text{-}\mu\text{m}$ periodicity) array of PtSi Schottky diodes. The DC component of the local product signal is temporally integrated as a stored charge on each diode, and since each diode represents a different delay between reference and signal, the charge on each diode represents a discrete point in the correlation function of reference and signal. A second parametric interaction between a scanning SAW pulse and the spatial charge pattern stored on the diode array provides a readout of the correlation function.

This device, then, provides a potential of performing the desired differential delay, mixing, and integration all in one small package with an equivalent of over 500 taps spanning a $20\text{-}\mu\text{sec}$ time window. Furthermore, the reference function is electrically programmable and the integration time is not limited by the substrate size. Utilizing the slow charging of the diode array by the reference-signal parametric interaction allows correlation of phase-modulated waveforms which are about 10^3 times longer than the $20\text{-}\mu\text{sec}$ acoustoelectric interaction region, hence producing large processing gains for wideband analog signals.

The earliest implementation of the integrating correlator utilized a 3-wave parametric interaction in which the signal and reference waves were centered about the same RF carrier. As a result, there also existed a degeneracy between the frequency of the scanning waveform and the correlator output, a degeneracy intrinsic to this 3-wave interaction. This degeneracy compounds the problem of providing a device output uncorrupted with spurious signals generated by the scan pulse.¹⁸ In order to specifically avoid such scan-related spurious signals, we have developed a new approach which utilizes a 4-wave parametric interaction and which thereby lifts the degeneracy between scan and output frequencies. Even more importantly, perhaps, the 4-wave parametric interaction provides an analog method of performing triple-product correlation¹⁹ and, as such, will likely allow implementation of new signal-processing capabilities.

Figure V-8(a-b) is a schematic representation of the 4-wave interaction tested, showing both the device configuration and temporal frequency - spatial frequency (ω - k) plane. The concepts pertaining to such a representation of these and other collinear parametric interactions

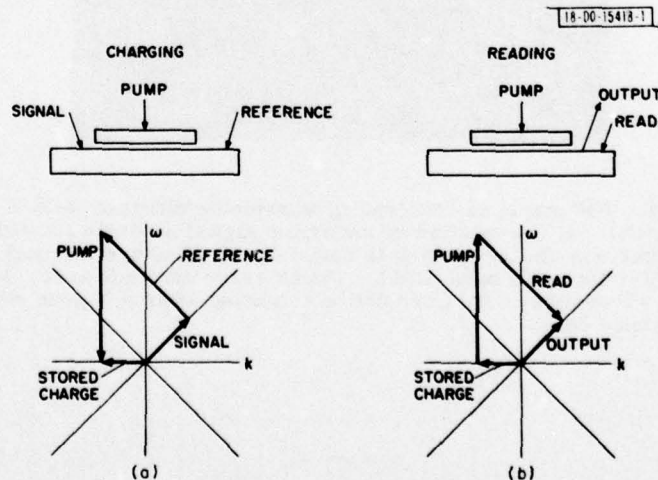


Fig. V-8. Schematic of 4-wave operation depicting pumping of silicon and acoustic inputs and output with representation of appropriate parametric interactions in the ω - k plane for (a) charging and (b) subsequent reading of the correlation.

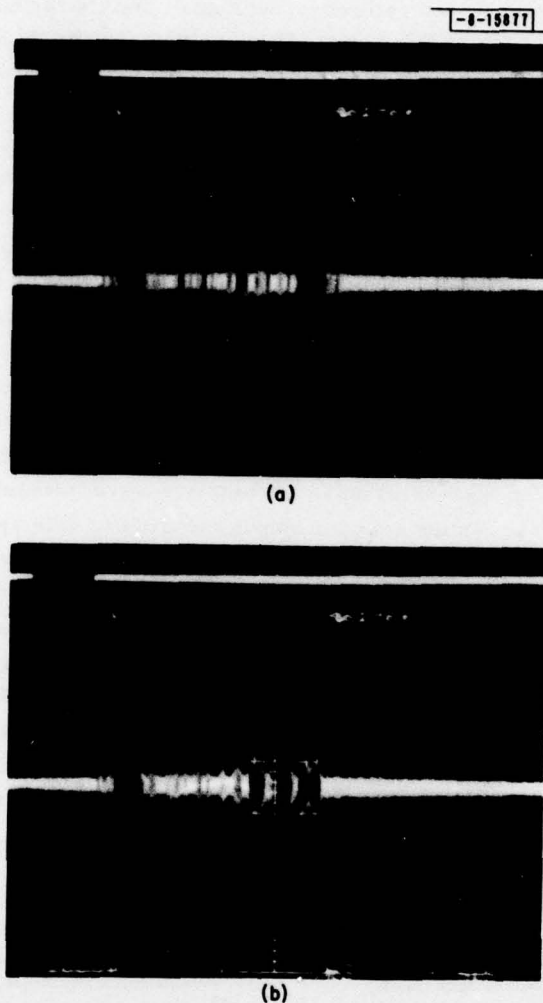


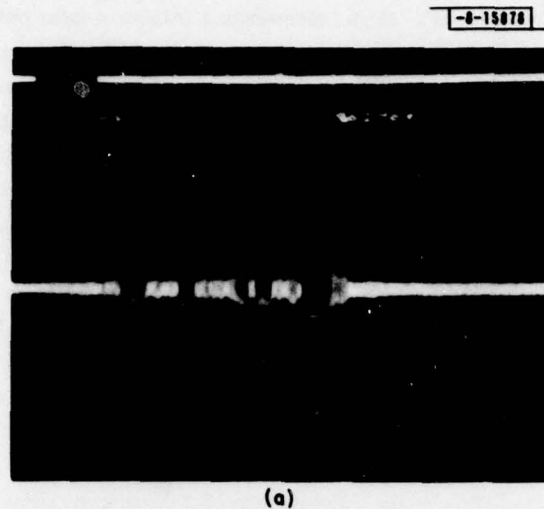
Fig. V-9. RF output of integrating correlator obtained with 4-wave interaction. (a) Correlation of maximum signal strength showing reduced spurious clutter, which is now only 10 dB above thermal noise floor (10-MHz noise bandwidth). Upper trace shows 6- μ sec, 2-MHz reading chirp input. (b) Correlation resulting after a 2- μ sec advance in reference code.

are more fully described elsewhere.¹⁹ As indicated in Fig. V-8(a), a forward propagating signal (ω_s, k_s) mixes with a reverse propagating reference ($\omega_r, -k_r$) in the presence of a high-power pump ($-\omega_s - \omega_r, 0$) via the cubic nonlinearity of the Si to produce a stored charge pattern ($0, k_s - k_r$). In Fig. V-8(b) this correlation charge is read out with a reverse propagating pulse ($-\omega_r, k_r$) in the presence of the same pump ($\omega_s + \omega_r, 0$), and the output (ω_s, k_s) is obtained as a forward traveling wave at a separate transducer. Both interactions utilize a sum pump, which has the advantage during charging of downconverting the k pattern such that it can be easily accommodated by the periodicity of the diode array, as well as the advantage during reading of producing an output at frequencies well below those of the read excitation. For clarity, only the carrier-frequency vectors are indicated, although in fact the interactions are wideband, and thus all vectors have a range in magnitude with the exception of the narrow-bandwidth pump. It should be noted that the sum-pump interaction used here may be limited to processing signal waveforms with real baseband representations, as the multiplication is occurring with spectral inversion implied. The more general wideband interaction would utilize a difference pump.¹⁹

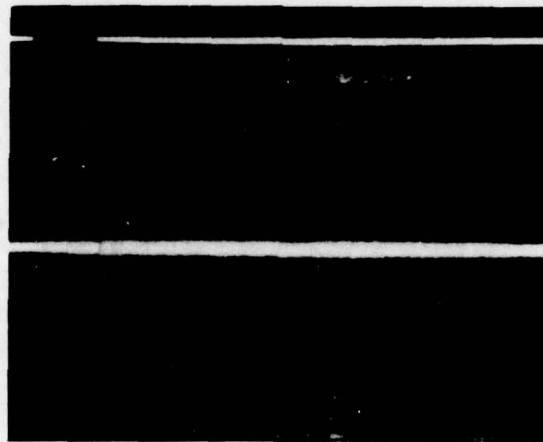
The wideband nature of the depicted interaction has been demonstrated using pseudonoise (PN) biphase modulation of the RF signal and reference carriers at a 2-MHz chipping rate. As described elsewhere,¹⁸ it is desirable to limit readout filling-factor loss by spatially spreading the correlation peak during the charging process and subsequently recompressing the peak during the reading process. This is accomplished by convolving the reference waveform with a linear dispersive transversal filter with a bandwidth of 2 MHz and duration time of 6 μ sec. The impulse response of that same filter is used to produce the linearly chirped read waveform. This process results in a quite manageable -10.5-dB filling-factor loss for the 20- μ sec interaction length, while providing a 14- μ sec time window within which to measure the code timing.

RF output waveforms observed after nearly 10-msec integration of 2-MHz PN codes for the 4-wave interaction are shown in the oscillographs of Fig. V-9(a-b). A relative timing displacement of 2 μ sec between signal and reference codes produces the expected displacement of the resultant correlation peak. The spurious levels accompanying the 4-wave interaction are shown in Fig. V-10(a-b). Under conditions where the 3-wave process (not shown) provides 0-dB dynamic range due to scan-related spurious signals, the use of the 4-wave process provides a 17-dB dynamic range. For both parametric processes the signal, reference, and read powers were maintained constant at 22, 18, and 16 dBm, respectively. The 3-wave process had a degenerate carrier frequency of 61 MHz, while the 4-wave process had 61-MHz signal and output carriers, 122-MHz reference and read carriers, and a 183-MHz pump. (It is, of course, not necessary to maintain a harmonic relationship between the three frequencies.)

These preliminary experiments employed PtSi Schottky diodes fabricated on uniformly doped 30- Ω -cm n-type silicon, and such barriers act as abrupt varactors with a predominant quadratic dependence of capacitance on voltage. Hence, the 3-wave parametric interaction is substantially more efficient than the 4-wave process in the current device. A pump power of 38 dBm (the maximum available) was required to produce the 4-wave result of Fig. V-9(a) with a peak output power of -74 dBm, some 22 dB below the -52-dBm output for the 3-wave process. The presence of the high-power pump, in addition to producing the 4-wave interaction, acts alone on the diodes so as to rapidly charge the array into a uniform (zero- k) reverse bias, which would widen the silicon depletion layer to such an extent that effective interaction with the evanescent RF fields accompanying the acoustic waves launched by the signal, reference, and read inputs would cease. The undesirable buildup of this large uniform charge is very effectively balanced



(a)



(b)

Fig. V-10. Spurious signals produced by reading (a) after no correlation was stored, and (b) in the absence of pump power.

by the use of low-level illumination provided by light-emitting diodes (LEDs). These LEDs already exist in the device structure as a means for rapidly erasing, at a much higher illumination level, the stored correlation prior to initiating a new integration sequence.¹⁸

The relative merits and design trade-offs of the two parametric interactions can be summarized as follows. The 3-wave interaction is efficient, but plagued by spurious bulk waves which accompany the read waveform. The 4-wave interaction is inefficient, but is relatively free of all read-produced spurious signals. A study to optimize the cubic nonlinearity by tailoring the doping profile of the silicon substrate is beginning, and other device modifications will be made as well to increase the dynamic range. Although this first acoustoelectric implementation of the triple-product correlation/convolution was initially motivated by the desire to reduce spurious signals in a double-product process, it is evident that a triple-product acoustoelectric interaction offers a class of signal-processing functions previously achieved only in cumbersome digital or optical hardware. The ability to perform triple-product correlation/convolution in a compact acoustoelectric device promises to lead to interesting new system capabilities in the future.

R. W. Ralston

REFERENCES

1. R. C. Williamson and H. I. Smith, IEEE Trans. Microwave Theory Tech. MTT-21, 195 (1973), DDC AD-772211/9.
2. R. C. Williamson, Proc. IEEE 64, 702 (1976), DDC AD-A028461/2.
3. H. M. Gerard, O. W. Otto, and R. D. Weglein, "Development of a Broad-band Reflective Array 10,000:1 Pulse Compression Filter," in 1974 Ultrasonics Symposium Proceedings (IEEE, New York, 1974), pp. 197-201.
4. G. R. Nudd and O. W. Otto, "Chirp Signal Processing Using Acoustic Surface Wave Filters," in 1975 Ultrasonics Symposium Proceedings (IEEE, New York, 1975), pp. 350-354.
5. J. D. Maines, G. L. Moule, C. O. Newton, and E. G. S. Paige, "A Novel SAW Variable-Frequency Filter," ibid., pp. 355-358.
6. R. M. Hays, W. R. Shreve, D. T. Bell, Jr., L. T. Claiborne, and C. S. Hartman, "Surface Wave Transform Adaptable Processor System," ibid., pp. 363-370.
7. C. Atzeni, G. Manes, and L. Masotti, "Programmable Signal Processing By Analog Chirp-Transformation Using SAW Devices," ibid., pp. 371-376.
8. H. J. Gerard and O. W. Otto, "A Programmable Radar Pulse Compression Filter Utilizing Chirp Transform Correlation," in 1976 Ultrasonics Symposium Proceedings (IEEE, New York, 1976), pp. 371-375.
9. M. A. Jack, G. F. Manes, P. M. Grant, C. Atzeni, L. Masotti, and J. H. Collins, "Real Time Network Analysers Based on SAW Chirp Transform Processors," ibid., pp. 376-381.
10. J. D. Collins, W. A. Sciarretta, D. S. MacFall, and M. B. Schulz, "Signal Processing With CCD and SAW Technologies," ibid., pp. 441-450.
11. H. M. Gerard and P. S. Yao, "Performance of a Programmable Radar Pulse Compression Filter Based on a Chirp Transformation with RAC Filters," in 1977 Ultrasonics Symposium Proceedings (IEEE, New York, 1977), pp. 947-951.
12. P. M. Grant and M. A. Jack, "Design and Applications of CCD-SAW Fourier Transform Processors," ibid., pp. 957-960.
13. M. Alldritt, R. Jones, C. J. Oliver, and J. M. Vaughn, J. Phys. E: Sci. Instrum. 11, 116 (1978).
14. K. Preston, Session 6. Task Report, SPIE Vol. 128 Supplement - Effective Utilization of Optics in Radar Systems (1977), pp. 35-42.
15. T. Beauvais, R. Carre, and H. Gautier, "Interfacing and Comparison of Surface Acoustic Wave and Digital Technologies," in IEE Conf. Publ. No. 144 - The Impact of New Technologies in Signal Processing, Aviemore, Scotland, September 1976, pp. 44-52.
16. O. W. Otto, "The Chirp Transform Signal Processor," in 1976 Ultrasonics Symposium Proceedings (IEEE, New York, 1976), pp. 365-370.
17. M. A. Jack and J. H. Collins, "Fast Fourier Transform Processor Based on the SAW Chirp Transform Algorithm," in 1978 Ultrasonics Symposium Proceedings (IEEE, New York, 1978), pp. 533-537.
18. R. W. Ralston et al., "A New Signal-Processing Device, the Integrating Correlator," in 1977 Ultrasonics Symposium Proceedings (IEEE, New York, 1977), pp. 623-628, DDC AD-A057512.
19. J. H. Cafarella, "Acoustoelectric Signal-Processing Devices with Charge Storage," in 1978 Ultrasonics Symposium Proceedings (IEEE, New York, 1978), pp. 767-774.

UNCLASSIFIED

SECURITY CLASSIFICATION OF THIS PAGE (When Data Entered)

19 REPORT DOCUMENTATION PAGE		READ INSTRUCTIONS BEFORE COMPLETING FORM
1. REPORT NUMBER (18) ESD-TR-79-8	2. GOVT ACCESSION NO.	3. RECIPIENT'S CATALOG NUMBER
4. TITLE (and Subtitle) (6) Solid State Research, 1979:1. A068563	5. TYPE OF REPORT & PERIOD COVERED (9) Quarterly Technical Summary 1 November 1978 - 31 January 1979	
7. AUTHOR(s) (10) Alan L. McWhorter	6. PERFORMING ORG. REPORT NUMBER 1979:1	
9. PERFORMING ORGANIZATION NAME AND ADDRESS Lincoln Laboratory, M.I.T. P.O. Box 73 Lexington, MA 02173 (12) 82 P.	8. CONTRACT OR GRANT NUMBER(s) (15) F19628-78-C-0002	
11. CONTROLLING OFFICE NAME AND ADDRESS Air Force Systems Command, USAF Andrews AFB Washington, DC 20331	10. PROGRAM ELEMENT, PROJECT, TASK AREA & WORK UNIT NUMBERS Program Element No. 65705F Project No. 649L	
14. MONITORING AGENCY NAME & ADDRESS (if different from Controlling Office) Electronic Systems Division Hanscom AFB Bedford, MA 01731	12. REPORT DATE (11) 15 February 1979	
	13. NUMBER OF PAGES 88	
	15. SECURITY CLASS. (of this report) Unclassified	
	15a. DECLASSIFICATION DOWNGRADING SCHEDULE	
13. DISTRIBUTION STATEMENT (of this Report) Approved for public release; distribution unlimited. (16) 649L		
17. DISTRIBUTION STATEMENT (of the abstract entered in Block 20, if different from Report)		
18. SUPPLEMENTARY NOTES None		
19. KEY WORDS (Continue on reverse side if necessary and identify by block number)		
solid state devices quantum electronics materials research microelectronics	surface-wave technology photodiode devices lasers laser spectroscopy	imaging arrays infrared imaging surface-wave transducers
20. ABSTRACT (Continue on reverse side if necessary and identify by block number)		
<p>This report covers in detail the solid state research work of the Solid State Division at Lincoln Laboratory for the period 1 November 1978 through 31 January 1979. The topics covered are Solid State Device Research, Quantum Electronics, Materials Research, Microelectronics, and Surface-Wave Technology. Funding is primarily provided by the Air Force, with additional support provided by the Army, ARPA, NSF, and DOE.</p>		

DD FORM 1 JAN 73 1473 EDITION OF 1 NOV 65 IS OBSOLETE

UNCLASSIFIED

SECURITY CLASSIFICATION OF THIS PAGE (When Data Entered)

207 650